ADVANCED THEORY AND SIMULATIONS
www.advtheorysimul.com

A Theoretical Framework for Ratiometric Single Ion Luminescent Thermometers—Thermodynamic and Kinetic Guidelines for Optimized Performance

Markus Suta and Andries Meijerink*

Luminescence (nano)thermometry is an increasingly important field for remote temperature sensing with high spatial resolution. Most typically, ratiometric sensing of the luminescence emission intensities of two thermally coupled emissive states based on a Boltzmann equilibrium is used to detect the local temperature. Dependent on the temperature range and preferred spectral window, various choices for potential candidates appear possible. Despite extensive experimental research in the field, a universal theory covering the basics of luminescence thermometry is virtually nonexistent. In this manuscript, a general theoretical framework of single ion luminescent thermometers is presented that offers simple, user-friendly guidelines for both the choice of an appropriate emitter and respective embedding host material for optimum temperature sensing. The results show that the optimum performance (thermal response and sensitivity) around T_0 is realized for an energy gap ΔE_{21} between thermally coupled levels between $2k_BT_0$ and $3.41k_BT_0$. Analysis of the temperature-dependent excited state kinetics shows that host lattices in which ΔE_{21} can be bridged by one or two phonons are preferred over hosts in which higher order phonon processes are required. Such a framework is relevant for both a fundamental understanding of luminescent thermometers but also the targeted design of novel and superior luminescent (nano)thermometers.

1. Introduction

Temperature is the most fundamental thermodynamic state variable and still the most frequently measured quantity in science.[1,2] The zeroth law of thermodynamics offers a very simple direct measurement prescription of temperature that relies on the thermal equilibrium between two systems that are in contact to each other and thus, will aspire to have the same temperature. The importance of temperature is also stressed by its role as the measure for one of the seven base units of the international system of units (SI = Système international), which has been recently redefined by the elevation of Boltzmann's constant, k_B, to a fixed exact natural constant.[3,4]

In most practical temperature measurements, the temperature is determined from an ideally precisely known relation to another physical quantity that is easily measurable. This concept allows a direct mapping to temperature after thorough calibration and is already well established. However, the conventionally known examples of thermal expansion of a liquid used in household thermometers or temperature dependence of resistance are spatially limited to only a few mm and thus require macroscopic contact interaction. Since the 1990s, various improvements have been presented that allowed to measure temperatures even at lower length scales. Many examples were gathered in the extensive reviews by Childs et al.[2] or Rai[5] and include detection of thermal expansion[6–8] or a local thermoelectric voltage in, e.g., scanning thermal microscopes.[9–13] Similarly well governing overviews on the appropriate usage of noncontact pyrometry using black-body radiation as the governing temperature calibration law were published by Khan et al.[14,15] This has been complemented by a recently presented concept on precision measurements of thermal emission even from opaque objects.[16] A short review on the history of the development of phosphor thermometry was published by Allison.[17]

Since the beginning of the twenty-first century, a revived interest in optical thermometry can be noted.[5,18–23] Especially the interest in luminescence thermometry has rapidly grown due to the demand for remote temperature sensing with high precision.[24–37] Moreover, its noninvasive nature and the high temporal and spatial resolution below 10 µm make it suited for many locally focused applications otherwise difficult to achieve.[38,39] A variety of emitters has proven to be useful for optical thermometry. A particularly impressive and advanced proof of concept in this sense was illustrated for single NV^- defects in

Dr. M. Suta, Prof. A. Meijerink
Condensed Matter and Interfaces
Debye Institute for Nanomaterials Science
Department of Chemistry, Utrecht University
Princetonplein 1, Utrecht 3584 CC, The Netherlands
E-mail: m.suta@uu.nl

The ORCID identification number(s) for the author(s) of this article can be found under https://doi.org/10.1002/adts.202000176

DOI: 10.1002/adts.202000176

nanodiamonds. The zero-field splitting of the triplet ground state of these defects shows a very strong temperature dependence with reported absolute temperature accuracies below 10 mK in the vicinity of room temperature and high spatial resolution (<100 nm).[40–46] A simple way of probing this zero-field splitting is, e.g., detection of the decrease in the red fluorescence intensity of the NV^- centers upon sweeping with microwave radiation.

Another important class of potential luminescent thermometers includes quantum dots (QDs). Their emission intensity in the visible or near infrared range is very sensitive in a very narrow temperature regime (10 °C–60 °C).[47–49] Their long emission wavelengths (red/near infrared regime) make them particularly suited for bioimaging[36,50–58] and resulted in the usage of bright Ag_2S QDs for that purpose,[59–61] which could be recently upgraded to very bright "superdots" by protection with a photochemically induced AgCl shell.[62] In line with QDs, semiconducting bulk halides also entered the stage as sensitive luminescence lifetime thermometers in the range between 0 °C and 100 °C based on their self-trapped exciton luminescence.[63] Finally, other currently attractive and sensitive (especially lifetime-based) thermometers employ the luminescent $3d^3$ ions Cr^{3+} [64–70] or Mn^{4+}[71–76] in symmetric fluorides or oxides and are based on a $^2E \rightarrow {}^4T_2$ (in cubically symmetric crystal fields) thermally induced nonradiative crossover at higher temperatures that lead to a strong decrease of the ^2E-related luminescence decay time.[77] The usage of thermal coupling between states of simultaneously present transition metal ions with different oxidation states has also been presented by Marciniak et al.[78,79] Recently, also the unusual ion Mn^{5+} has attracted attention for that purpose.[80]

Optical (nano)thermometry has shown high potential in the experimental elucidation of several thermodynamic phenomena at the nanoscale and its superiority over, e.g., thermographic methods, which can only measure surface temperatures. Demonstrative examples include the experimental measurement of the Brownian velocity of nanocrystals in suspensions,[81] the in vivo detection of the brain[55] or intracellular[28,82] temperature, direct measurements of (transient) heat transfer properties of a lipid bilayer,[83] temperature monitoring of liquid or gas flows[23,84] or also detection of local temperature increases on catalysts[85,86] due to exothermic reactions. In all cases, luminescence thermometry particularly captivates by the simplicity of the respective experimental setup consisting of a laser source, the luminescent nanocrystals in contact with the medium to be characterized and a fast processing detection system.

Among the various possibilities of temperature detection by means of luminescence, the by far most widely employed type is based on the detection of a luminescence intensity ratio (LIR) between two emission lines or bands.[19,26,27] The acquisition of a ratio allows for more accurate and precise temperature measurements since the LIR as a relative quantity is not readily affected by variations in absolute luminescence intensities.[35] If the two probed emission bands stem from thermally coupled excited states within a single ion, the LIR should classically follow a Boltzmann distribution at elevated temperatures due to the fact that the luminescence intensity is proportional to the population in the excited state.[19]

Lanthanides have proven to be particularly well suited for ratiometric luminescence thermometry due to their high number of closely lying emissive energy states stemming from the $4f^n$ configuration that allow for luminescence detection from the ultraviolet (UV) over the visible to near infrared (NIR) range.[31,35,37,87–91] The shielded nature of the 4f orbitals and the resulting $4f^n \rightarrow 4f^n$-based narrow emission peaks at well-defined wavelengths allow to accurately measure LIRs without substantial spectral overlap.[87–91] If doped into thermally stable inorganic nano- or microcrystalline hosts, lanthanides thus found many promising applications such as Pr^{3+},[19,92–95] Nd^{3+} (often sensitized with Yb^{3+})[33,96–121] or Tm^{3+}[122–124] in the field of room temperature sensing and thermal bioimaging. Er^{3+} and Yb^{3+} is the traditional lanthanide couple for upconversion-based in vivo imaging,[125–133] or in situ temperature monitoring of catalytic reactions or flow reactions in microfluidic devices.[85,86,134–138] Recently reported creative alternatives of the use of this upconversion couple were vacuum sensing[139] or photothermal conversion.[140] Finally, Sm^{3+},[141,142] Eu^{3+},[135,143–146] Dy^{3+}[147–153] or Ho^{3+}[154–157] show potential for thermometry far above room temperature, as was also reviewed by Chambers and Clarke.[158]

In addition to LIR thermometry based on single ion emission spectra, another strongly developed field involves energy transfer thermometry. Especially Eu^{3+} and Tb^{3+} interacting with triplet states of organic antennas have become a de facto standard with high relative sensitivities at cryogenic temperatures.[159–166] More recent attempts reveal that lanthanides in mesoporous materials may be a promising addition to the field.[167–170] Usage of the lanthanides as luminescent ions even allows the combination of different functionalities such as luminescence thermometry and single-ion magnetism[171,172] or solid-state lighting.[173] Moreover, creative ways for novel alternative thermometry concepts using Boltzmann-based thermometry in the ground states have also been presented, which have the potential to strongly enhance relative sensitivities.[174–178] Also anomalous thermal quenching effects often found in nanocrystals was demonstrated to be a successful strategy to achieve high relative sensitivities.[118,179,180] For the sake of completion, it is also noteworthy that divalent lanthanides such as Sm^{2+},[181–183] Eu^{2+},[184] Tm^{2+}[185–188] and especially Yb^{2+}[189–192] show potential for luminescence thermometry, although their thermal behavior is often not governed by simple Boltzmann statistics anymore, but more complex temperature-dependent excited state dynamics involving a crossover to the $4f^{n-1}5d^1$ configuration.[193,194] Unlike the chemically more challenging examples of divalent lanthanides, Pr^{3+} has also recently been introduced as an alternative, more stable luminescent thermometer with the same underlying principle of a $4f^2$ –$4f^15d^1$ crossover (with eventual incorporation of thermal ionization into the conduction band).[195–197] The presented overview is still by no means complete and demonstrates the extremely rapid evolution of the research field.

Usage of the Boltzmann distribution for temperature calibration with a LIR is only valid if the thermal exchange rate between the two emissive states is much faster than any competing radiative or nonradiative depopulation rate. The case of a failure of Boltzmann equilibrium has been recently explicitly demonstrated for Eu^{3+},[198] but is also known to occur for, e.g., Dy^{3+}.[135] The validity and sensitivity of the Boltzmann distribution for thermometry is delicately dependent on the energy difference, ΔE_{21}, between the two emissive states with respect to the temperature range to be probed. While this fact is readily clear for the case that $\Delta E_{21} \gg k_B T$ based on an inefficient thermal population of the

higher excited state, the consequences of the opposite case $\Delta E_{21} \ll k_B T$ are not as intuitively evident. Given the large number of possible electronic $4f^n$ microstates of lanthanides, the flexibility in choice of a potential luminescent probe for luminescence thermometry appears unlimited if ΔE_{21} is in the order of several $k_B T$. Any inappropriate choice of a lanthanide ion for luminescence thermometry at a temperature of interest may in principle work, but at the cost of a low temperature sensitivity and thus, high temperature uncertainty. Critical reviews stressing the various experimental difficulties in achieving high precision and accuracy in luminescence thermometry have been recently published by the group of Jaque,[199,200] Dramićanin's book[201] and perspective[202] or by Bednarkiewicz et al.[203]

Despite the enormous amount of experimental data available in the literature of luminescence thermometry, a governing unifying theory that allows for a systematically driven search towards effective thermometers is still virtually non-existent. Only in the last few years, some progress towards this direction is recordable, which also resulted in the availability of applets and programs. Besides the overview works by Brites et al. stressing the theoretical gap in luminescence thermometry,[35,37] (lifetime) thermometry models on Mn^{4+} or Cr^{3+} [64,74,77] have already been developed. Moreover, Judd-Ofelt intensity calculations have resulted in the open-source Java applet *JOLIR* (Judd-Ofelt luminescence intensity ratio).[204] Another practical tool written in MATLAB is *TeSen*, which allows an automated analysis of the sensitivities and performance parameters of both Boltzmann-based and crossover-based thermometers after input of the measured temperature-dependent luminescence data.[205] Despite the development of those programs and applets, a generalized theoretical framework aiming at a basic understanding and simple guidelines on the choice of any combination of host and luminescent ion to address a temperature range of interest with optimized performance is still surprisingly lacking up to now.

The overall goal of this work is thus a theory-based derivation of clear and user-friendly quantitative guidelines for both the choice of the luminescent ion and the host material to achieve optimized performance of a respective ratiometric single ion luminescent thermometer. For that purpose, this work is divided into three main parts. The first part deals with the thermodynamic foundations of ratiometric luminescence thermometers that are based on the Boltzmann distribution as governing temperature calibration law. This part contains a derivation of optimized thermodynamic conditions for most responsive and sensitive temperature detection upon usage of two thermally coupled excited states. Guidelines for both the choice of an optimized energy difference and the most suitable phonon energy to bridge that gap are elucidated and allow for an optimized choice of a lanthanide ion-host compound couple with respect to the desirable temperature range to be detected. The second part deals with an account on the validity regime of a linearization of the Boltzmann distribution often applied in in vivo nanothermometry for the sake of simpler calibration. A careful error analysis and guidelines for its usage are presented therein. The third part accounts for the kinetics and the conditions for sustainment of the Boltzmann equilibrium over a wide temperature range. The impact of the radiative decay rates on the Boltzmann equilibrium will be quantitatively discussed in relation to nonradiative thermalization processes and it is demonstrated under which conditions

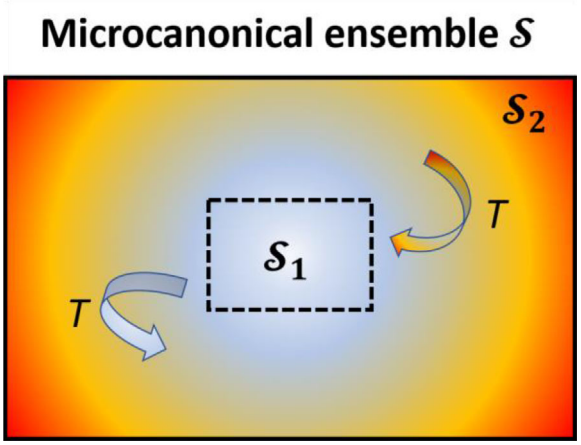

Figure 1. Schematic representation of the conditions for the derivation of the Boltzmann distribution from statistical physics. A large heat reservoir $\mathcal{S}_2$ is in thermal contact with a canonical ensemble $\mathcal{S}_1$ in order to exchange heat and reach thermal equilibrium. The whole system $\mathcal{S} = \mathcal{S}_1 + \mathcal{S}_2$ is microcanonical and considered closed from the environment. Note that the arrows are only supposed to indicate thermalization and do not illustrate the direction of the heat flow since the second law of thermodynamics only allows heat to flow from a hot to a cold object.

the additional pathway of radiative decay can lead to a failure of the Boltzmann-based luminescent thermometer at sufficiently low temperatures. A generalized excited state dynamics model for all temperatures will be derived that inherently contains the Boltzmann distribution and gives clear accounts for the rules to tune a luminescence thermometer toward Boltzmann behavior for widest temperature ranges possible. In conclusion, this manuscript provides a general theoretical framework for narrow-band emitting single ion luminescence thermometers with the aim to provide fundamental understanding and explicit user-friendly guidelines that allow for a more systematic approach toward an optimum luminescence thermometer for any temperature range instead of a common trial-and-error strategy.

2. Thermodynamic Perspective—Optimization of Thermometry with the Boltzmann Distribution

2.1. Derivation and Approximations of the Boltzmann Distribution in Statistical Physics

For the following sections and assessment of the assumptions for the validity of a Boltzmann distribution for thermometry, it is insightful to review its derivation from statistical physics and get an impression of the employed assumptions. For that purpose, consider a canonical ensemble $\mathcal{S}_1$ that is in thermal contact with a much larger heat reservoir $\mathcal{S}_2$, i.e., the ensembles are allowed to exchange thermal energy but no particles. The whole system $\mathcal{S} = \mathcal{S}_1 + \mathcal{S}_2$ is microcanonical and thus, thermally isolated from the environment (see **Figure 1**).

Moreover, it is assumed that $\mathcal{S}$ is a macroscopic system such that the thermodynamic limit is valid, and both the total particle number and volume may be safely regarded as constant. Finally, it is necessary to rely on the fundamental postulate of statistical physics stating that for a microcanonical ensemble in thermo-

dynamic equilibrium, each of its microstates in phase space is occupied with the same probability.

With all these preliminaries, we seek for the probability $p_m(T)$ at a given fixed temperature T that the canonical ensemble $\mathcal{S}_1$ is in an arbitrary g_m-fold degenerate microstate $|m\rangle$ in phase space with potential energy E_m.[206] E_m is presumed to be smaller than the total conserved energy E of the macroscopic ensemble $\mathcal{S}$. Out of the initially $\Omega(E)$ available microstates of $\mathcal{S}$, only $\Omega_2(E-E_r)$ are left since $\mathcal{S}_1$ in microstate $|m\rangle$ is part of $\mathcal{S}$. The desired probability p_m is then

$$p_m(T) = g_m \frac{\Omega_2(E-E_m)}{\Omega(E)} \tag{1}$$

Since $E_m \ll E$ and due to the fact that $\Omega(E)$ and $\Omega_2(E-E_m)$ are very large in the thermodynamic limit, it is reasonable to consider the logarithmic value $\ln \Omega_2(E-E_m)$ instead and expand it around the small E_m

$$\ln \Omega_2(E-E_m) = \ln \Omega_2(E) - \left.\frac{\partial \ln \Omega_2(E_2)}{\partial E_2}\right|_{E_2=E} E_m + \mathcal{O}\left(\frac{E_m^2}{E^2}\right) \tag{2}$$

where E_2 denotes the total potential energy of the residual system $\mathcal{S}_2$. The quadratic order term is clearly negligible as $E_m \ll E$. The logarithmic terms are reminiscent of Boltzmann's statistical definition of entropy, $S := k_B \ln \Omega$, and thence, the derivative term may be related to the macroscopic definition of temperature

$$\left(\frac{\partial S}{\partial E}\right)_N = \left(\frac{\partial \left(k_B \ln \Omega\right)}{\partial E}\right)_N = \frac{1}{T} \tag{3}$$

where the subscript N denotes constant particle number. Equation (3) may be easily derived from the first law of thermodynamics using the fact that the internal energy does not change at a given temperature T. In statistical physics and throughout this work, it will occasionally prove convenient to employ the more natural thermodynamic reciprocal temperature β,

$$\beta := \frac{1}{k_B T} \tag{4}$$

Usage of Equation (3) leads to

$$\ln \Omega_2(E-E_m) = \ln \Omega_2(E) - \frac{E_m}{k_B T} \tag{5}$$

Thus, Equation (1) evolves to the Boltzmann distribution function

$$p_m(T) = g_m \frac{\Omega_2(E)}{\Omega(E)} \exp\left(-\frac{E_m}{k_B T}\right) := \frac{g_m}{Z_c} \exp\left(-\frac{E_m}{k_B T}\right) \tag{6}$$

with Z_c as the canonical partition function,

$$Z_c = \sum_m g_m \exp\left(-\frac{E_m}{k_B T}\right) \tag{7}$$

ensuring that the probability is properly normalized to 1.

In the context of luminescence thermometry, the desirable model system of choice is a luminescent entity with two well isolated excited states that exchange heat with a macroscopic heat reservoir and among each other. In the context of the ensembles, the luminescent ions represent the canonical ensemble $\mathcal{S}_1$, while the nanocrystals containing the luminescent ions can be considered as the heat reservoir $\mathcal{S}_2$. Equation (6) is valid for the description of the thermal population statistics between the two excited states if the thermal exchange rate among the two excited states is high enough such that thermodynamic equilibrium is always sustained and all emissive ions can be considered as distinguishable and independent units. This readily implies that the radiative decay rates from the excited states have to be much lower than the respective nonradiative rates in order to govern a sufficiently quick thermal equilibration. It is also noteworthy that the assumptions for the validity of the Boltzmann equilibrium exclude energy transfer-based luminescent thermometers as they involve interacting ions. As long as it can be guaranteed that the nonradiative transitions are much faster than the energy transfer, an ensemble of several ions may also be considered as noninteracting.

Instead of the absolute thermal probabilities of finding the luminescent ion in the excited state $|1\rangle$ or $|2\rangle$, respectively, it is mostly of more practical interest to regard their relative population. Suppose the states have the degeneracies g_1 and g_2, respectively. For the effective predictions shown later within this work, it will prove useful to normalize the populations to their degeneracies. These populations will be labeled with primes throughout this work. Thus, the population ratio of the two states at a given temperature is easily obtained from Equation (6),

$$\frac{N_2'}{N_1'} = \frac{N_2/g_2}{N_1/g_1} = \frac{p_2(T)/g_2}{p_1(T)/g_1} = \exp\left(-\frac{E_2-E_1}{k_B T}\right) = \exp\left(-\frac{\Delta E_{21}}{k_B T}\right) \tag{8}$$

The relative net change in population at a temperature T is assessed by

$$\frac{N_1/g_1 - N_2/g_2}{N_1/g_1 + N_2/g_2} = \frac{\Delta N'}{N'_{tot}} = \tanh\left(\frac{\Delta E_{21}}{2k_B T}\right) \tag{9}$$

defined such that it only takes values between 0 and 1. It is close to 100% at very low temperatures since state $|2\rangle$ is empty then. At very high temperatures compared to the energy gap, the relative change is close to 0 since states $|1\rangle$ and $|2\rangle$ reach thermodynamic equilibrium and the populations are equal in that case.

2.2. Foundations of Single Ion Luminescence Thermometry

2.2.1. Proper Definition of the Measure of luminescence Intensity for Thermometry

For practical luminescence thermometry, it is relevant to consider all necessary conditions on the experimental setup and the approximations that need to be fulfilled. In a typical luminescence thermometry experiment, only low excitation powers are

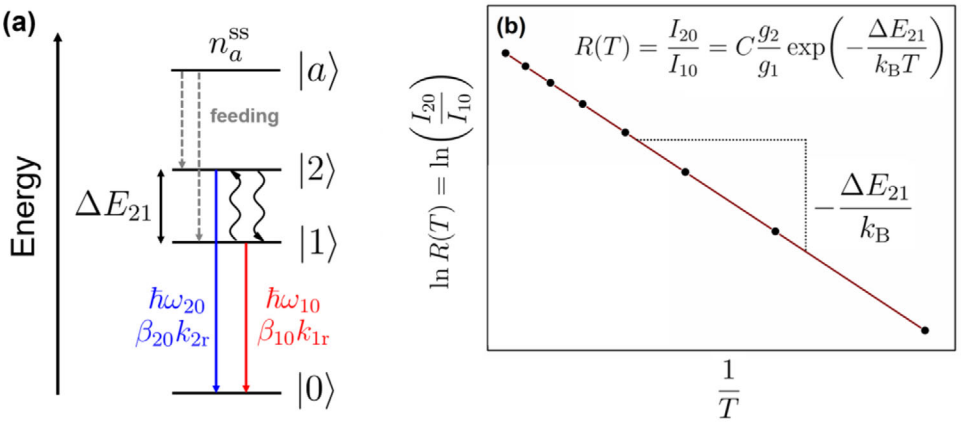

Figure 2. a) Simplified energy level diagram for the performance of a single ion luminescent thermometer. A higher lying auxiliary level $|a\rangle$ is excited by an external light source to sustain a steady state population density n_a^{ss} in that level. The thermally coupled levels $|1\rangle$ and $|2\rangle$ are nonradiatively fed by $|a\rangle$ (dashed arrows). Straight arrows indicate radiative transitions, curly arrows nonradiative transitions. b) A plot of the logarithmic LIR from the two thermally coupled levels versus reciprocal temperature affords a straight line with slope $-\Delta E_{21}/k_B$ and intercept of $\ln C + \ln(g_2/g_1)$ in case of a Boltzmann equilibrium.

employed such that no population inversion of the ground state is induced. Thus, only spontaneous emission significantly contributes to luminescence and only that limit is relevant for conventional luminescence thermometry. Next, suppose that there is a homogeneous doping fraction of x luminescent ions to be excited. A macroscopic volume V of a doped material is considered to be composed out of s unit cells with volume V_{uc} each. Each unit cell contains Z effective formula units of the composition of the material with ν cations supposed to be substituted (e.g., $\nu = 2$ in a composition A_2L_3 with A being the cations). Then, the average number of ions found in the volume is $sZ\nu x$. It is desirable that the ions are in close contact with the heat reservoir in order to avoid heat loss and temperature mismatch between the real temperature of the object and the actually measured temperature by means of luminescence thermometry. Thus, the lateral distance between ion and heat source is supposed to be negligibly small compared to the system dimensions. The external excitation source emits light of a given photon energy $\hbar\omega_{0a}$, which reaches the thermometric material with an incident irradiance I_0 (in W m^{-2}). As long as the irradiated surface area of the luminescent thermometers (e.g., nanocrystals or microcrystals) is much lower than the incident beam area, it is an excellent approximation to neglect light loss due to, e.g., scattering within or reflection from the medium until the photons reach the ions of interest, i.e., $I(\boldsymbol{r}_{ions}) \approx I_0$ with $\boldsymbol{r}_{ions}$ as the position of the ions. This approximation is practically always met as typically only micro- or nanocrystalline luminescent thermometers are employed.

Now suppose that the ions are excited from a ground level $|0\rangle$ into an auxiliary level $|a\rangle$ with absorption cross section σ_a. Moreover, it is assumed that the auxiliary level decays with an effective rate K both radiatively to any ground level(s) and non-radiatively to the thermally coupled excited levels $|1\rangle$ and $|2\rangle$ of interest (see **Figure 2**a).[19] The steady-state population of ions in the excited level $|a\rangle$ then reads (see Supporting Information for a detailed derivation)

$$N_a^{ss} = \frac{sZ\nu x\sigma_a I_0}{K\hbar\omega_{0a}} = \frac{VZ\nu x}{V_{uc}}\frac{\sigma_a I_0}{K\hbar\omega_{0a}} = V\cdot\frac{\rho N_A \nu x}{M}\frac{\sigma_a I_0}{K\hbar\omega_{0a}} \tag{10}$$

where ρ is the mass density of the material, N_A is Avogadro's constant and M is the molar mass. In practice, it is common to consider the population density $n_a^{ss} = N_a^{ss}/V$ instead. The steady-state population densities n_1 and n_2 of the thus indirectly fed levels $|1\rangle$ and $|2\rangle$, respectively, are both directly proportional to the population density n_a^{ss} (see Supporting Information). Moreover, it is important to realize that any thermometric experiment has to be conducted by this indirect feeding via a higher energetic auxiliary level $|a\rangle$ since direct excitation into one of the thermally addressed levels will drive the two excited levels out of thermodynamic equilibrium by means of the direct feeding by the constant external excitation.[19] For the sake of completeness, it should be mentioned that a thermometry experiment can also be performed with a pulsed excitation source if the integration time of spectral acquisition is higher than the pulse period $T' = 1/f$ with f as pulse frequency (see Supporting Information for more details), which is practically the case.

Now suppose that the levels $|1\rangle$ and $|2\rangle$ have total radiative decay rates k_{2r} and k_{1r}, respectively. The radiative emission rate to a selected ground level $|j\rangle$ is governed by the Einstein coefficient for spontaneous emission, A_{ij}, and a branching ratio β_{ij} ($i = \{1, 2\}$),

$$A_{ij} = \beta_{ij} k_{ir} \tag{11}$$

In the case of only one distinct ground level, it is $\beta_{ij} = 1$. The radiant power P_{ir} (in W) emitted by any of the two excited levels $|i\rangle$, $i = \{1, 2\}$ in the radiative transition $|i\rangle \rightarrow |j\rangle$ is then given by

$$P_{ir,0} = N_i A_{ij}\hbar\omega_{ij} \tag{12}$$

with $\hbar\omega_{ij}$ as the average emitted photon energy. This radiant power is isotropically emitted from the luminescent thermometers. At the distant light detector, only a portion of the totally radiated power is actually detected (due to the attenuation, quadratic with distance). In a ratiometric approach, however, this attenuation does not affect the indirect measurement of temperature

since both sample and detector are fixed, which makes calibration much simpler.

Conventional photon-counting detectors in luminescence spectrometers such as photomultiplier tubes (PMTs) do not measure incident radiant powers, but actually do single photon counting. Thus, it is necessary to relate the corresponding physical quantities to the radiated power according to Equation (12). One of the most immediately measured quantities in modern spectrometers is the incident spectral photon flux per unit wavelength, $\mathrm{d}\phi/\mathrm{d}\lambda$ (in photons s^{-1} nm^{-1}). The photon flux ϕ (in photons s^{-1}) is the incident number of photons impinging on a cross section of the detection unit per unit time. It is connected to the incident radiant power at the detection unit, P_{det}, as follows[18]

$$\phi_{21} = \frac{P_{\mathrm{det}}}{\hbar\omega_{21}} = \int_{E_1}^{E_2} \mathrm{d}E\, \frac{\mathrm{d}\phi}{\mathrm{d}E} = \int_{E_1}^{E_2} \mathrm{d}E\, \frac{\mathrm{d}\lambda}{\mathrm{d}E}\frac{\mathrm{d}\phi}{\mathrm{d}\lambda} = -\int_{\lambda_2}^{\lambda_1} \mathrm{d}\lambda\, \frac{\mathrm{d}\phi}{\mathrm{d}\lambda} \quad (13)$$

where $E_1 = hc/\lambda_1$ and $E_2 = hc/\lambda_2$ are the integration boundaries of the spectrum in the energy scale. Note that the areas and thus, the photon flux remain unaffected by the change from energy to wavelength scales. Only the representation of the spectral photon flux per unit energy differs from that in a wavelength scale,

$$\frac{\mathrm{d}\phi}{\mathrm{d}E} = \left|\frac{\mathrm{d}\lambda}{\mathrm{d}E}\right| \frac{\mathrm{d}\phi}{\mathrm{d}\lambda} = \left|-\frac{\lambda^2}{hc}\right| \frac{\mathrm{d}\phi}{\mathrm{d}\lambda} = \frac{\lambda^2}{hc}\frac{\mathrm{d}\phi}{\mathrm{d}\lambda} \quad (14)$$

consistent with earlier reports.[37,207,208] The negative sign accounts for the reversed integration direction in wavelength scales (short/long wavelengths correspond to high/low energies) and ensures that the integral photon flux ϕ_{21} remains positive. It should be noted that the spectrum $\mathrm{d}\phi/\mathrm{d}\lambda$ should be always corrected for either constant background due to, e.g., dark current in the PMT or a sloping background due to blackbody radiation. Any background or incorrect background correction can severely falsify the physically interpretable spectral data.

Finally, both the photomultiplier tube and also the dispersion grating in a spectrometer lead to additional photon loss, which can be compiled in a wavelength-dependent efficiency factor $\eta(\lambda) < 1$. The actually measured average count rate $\mathcal{R}_{ij}$ of a spectral transition (in counts s^{-1}) is then

$$\mathcal{R}_{21} = \int_{\lambda_2}^{\lambda_1} \mathrm{d}\lambda\, \eta(\lambda)\frac{\mathrm{d}\phi(\lambda)}{\mathrm{d}\lambda} \propto \phi_{21} \quad (15)$$

with $\lambda_2 < \lambda_1$. From that quantity, the average number of counts $\langle\mathcal{N}\rangle_{ij}(\Delta t)$ characterizing the radiative transition results from the count rate dependent on the user-set integration time Δt in a spectrum as $\langle\mathcal{N}\rangle_{ij}(\Delta t) = \mathcal{R}_{ij}\Delta t$. With all those preliminaries of the detection process, it is possible to finally define the proper LIR, $R(T)$, from two thermally coupled emissive levels by directly relating it to the experimentally accessible luminescence spectrum[37,207,208]

$$R(T) = \frac{\langle\mathcal{N}\rangle_{20}}{\langle\mathcal{N}\rangle_{10}} = \frac{\mathcal{R}_{20}\Delta t_2}{\mathcal{R}_{10}\Delta t_1} = \frac{\int_{\lambda_{22}}^{\lambda_{21}} \mathrm{d}\lambda\, \eta(\lambda)\left(\frac{\mathrm{d}\phi(\lambda)}{\mathrm{d}\lambda}\Delta t_2\right)}{\int_{\lambda_{12}}^{\lambda_{11}} \mathrm{d}\lambda\, \eta(\lambda)\left(\frac{\mathrm{d}\phi(\lambda)}{\mathrm{d}\lambda}\Delta t_1\right)}$$

$$= \frac{A_{20}}{A_{10}}\frac{N_2}{N_1} = \frac{\beta_{20}k_{2\mathrm{r}}}{\beta_{10}k_{1\mathrm{r}}}\frac{g_2}{g_1}\exp\left(-\frac{\Delta E_{21}}{k_{\mathrm{B}}T}\right)$$

$$:= C\frac{g_2}{g_1}\exp\left(-\frac{\Delta E_{21}}{k_{\mathrm{B}}T}\right) \quad (16)$$

where Equations (8) and (11)–(15) have been used. It is noteworthy that the pre-factor C only contains the emission branching ratios β_{i0} and the radiative decay rates $k_{i\mathrm{r}}$ ($i = \{1, 2\}$), which are easily accessible by independent steady-state and time-resolved luminescence experiments and allow an independent verification of the physical reliability of the fitting parameters in a Boltzmann fit of the temperature-dependent LIR data. More importantly, C is not dependent on the emission energies $\hbar\omega_{i0}$ in the case of single photon counting detection, in contrast to the conventionally found definition in the literature of luminescence thermometry. That error mostly stems from an inaccurate definition of measured luminescence intensity, which is nowadays the photon counting rate (see Equation (15)) or the average number of counts dependent on the type of spectrometer. It should be noted that C is generally checked very rarely for its physical reliability. However, in many cases, the error in introduction of $\hbar\omega_{i0}$ was barely noticed because of the very close energy range of the two comparable radiative transitions (i.e., $\hbar\omega_{10} \approx \hbar\omega_{20}$), which gives a ratio close to 1.

The definition according to Equation (16) offers an additional advantage. As most emission bands are composed of different subtransitions or are vibronically broadened, it is only possible to define an average emission energy, $\langle\hbar\omega_{ij}\rangle$, that would have to be elucidated by appropriate integration of the emission spectrum. Thus, a comparison of the fitted value of C to the expected value according to Equation (16) would be accompanied by an additional error introduced by determination of an expectation value of the emission energy (due to a standard deviation dependent on the quality of the spectral data).

Equation (16) can be simplified for practice in the case of narrow-band emitters (with spectral widths $\Delta\lambda < 10$ nm) such as the trivalent lanthanides. If the two emission transitions are in a very similar wavelength range, the correction factor $\eta(\lambda)$ can be often disregarded since it will not differ much in such a narrow range and can be regarded as approximately wavelength-independent quantity. The inclusion of the factor λ^2 according to Equation (14) is necessary if the spectra are supposed to be represented on an energy scale but is not relevant for the overall area under the emission spectrum.[37]

The form of Equation (16) implies that the temperature dependence is only contained in the exponential Boltzmann factor, while C is typically considered as temperature independent. This is not fully correct. Two main mechanisms can give rise to an additional temperature dependence of C. One possibility arises from a general temperature dependence of the radiative decay rate by means of strong electron–phonon coupling. This situation is particularly important for any luminescent ion with thermally coupled d^n electronic levels such as Cr^{3+} [64–70,77] or Mn^{4+}.[71–76] In those cases, an increase in temperature can induce an intensity redistribution from the zero-phonon transition to the Stokes and anti-Stokes ranges (see Section 2.4 for more details). Consequently, this leads to increasing radiative transition rates at elevated temperatures, which can also affect C. It will be shown in the Supporting Information under which circumstances C can be yet considered temperature independent.

The other possibility is commonly encountered in trivalent lanthanides with shielded $4f^n$ spin-orbit levels. These levels split into different crystal field states in a crystalline host compound by means of the Stark effect. At sufficiently low temperatures, if $k_B T$ is around as large as the crystal field splitting ΔE_{CF} (in the order of 100 cm^{-1}) between the split states of a spin–orbit level, a reorganization of the population among the crystal field states has an effect on both the branching ratios and the radiative decay rates from the different crystal field states. Thus, C could in principle bear a temperature dependence for very low temperatures ($T < 150$ K) in the case of trivalent lanthanides. As will be shown in Sections 2.4 and 5.2, however, at those temperatures, Boltzmann equilibrium between spin–orbit levels is typically not sustained anymore. Only at sufficiently large temperatures, i.e., if $k_B T \gg \Delta E_{CF}$, the population among the various crystal field states is in thermodynamic equilibrium and the spin–orbit level may be considered as an effective, thermally averaged single level with an average radiative decay rate and branching ratio. In that case, it is a valid approximation to consider the prefactor C as a temperature-independent quantity. It is noteworthy that any nonnegligible temperature dependence of C can have an impact on the performance of a luminescent thermometer, as was also pointed out by Brites et al. in their extensive review.[37] In essentially all practically relevant cases, however, the temperature dependence of C is much weaker than that of the Boltzmann factor and can be neglected in the regarded temperature range. A finally important remark is the fact that the definition of the constant C based on Equation (16) only contains information about the radiative decay rates, while any effects on the absolute intensities of the two emission bands are actually encoded in the excited state populations N_j. However, C (and also Equation (16) in general) are not affected by neither thermal quenching nor thermal coupling to higher excited states, which only have an influence of the separate luminescence photon counts of the two emission bands of interest but not on the radiative rates or the thermodynamic equilibrium. Only if the thermal quenching rates dominate over the thermalization rates, Boltzmann equilibrium cannot be sustained at very high temperatures anymore.

2.2.2. Additional Remarks on Advisable Luminescence Intensities and Doping Concentrations

If an average photon number $\langle \mathcal{N} \rangle$ is detected within a pre-set integration time, the relative uncertainty is given from Poisson statistics by

$$\pm \frac{\sigma_{\mathcal{N}}}{\langle \mathcal{N} \rangle} = \pm \frac{1}{\sqrt{\langle \mathcal{N} \rangle}} \tag{17}$$

This is referred to as the shot noise limit. This detection principle makes it advisable to set photon counting rates as close to the detector saturation as possible to minimize propagated errors in temperature determinations due to variations in emitted average photon counting numbers (see Section 2.3.2 for more details). For example, a detected average photon number of $\langle \mathcal{N} \rangle = 10^6$ already reduces the number fluctuations to only ±0.1%. This can be either achieved by preset high count rates or, alternatively, long integration times.

On the other hand, the number of emitted photons from the states $|1\rangle$ and $|2\rangle$ is both proportional to the population N_a of the auxiliary feeding state $|a\rangle$, which in turn is proportional to the number of available emitting ions $sZvx$ (see Equation 10). For a sufficiently high constant doping concentration and under the assumption of homogeneous doping, one simple approach would be an increase of the lateral dimensions to increase the number of ions by increasing the number of unit cells s in the excited volume. However, for high spatial resolutions below 10 µm in the field of nanothermometry, smaller volumes are mandatory. In those cases, higher doping concentrations are necessary to still allow for appreciable absorption of the nanothermometers. Thus, the concentration x must be chosen from a careful trade-off between high absorption strength, yet unperturbed luminescence without undesired side effects such as mutual ion interaction or concentration quenching as is often found in practice. Alternatively, the quenching pathways need to be kinetically controlled to yet allow for effective Boltzmann thermometry. Another option is the usage of high-power density excitation, which explains the success of laser sources for luminescence nanothermometry. However, local heating effects will then have to be avoided as, e.g., by usage of pulsed excitation sources with sufficiently low power density per pulse.[209] The alternative approach to increase the incident irradiance I_0 (see Equation 10) for a higher excited state population N_a should be taken with caution since, dependent on the size of the decay rate K, saturation of the excited states $|a\rangle$ can occur, which leads to diminished absorption. In the case of the slowly decaying $4f^n$-related spin–orbit levels, too high incident irradiances may also provoke undesired upconversion processes that can affect the calibration procedure by interfering radiative transitions from higher excited states. Finally, obvious (but by no means trivial!) measures to improve the count rates without negative side effects are optimizing the photon collection efficiency and the luminescence quantum efficiency. Especially for luminescent nanocrystals quantum yields can be low because of surface-related quenching processes. Careful design and synthesis of core–shell nanostructures are thus crucial in optimizing the performance in nanothermometry.

2.3. Estimates of the Preconstant *C* by Judd-Ofelt Theory—Computational Aid for Luminescence Thermometry with Trivalent Lanthanides

For $4f^n$ levels of the trivalent lanthanides, the prefactor C can be also semiempirically calculated within the phenomenological Judd-Ofelt theory,[210,211] as already indicated before.[37,204] This framework allows an estimation of induced electric dipole and magnetic dipole radiative transition rates between two spin–orbit levels with quantum numbers J and J', respectively, which is denoted by the Einstein coefficients for spontaneous emission, $A_{JJ'}$,

$$A_{JJ'} = \frac{4\alpha\omega_{JJ'}^3}{3g_J c^2}\left[n|\chi(n)|^2 S_{ED} + n^3 S_{MD}\right] \tag{18}$$

with $\alpha = \frac{e^2}{4\pi\varepsilon_0 \hbar c} \approx \frac{1}{137}$ as the dimensionless electromagnetic fine structure constant, c as the vacuum light velocity, $g_J = 2J + 1$ as the degeneracy of the emitting spin–orbit level, n as the refractive

index of the medium and $|\chi(n)|^2$ as a local electric field correction factor to account for photonic differences between vacuum and the dielectric host medium that the lanthanide is embedded in refs. [212–215]. Dependent on the wavelengths of the emission transitions, the refractive index has to be estimated by, e.g., the Sellmeier equation if the refractive index at other wavelengths is already known. However, especially for emission transitions in the NIR range, it is often a valid approximation to neglect dispersion of the refractive index and regard it as constant as long as the host does not absorb in that region itself. S_{ED} and S_{MD} are the so-called line strengths (in cm^2) of the induced electric dipole and magnetic dipole transition, respectively. Upon normalization to e^2 (contained in the fine structure constant in Equation (18)), their definition in the framework of Judd-Ofelt theory is as follows

$$S_{ED} = \sum_{t=2,4,6} \Omega_t |\langle 4f^n[\gamma LS]J||U^{(t)}||4f^n[\gamma' L' S']J'\rangle|^2 \quad (19)$$

and

$$S_{MD} = \left(\frac{\mu_B}{ec}\right)^2 |\langle 4f^n[\gamma SL]J||\boldsymbol{L} + g_S \boldsymbol{S}||4f^{n'}[\gamma' S' L']J'\rangle|^2 \quad (20)$$

The three quantities Ω_t (t = 2, 4, 6) are the phenomenological Judd-Ofelt intensity parameters (typically in the order of 10^{-20} cm^2) that are dependent on the type and local symmetry at the Ln^{3+} site in the host material. They were tabulated for many hosts by Görller-Walrand and Binnemans.[216] $U^{(t)}$ represents the irreducible unit tensor forms that characterize the electric dipole transition moment. The $|4f^{n'}[\gamma SL]J\rangle$ mark the spin–orbit states of the lanthanides in the intermediate coupling scheme, as indicated by the squared brackets, while γ represents all additional necessary quantum numbers. $\boldsymbol{L} + g_S\boldsymbol{S}$ with g_S = 2.002... as the electron g_S factor are the contributions of orbital and spin angular momentum to the magnetic moment of a transition, quantized in units of Bohr's magneton, $\mu_B = \frac{e\hbar}{2m_e}$. The overall matrix elements in both Equations (19) and (20) are the so-called dimensionless reduced matrix elements evolving from the Wigner-Eckart theorem. The electric dipole matrix elements (Equation 19) are tabulated by, e.g., Carnall et al.,[217] while the magnetic dipole matrix elements (Equation 20) have been gathered by, e.g., Dodson and Zia.[218] Nowadays, both are easily accessible within the open-source software RELIC (Rare Earth State and Intensity Calculation).[219] The applet JOES (Judd-Ofelt analysis from Emission Spectra) provides an additional simple tool for the immediate analysis of emission spectra for the special case of Eu^{3+}.[220]

Once the ED and MD line strengths for the two radiative transitions $|2\rangle \rightarrow |0\rangle$ and $|1\rangle \rightarrow |0\rangle$ of interest are known, usage of Equations (11), (16), and (18) leads to a semi-empirical estimate for the exponential prefactor C,

$$C\frac{g_2}{g_1} = \left(\frac{\omega_{20}}{\omega_{10}}\right)^3 \frac{n(\omega_{20})\left|\chi\left(n(\omega_{20})\right)\right|^2 S_{ED,20} + n^3(\omega_{20}) S_{MD,20}}{n(\omega_{10})\left|\chi\left(n(\omega_{10})\right)\right|^2 S_{ED,10} + n^3(\omega_{10}) S_{MD,10}} \quad (21)$$

with the transition line strengths as defined in Equations (19) and (20). In many practical cases, Equation (21) is further simplified due to the validity of additional approximations such as a negligible electric or magnetic dipole character of at least one of the considered emission transitions or similar refractive indices at the energies $\hbar\omega_{10}$ and $\hbar\omega_{20}$. The recently developed applet JOLIR (Judd-Ofelt Luminescence Intensity Ratio) has its foundations in Equation (21) and provides an automated tool to predict this preconstant C by means of Judd-Ofelt theory.[204] Apart from these recent developments, usage of Judd-Ofelt theory to estimate the preconstant C was only occasionally reported.[221–223]

While Judd-Ofelt theory accounts for the electric dipole contributions to the intensities of $4f^n$–$4f^n$ transitions, there are also theoretical approaches to predict the general appearance of lanthanide-based luminescence spectra. Despite the strong experimental progress in luminescence thermometry, knowledge about the availability of those computational program packages can help make lanthanide-based thermometry independently theoretically accessible. Thus, we also draw the attention of the interested reader to some of the currently existent, mostly open-source packages. Besides the foundations laid by common advanced crystal field calculations (see, e.g., the works from Malta, Burdick, Reid, Duan and Tanner),[217,224–227] there are also advances to make calculations as independent from experiment as possible. Usage of wavefunction-based post-Hartree-Fock approaches resulted in LUMPAC (Luminescence Package)[228,229] that employs semiempirical wavefunction methods and incorporates *ORCA* as a graphical user interface.[230,231] Recently, also ab initio multiconfigurational embedded cluster methods with a high level account of relativistic effects have been reported for Eu^{3+} and Tb^{3+} in cubic symmetries by Joos et al.[232,233] Finally, the different approach by the angular overlap framework of ligand field theory[234–236] led to the development of the currently optimized program package BonnMag,[237–241] which allows for simultaneous ligand field and intensity calculations of lanthanide-based spectra even at lower symmetries than cubic ones. All those packages have the potential to perform computational studies on novel thermometers and give predictive tools at hand to facilitate experimental trial-and-error attempts and support the development of next-generation luminescence thermometers based on lanthanide dopants.

2.4. Optimum Conditions for the Performance of Single Ion Two-State Luminescent Thermometers

2.4.1. Quantitative Guidelines for the Choice of an Optimized Boltzmann Thermometer

After having reviewed the foundations of the Boltzmann distribution for thermometry, we will now derive the conditions for an optimally sensing thermometer in a desired temperature range. A reasonable measure for the absolute sensitivity $S_a(T)$ of a luminescent thermometer is the thermal response of the LIR, $dR(T)$ (see Equation 16), to an infinitesimally small change of temperature dT,

$$S_a(T) \equiv \frac{dR}{dT} = \frac{\Delta E_{21}}{k_B T^2} \cdot C\frac{g_2}{g_1} \exp\left(-\frac{\Delta E_{21}}{k_B T}\right) \equiv S_r(T) \cdot R(T) \quad (22)$$

where $S_r(T)$ is commonly referred to as relative sensitivity (usually given in % K^{-1}) of the luminescent thermometer. For a Boltzmann-based thermometer (and only that!), the relative sensitivity can be explicitly given as

$$S_r(T) = \frac{\Delta E_{21}}{k_B T^2} \tag{23}$$

and is used as a figure of merit to allow comparisons between different thermometers irrespective of their operational principle. Equations (22) and (23) are, strictly regarded, only correct if the temperature dependence of the pre-factor C can be neglected (see also Section 2.2.1). Otherwise, an additional term of $\frac{d\ln C}{dT}$ would have to be included for the relative sensitivity in both Equations (22) and (23). The temperature variation of $\ln C$ is, however, even weaker than that of C itself, which makes its neglection clearly plausible.

It is the purpose of this section to derive simple guidelines for optimized thermal response and relative sensitivity of any single ion luminescent thermometer working with the principle of the Boltzmann distribution. A more profound derivation of those guidelines from the concepts of statistical physics and Bayesian estimation theory is given in the Supporting Information and puts the following simple approach on a fundamental ground. Within this work, we will focus on the main results. In practice, most commonly the temperature range to be measured is predefined from an applicational perspective, while the energy gap between the two thermally coupled levels should be chosen such that it maximizes the response of the luminescent thermometer. From Equation (22), it can then be easily concluded that for a given energy gap, the most responsively detected temperature is

$$T_{opt} = \frac{1}{2}\frac{\Delta E_{21}}{k_B} \tag{24}$$

in agreement with reported earlier findings.[112,204,242]

So far, Equation (24) is still very specific for a certain choice of a luminescent ion, because it depends on the ion-related energy gap ΔE_{21}. In order to become independent from any specific luminescent system and allow for general predictive guidelines, both the thermal response $S_a(T)$ and the relative sensitivity $S_r(T)$ can be normalized with respect to their values at T_{opt}. This allows for the definition of energy independent response and sensitivity functions that are universally applicable to any single ion luminescent thermometer based on the Boltzmann distribution and allow general conclusions. For that purpose, it will prove useful to introduce the generalized variable r

$$r = \beta \Delta E_{21} = \frac{\Delta E_{21}}{k_B T} \tag{25}$$

that accounts for a simultaneous discussion on variations of the energy gap ΔE_{21} and the temperature T. It is noteworthy a similar reparametrization (although not the same) was applied in the classic paper by Collins et *al.* in order to compare different luminescence-based thermometry techniques.[17] Given that definition, the response function $\rho(r)$ normalized to its optimum $r_{opt} = 2$ is defined as

$$\rho(r) := \frac{S_a\left(T = \frac{1}{r}\frac{\Delta E_{21}}{k_B}\right)}{S_a\left(T = T_{opt} = \frac{1}{2}\frac{\Delta E_{21}}{k_B}\right)} = \frac{1}{4} r^2 \exp(2 - r) \tag{26}$$

while the respective normalized sensitivity function is given by

$$\sigma(r) := \frac{S_r\left(T = \frac{1}{r}\frac{\Delta E_{21}}{k_B}\right)}{S_r\left(T = T_{opt} = \frac{1}{2}\frac{\Delta E_{21}}{k_B}\right)} = \frac{1}{4} r^2 \tag{27}$$

The graphs of both functions are plotted in **Figure 3**a. While $\rho(r)$ goes through a global maximum at $r_{opt} = 2$ (cf. Equation (24)), $\sigma(r)$ monotonically increases for any $r > 0$. The evolution of the graphs of both the generalized response function $\rho(r)$ and the sensitivity function $\sigma(r)$ can be related to physical properties of the Boltzmann distribution. Thus, their meaning is more fundamental than simply being figures of merit for a luminescent thermometer. For low energy gaps and high temperatures ($r < 2$), the probability for excitation of state $|2\rangle$ becomes high according to Equation (6) (see also Figure 3b). Correspondingly, a high intensity of the emission from state $|2\rangle$ should be expected. Nonetheless, the response $\rho(r)$ is low in that regime because of the concomitantly decreasing remaining population in state $|1\rangle$ necessary to feed state $|2\rangle$. In that regard, the Boltzmann thermometer becomes thermodynamically saturated and the two states evolve towards equal thermal population. The sensitivity $\sigma(r)$ in turn is low because the relative net change in population tends to zero (see red curve in Figure 3b) in that regime, which corresponds to the thermodynamic equilibrium.

For $r > 2$, the energy gap is high and the temperature is low. Expectedly, the probability for a successful thermal excitation event from state $|1\rangle$ to $|2\rangle$ is rather low (see blue curve in Figure 3b). Consequently, the thermal response $\rho(r)$ also decreases for high r. In contrast, the relative sensitivity of a thermometer is very high in that regime since any successful excitation event will result in a large relative net change of the population distribution (see red graph in Figure 3b). It is evident that the energy gap of any practically useful luminescent thermometer should obey the condition $r \geq 2$ since otherwise both thermal response and relative sensitivity are low. That means that the two excited states should not be used at high temperatures for temperature sensing since then their effective populations N_1' and N_2' become equal (see Figure 3b). This reflects the generally reported problem that relative sensitivities are very low at high temperatures (as also suggested by Equation 22). According to Equation (27), this limitation at high temperatures can be overcome by choosing a larger energy gap ΔE_{21} to increase the value of r.

The upper analysis indicates an additional problem. Both $\rho(r)$ and $\sigma(r)$ increase with r simultaneously up to the optimum $r_{opt} = 2$. If a desired relative sensitivity S_{r0} is preset by the user, this implies that any Boltzmann-based luminescent thermometer can only perform at optimum conditions for temperatures up to

$$T_0 \leq \frac{2}{S_{r0}} \tag{28}$$

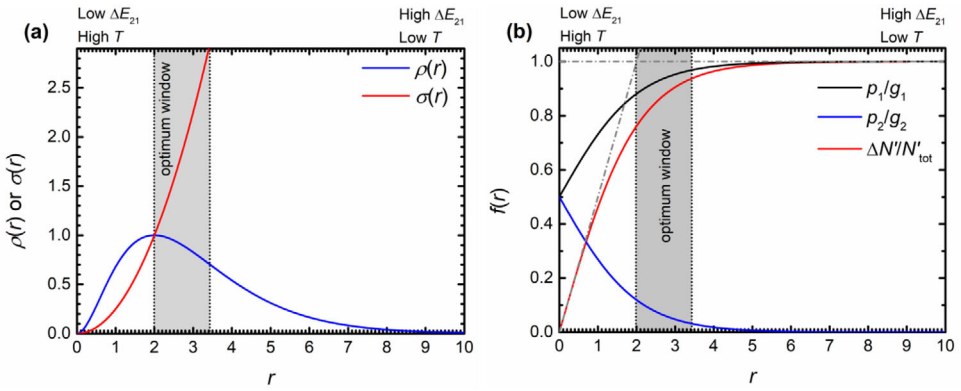

Figure 3. a) Graphs of the universally applicable normalized thermal response $\rho(r)$ (blue) and thermal sensitivity $\sigma(r)$ (red), as given by Equations (26) and (27). r represents the ratio between energy gap ΔE_{21} and thermal energies $k_B T$. The statistically advisable operation window for optimized performance of a Boltzmann-based single ion luminescence thermometer is also depicted. b) Evolution of the relative population $p_1(r)/g_1$ and $p_2(r)/g_2$ of states $|1\rangle$ (black) and $|2\rangle$ (blue) according to Equation (6), respectively. The relative change in population (red) with r according to Equation (9) is also depicted. The high temperature (low energy gap) and low temperature (high energy gap) asymptotes (dashed dotted lines) for the relative population change exactly cross in the optimum $r_{opt} = 2$.

Equation (28) immediately points at a fundamental limitation of Boltzmann-based thermometers, which will be highlighted in more detail below. If temperatures are supposed to be measured with at least $S_{r0} = 1\%\ K^{-1}$ relative sensitivity, the maximum temperature at which this is still feasible is 200 K. Higher desirable relative sensitivities ($S_{r0} > 1\%\ K^{-1}$) will lower the maximum measurable temperature even more, in agreement with this condition. Thus, if higher temperatures than given by Equation (28) are aimed to be measured with a luminescent thermometer, the user will have to sacrifice either thermal response for the sake of higher relative sensitivity or vice versa. In the following, we will give a simple justification which strategy is more advantageous. Again, the statistically profound derivation of this decision is illustrated in the Supporting Information for the interested reader.

A simple decision criterion is the comparison of the changes of $\rho(r)$ and $\sigma(r)$ with r in the range $r > 2$. While the gain in relative sensitivity is $\frac{d\sigma}{dr} \geq 1$ for $r \geq 2$, the maximum loss, $-\frac{d\rho}{dr}$, of $\rho(r)$ is found at the deflection position $r = 2 + \sqrt{2} \approx 3.41$ ($-\frac{d\rho}{dr}|_{r=2+\sqrt{2}} \approx 0.294$). Clearly, that value is still smaller than $\frac{d\sigma}{dr}$ in that range. Consequently, it is advisable to yet increase the energy gap ΔE_{21} and move to higher r with the sacrifice for a slight loss in thermal response $\rho(r)$ (and thus, thermally excited intensity I_{20} of state $|2\rangle$) to realize a higher gain in relative sensitivity. In numbers, the thermal response at $r = 2 + \sqrt{2}$ has only dropped to $\rho(2 + \sqrt{2}) \approx 0.71$ of the globally maximum value, while the relative sensitivity increases by a factor of $\sigma(2 + \sqrt{2}) \approx 2.91$. The deflection position $r = 2 + \sqrt{2}$ is also the statistically most advisable value for a maximum sacrifice in thermal response for the sake of higher relative sensitivity (see Supporting Information).

Any higher value for r still further increases the relative sensitivity, but the thermal probability for population of state $|2\rangle$ becomes already so low (see Figure 3b) that any corresponding thermally excited luminescence intensity I_{20} will be hardly detectable. This is practically undesirable as the shot noise will limit precise temperature measurements (see Equation 17).

The previous arguments can be translated to a simple decision flowchart that allows for an optimization of any single ion luminescent thermometer operating with the Boltzmann distribution. It is depicted in **Figure 4**. This flowchart provides the basis for the choice of an optimum luminescent ion for thermometry at any temperature range of interest. In practice, typically a desirable relative threshold sensitivity S_{r0} and the highest temperature T_0 to be measured are set. Then, the corresponding threshold value for r_0 is simply

$$r_0 = S_{r0} T_0 \tag{29}$$

If $r_0 < 2$ ($\Delta E_{21} < 2k_B T_0$), it may be easily increased to the optimum value of $r_{opt} = 2$ ($\Delta E_{21} = 2k_B T_0$), and both $S_r(T_0) > S_{r0}$ and $S_a(T_0)$ will be optimized, as both $\rho(r)$ and $\sigma(r)$ simultaneously strictly monotonically increase in that range.

If, however, $r_0 > 2$, it is statistically wise to increase r to $2 + \sqrt{2} \approx 3.414$ ($\Delta E_{21} = 3.414 k_B T_0$) since the gain in relative sensitivity supersedes the loss in thermal response. The flowchart in Figure 4 illustrates the optimization strategy for single ion luminescent thermometers schematically.

The described strategy also suggests that for any $r_0 > 2 + \sqrt{2}$, Boltzmann thermometry is not advisable with the predefined conditions anymore. This occurs either at too high temperatures ($T > T_0$) or too ambitiously predefined relative sensitivities S_{r0}. It is then required to release the desired conditions (e.g., by allowing a lower threshold relative sensitivity). Specifically, the analysis shows that each Boltzmann-based single-ion luminescent thermometer with a fixed energy gap of ΔE_{21} between the two thermally coupled states of interest is only suited for a limited temperature range such that $r \in [2, 2 + \sqrt{2}]$. Moreover, the previously presented simple guidelines restrict the number of apparently potential activators for luminescence thermometry already by fundamental properties derivable from the statistical nature of the Boltzmann distribution and allow a selection of the ion and the two excited states of interest in order to make the energy gap ΔE_{21} match the required temperatures to be measured. A way to overcome this limitation of two thermally coupled excited levels is the extension to more excited levels with successively larger energy gaps to the lowest excited emissive state, as has already been found experimentally earlier.[101,243,244] In that case, it

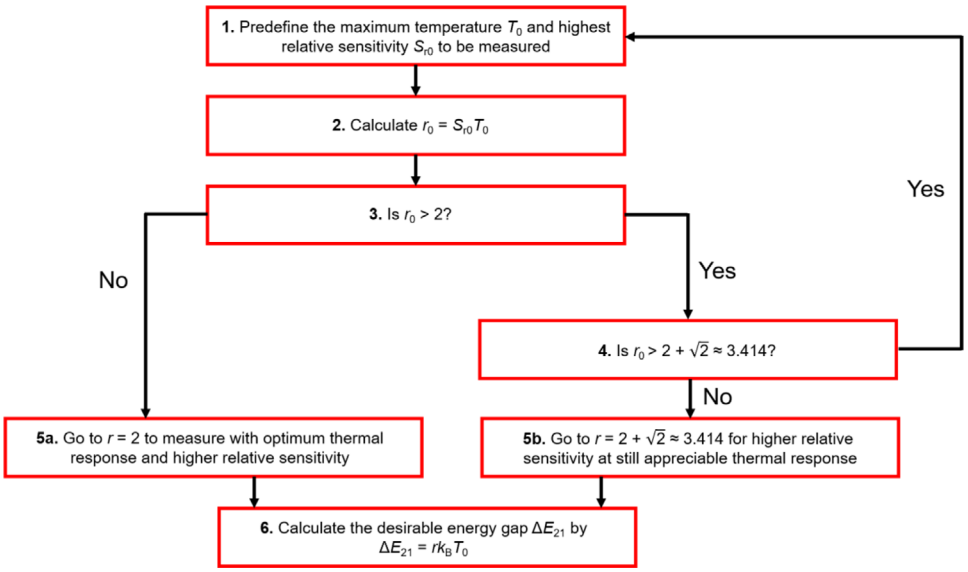

Figure 4. Decision flowchart for the choice of an optimized Boltzmann-based luminescence thermometer for a predefined desirable relative sensitivity S_{r0} and highest temperature T_0 to be measured. If r_0 exceeds the value $2 + \sqrt{2}$, the preset relative sensitivity S_{r0} or maximum temperature T_0 have to be reduced, respectively. For more explanations, see text.

is possible to retain optimum conditions at successively higher temperatures.

A numerical example illustrates the working principle of the developed flowchart. Suppose a user wants to measure temperatures close to $T_0 = 300$ K with a relative sensitivity of at least $S_{r0} \geq 1\%\ K^{-1}$. With these values, it follows $r_0 = 3.0$, which is larger than the optimum value at $r = 2$. Thus, the flowchart suggests choosing a luminescent ion with yet a larger energy gap ΔE_{21} such that $r = 2 + \sqrt{2}$. At $T_0 = 300$ K, this gives an energy gap of $\Delta E_{21} = 712\ cm^{-1}$. Although a bit of thermal response has been sacrificed, the relative sensitivity is slightly increased to $S_r = (2 + \sqrt{2})/T_0\ 100\% = 1.1\%\ K^{-1}$. Both the energy gap and the optimized relative sensitivity are typical values of the $^2H_{11/2}$–$^4S_{3/2}$ energy gap of Er^{3+}. Thus, the developed flowchart easily explains why Er^{3+} is still one of the most effective single ion luminescent Boltzmann thermometers for temperatures around room temperature. Another conclusion that can be made is, however, that above 342 K, it will not be possible to retain a relative sensitivity $S_{r0} \geq 1\%\ K^{-1}$ even with Er^{3+} under the suggested optimum conditions for good thermometry performance. The user will have to accept a lower relative sensitivity for still accurately detectable luminescence intensities from both excited levels. This example points at the previously mentioned fundamental limitation of Boltzmann thermometers.

Another well-known example is Nd^{3+}. Its excited $^4F_{3/2}$ spin–orbit level splits into two Kramers' doublet states R_1 and R_2 with an energy difference of around $\Delta E_{21} = 100\ cm^{-1}$, which are sufficiently well isolated from other disturbing energy levels.[99,104,114,117,120,245] Also, the two Kramers' doublets of the excited ^2E term of Cr^{3+} or Mn^{4+} in strong cubic crystal fields fall into this category (although with typically even lower energy gaps $< 100\ cm^{-1}$).[65–70] The flowchart can also be used to demonstrate for which temperature range a specific energy gap is most useful for. Suppose it is desirable to use it at the optimum, i.e., $r = 2$. For an energy gap of $100\ cm^{-1}$, the optimum temperature is then given by Equation (24), i.e., $T_{opt} \approx 72$ K, with a relative sensitivity of $S_r \approx 2.8\%\ K^{-1}$. Thus, the $R_1 - R_2$ gap of Nd^{3+} is most suited for measurements around liquid N_2 temperatures. It can be even used to measure lower temperatures thereby moving to $r = 2 + \sqrt{2}$. The minimum advisable temperature to use this energy gap for Boltzmann thermometry is thus $T \approx 42$ K, connected to an almost tripled relative sensitivity of around $S_r = 8.1\%\ K^{-1}$. For temperature above 72 K, however, the user successively shifts the thermal response and relative sensitivities to $r < 2$, clearly outside the optimum conditions of a Boltzmann thermometer. Therefore, room temperature sensing with the $R_1 - R_2$ gap already performs so close to the limit of equal excited state populations that a significant loss of relative sensitivity and thermal response are expected. At $T = 300$ K, it is $r = 0.48$ and the expected relative sensitivity of this energy gap is thus $S_r \approx 0.2\%\ K^{-1}$, exactly in the range of reported values.[99,105,114,117] The numerical examples give a clear impression how to optimize Boltzmann thermometers. Room temperature sensing using the Boltzmann distribution requires larger energy gaps, in the range of the spin–orbit splitting among $4f^n$ levels. Temperature sensing with the different crystal field states of a given spin-orbit level in lanthanides is meaningful for cryogenic temperatures only.

2.4.2. Guidelines for an Optimum Electronic Preconstant C

The previous thermodynamic guidelines for an optimized performance of a Boltzmann thermometer explicitly stated that it is advisable to use two excited states far from the limit of effectively equal excited state populations ($p_1/g_1 = p_2/g_2 = 0.5$ for $r \to 0$). An immediate consequence of an optimized performance, as also depicted in Figure 3b, is a sacrifice in population of the higher excited state $|2\rangle$. Despite higher relative sensitivity, this will lead to a lower emission intensity I_{20} and thereby increase the relative

uncertainty in the intensity measurement. The estimated temperature change dT connected to single-ion luminescence thermometry follows from Equation (22)

$$\mathrm{d}T = \pm\frac{1}{S_\mathrm{r}}\frac{\mathrm{d}R}{R} \tag{30}$$

One of the most commonly found arguments in the literature of luminescence thermometry is to tailor the relative sensitivity S_r to a very high value in order to keep the temperature uncertainty low. However, this argument only holds as long as the relative uncertainty in the LIR, σ_R/R, is also sufficiently low.[37,246] In that regard, the temperature uncertainty is also determined by the relative error in the measured separate photon counts $\langle\mathcal{N}\rangle_{10}(T)$ and $\langle\mathcal{N}\rangle_{20}(T)$. It is assumed that the measurement of the two luminescence intensities is uncorrelated, i.e., $\langle\mathcal{N}\rangle_{10}(T)$ and $\langle\mathcal{N}\rangle_{20}(T)$ can be measured independently from each other.

In a spectral acquisition, luminescence counts or count rates (see Equation (16)) are measured and connected to a relative uncertainty according to Poissonian statistics of photon detection (see Equation (17)). The actual relative uncertainty of the LIR, σ_R/R, is then given by

$$\frac{\sigma_R}{R} = \pm\sqrt{\left(\frac{\sigma_{\mathcal{N}_{10}}}{\langle\mathcal{N}\rangle_{10}}\right)^2 + \left(\frac{\sigma_{\mathcal{N}_{20}}}{\langle\mathcal{N}\rangle_{20}}\right)^2} = \pm\sqrt{\frac{1}{\langle\mathcal{N}\rangle_{10}} + \frac{1}{\langle\mathcal{N}\rangle_{20}}} \tag{31}$$

with $\langle\mathcal{N}\rangle_{10}$ and $\langle\mathcal{N}\rangle_{20}$ as the average count numbers of the radiative transitions $|1\rangle \rightarrow |0\rangle$ and $|2\rangle \rightarrow |0\rangle$. Consequently, the temperature uncertainty is

$$\sigma_T = \pm\frac{1}{S_\mathrm{r}}\sqrt{\frac{1}{\langle\mathcal{N}\rangle_{10}} + \frac{1}{\langle\mathcal{N}\rangle_{20}}} \tag{32}$$

which can be transformed to a relative uncertainty by Equations (23) and (25)

$$\frac{\sigma_T}{T} = \pm\frac{1}{r}\sqrt{\frac{1}{\langle\mathcal{N}\rangle_{10}} + \frac{1}{\langle\mathcal{N}\rangle_{20}}} \tag{33}$$

If the LIR obeys Boltzmann's law (16), it is

$$\frac{\sigma_T}{T} = \pm\frac{1}{r\sqrt{\langle\mathcal{N}\rangle_{10}}}\sqrt{1 + \frac{1}{C}\frac{g_1}{g_2}\exp(r)} \tag{34}$$

Besides the previously indicated condition for high average photon count numbers $\langle\mathcal{N}\rangle_{10}$ (also compare to the shot noise limit, Equation (17), Equation (34) also suggests that there is an advisable value for the pre-constant C. It is determined by the fact that both luminescence intensities are mutually as similar as possible resulting in a LIR of around 1 at a given temperature T_0 (a given r_0). However, the requirement for a LIR $\approx$ 1 appears incompatible to the statistical guidelines for fundamentally optimum performance of a Boltzmann-based luminescent thermometer (see Section 2.2). It turns out that the relative temperature uncertainty as given by Equation (34) can be minimized. The respective value r_min is given by the implicit equation (see Supporting Information for a more detailed discussion)

$$\frac{1}{2}\left(r_\mathrm{min} - 2\right)\exp\left(r_\mathrm{min}\right) = C\frac{g_2}{g_1} \tag{35}$$

and depends on the value of C.

The possibility to minimize the relative temperature uncertainty is understandable by the previously mentioned competition of high relative sensitivity at low temperatures T (high values of r) and appreciable thermal population of state $|2\rangle$ at high temperatures T (low values of r). With Equation (35) and knowledge on the optimum range of r, it is possible to derive an optimized pre-factor C for $r > 2$. At $r = r_\mathrm{min} = 2 + \sqrt{2}$, it follows from Equation (35) that the corresponding optimum value for C is given by $C\frac{g_2}{g_1} = \frac{\mathrm{e}^{2+\sqrt{2}}}{\sqrt{2}} \approx 21.5$. For higher values for C (see **Figure 5**a), the minimum expectedly shifts towards higher values of r (lower temperatures T) as C intrinsically increases the photon count number $\langle\mathcal{N}\rangle_{20}$. However, too high values for C are also not beneficial as then the relative sensitivity dominates the behavior of the relative temperature uncertainty (see increase of the blue curve in optimum window with decreasing r in Figure 5a) and $\langle\mathcal{N}\rangle_{10}$ also tends to decrease in turn.

Another interesting conclusion from Equation (35) is that the temperature uncertainty cannot be globally minimized at $r = r_\mathrm{opt} = 2$, as a corresponding value of $C = 0$ is physically not possible. This arises from the fact that every excited state has a non-zero decay rate by virtue of Heisenberg's uncertainty relation. The interpretation of this case is that at the optimum of $r = 2$, the change in thermal population from state $|1\rangle$ to $|2\rangle$ is maximum irrespective of the value of C. The relative temperature uncertainty can then only be additionally lowered by a respective increase in the photon count number $\langle\mathcal{N}\rangle_{10}$ (see Figure 5b). The photon count number $\langle\mathcal{N}\rangle_{20}$ will then be already sufficiently high due to thermal population from state $|1\rangle$. To overall comply with the previously derived optimum range for r and minimized temperature uncertainty, a value of $C\frac{g_2}{g_1}$ in the range of 20 is most reasonable as follows from Equation (35). Then, the LIR is also guaranteed to be close to 1, which appears meaningful for optimum thermometer performance.

Equation (35) provides additional design rules of the host material in the case of lanthanide ions based on the discussion in Section 2.3. The Judd-Ofelt intensity parameters are host- and symmetry-dependent and influence the values of the spontaneous decay rates A_{20} and A_{10}. By the same argument, the Judd-Ofelt parameters also affect the emission branching ratios. Overall, the upper optimum condition on C allows to at least partially design the host material towards desirable LIRs. In the optimum window this implies a higher radiative decay from the much less populated higher energy level. Enhancing the weaker emission intensity also reduces the uncertainty in the (lower) count rate which contributes more strongly to the temperature uncertainty.

An instructive example is again Er^{3+} with the two thermally coupled $^2H_{11/2}$ and $^4S_{3/2}$ spin-orbit levels. Both time-resolved luminescence studies and Judd-Ofelt calculations in, e.g., YVO_4[247] or β-$NaGdF_4$[248] revealed that the $^2H_{11/2}$ level has a five to tenfold

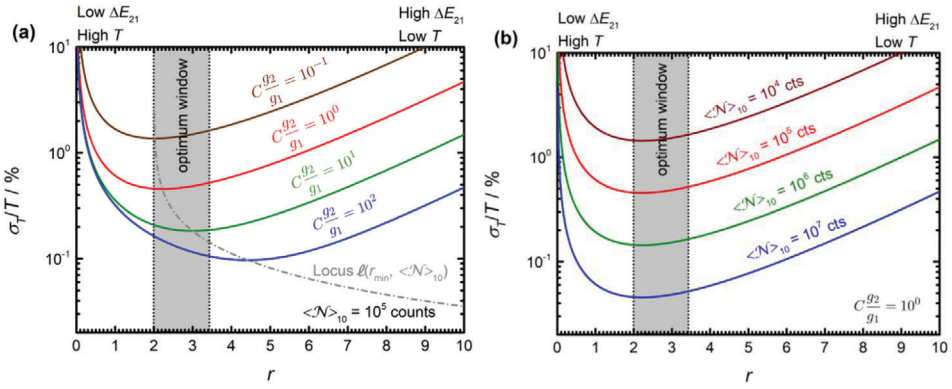

Figure 5. Evolution of the relative temperature uncertainty in relation to $r = \Delta E_{21}/k_B T$ with a) varying pre-factor C (at a given $\langle\mathcal{N}\rangle_{10}$) or b) count number of the lower energetic emission (at a given C). The locus depicted in a) is the connecting curve of all minimum points (see Supporting Information for more details).

higher radiative decay rate compared to the ground level than the $^4S_{3/2}$ level. Together with $g(^2H_{11/2}) = g_2 = 12$ and $g(^4S_{3/2}) = g_1 = 4$, this affords a value of $C\frac{g_2}{g_1}$ in the order of 15–30. Within the range, this value agrees with the recommendable optimum value $C\frac{g_2}{g_1} = 21.5$ at according to Equation (35). This again illustrates why Er^{3+} is a successfully applied Boltzmann-based luminescent thermometer for room temperature sensing.

It is insightful to compare the impact of an optimization of the preconstant C on the required emission photon count number $\langle\mathcal{N}\rangle_{10}$ from the lower energetic emission for a desired temperature uncertainty. Suppose that the desired relative temperature uncertainty is in the range of ±0.1%, i.e., the luminescent thermometer is expected to detect temperatures statistically reliably with an uncertainty of, e.g., less than ±0.3 K at 300 K. Moreover, the energy gap ΔE_{21} is assumed to match the optimum performance range, i.e., $r = 2$ to $2 + \sqrt{2}$. If $C = g_1/g_2$, Equation (34) implies that the minimum required photon count number of the emission from the lower lying state $|1\rangle$ has to be in the order of $\langle\mathcal{N}\rangle_{10} \approx 10^6$ counts (see Figure 5b). If, however, C is optimized and in the range of the desirable value of $C = 21.5\ g_1/g_2$ according to Equation (35), the necessary photon count number can be lowered by one order of magnitude, $\langle\mathcal{N}\rangle_{10} \approx 10^5$ counts to still obtain a relative temperature uncertainty of around 0.1%. This does not only offer the possibility to acquire luminescence spectra in shorter time, but also releases demands on, e.g., high doping concentrations (see Section 2.2.2) that could cause mutual ion interactions and thus disturb the performance of a Boltzmann thermometer. Moreover, an optimization of C by means of Judd-Ofelt theory for the lanthanides is worth considering in the field of nanothermometry, since attached surface ligands can lead to additional surface-related quenching of luminescence of dopants in nanocrystals. Low photon count rates are thus more common for nanocrystals.

2.5. Temperature Dependence of Radiative and Nonradiative Transition Rates

As already laid down in the derivation in Section 2.1, the validity of the Boltzmann distribution as the underlying model for luminescence thermometry critically depends on the fact that thermal equilibrium is sustained. This is the case if the nonradiative multiphonon transition rates between the coupled excited states are substantially higher than the radiative and other competitive relaxation rates. For trivalent lanthanides, the radiative decay rates k_r are typically in the order of 10^2–10^4 s^{-1} and temperature-independent for most host materials (see also below). Moreover, they are experimentally accessible by luminescence decay measurements at cryogenic temperatures ($T \leq 10$ K) if the absolute quantum yield of a corresponding emissive transition is close to unity at these temperatures (see Section 4.1 for more details). Radiative decay rates can be basically calculated from time-dependent perturbation theory or, in the case of trivalent lanthanides, within the framework of the phenomenological Judd-Ofelt theory (see Section 2.2). The previously mentioned applets or program packages RELIC,[219] LUMPAC,[228] or, for the special case of Eu^{3+}, JOES[220] are useful for an automated determination of Judd-Ofelt parameters from experimental $4f^n \leftrightarrow 4f^n$ absorption and emission spectra. Equation (18) then allows to calculate the radiative rate from the spontaneous emission coefficients.

The nonradiative rate, k_{nr}, in turn, shows both a prominent temperature-dependence and is strongly determined by the ratio between the energy difference ΔE_{21} and effective energy $\hbar\omega_{eff}$ of the optical phonons of an embedding host material. Thus, for a desirable kinetic control of Boltzmann equilibrium in a specific luminescent thermometer, it is mandatory to know the ratio between the radiative and nonradiative transition rates for a selected electronic transition at a given temperature. While Section 4 is fully devoted to the detailed kinetic analysis determining the performance of luminescent thermometers, this subsection will be focused on the temperature dependence of the non-radiative transition rates thus building the bridge between thermodynamics and kinetics. Moreover, here we will restrict ourselves on the sole case of multiphonon relaxation and neglect concentration-dependent effects such as energy transfer or cross relaxation, as they specifically depend on the considered ion couple and the respective excited states of interest.

From a theoretical point of view, nonradiative decay rates of lanthanide ions are quite often, if at all, only phenomenologically considered, which is related to difficulties in calculating this quantity accurately for $4f^n \leftrightarrow 4f^n$ transitions due to the

correspondingly low configurational coordinate offsets between the electronic states. Contrarily, for transitions with a corresponding offset, the Manneback recursion method by Fonger and Struck works very well.[249,250] This technique has been recently analyzed in detail for the temperature dependence of decay times of Mn^{4+} in inorganic hosts.[76] We will present an alternative, intuitive access to intrinsic nonradiative transition rates by means of an energy transfer interpretation in Section 2.5.

In contrast to the difficulties in prediction of the precise magnitude of the non-radiative rate $k_{nr}(0)$ itself (see Section 2.5 for that), all multi-phonon relaxation theories of intraconfigurational electronic states are consistent in their prediction of the temperature dependence of k_{nr}. For that, consider that the lanthanide ion is embedded in a crystalline host compound and coordinated by anionic or molecular ligands (this theory can, however, be also easily generalized to, e.g., single complexes). The thermal average occupation number of any phonon mode with quasi-momentum $\hbar\boldsymbol{k}$ in the host is given by the Planck formula,

$$\langle n_k \rangle = \left(\exp\left(\frac{\hbar\omega_k}{k_B T} \right) - 1 \right)^{-1} \tag{36}$$

If the offset between the representative harmonic potentials of the vibronic states $|1n\rangle = |1\rangle \otimes |n\rangle$ and $|2m\rangle = |2\rangle \otimes |m\rangle$ is close to zero, which is represented by a small Huang-Rhys-Pekar factor $S < 0.5$,[251] the multiphonon emission rate is simply governed by[252–257]

$$k_{nr}^{em}(T) = g_1 k_{nr}(0) \prod_k \left(1 + \langle n_k \rangle\right) \tag{37}$$

where the additional term of 1 accounts for the spontaneous emission contribution of the effective vibrational modes and $k_{nr}(0)$ denotes the limiting spontaneous non-radiative rate at 0 K. The corresponding absorption rate reads[252–257]

$$k_{nr}^{abs}(T) = g_2 k_{nr}(0) \prod_k \langle n_k \rangle \tag{38}$$

Correspondingly, the nonradiative absorption rate is reduced by a factor

$$\frac{k_{nr}^{abs}(T)}{k_{nr}^{em}(T)} = \frac{g_2}{g_1} \prod_k \frac{\langle n_k \rangle}{\left(1 + \langle n_k \rangle\right)} = \frac{g_2}{g_1} \exp\left(-\frac{\sum_k \hbar\omega_k}{k_B T} \right) = \frac{g_2}{g_1} \exp\left(-\frac{\Delta E_{21}}{k_B T} \right) \tag{39}$$

compared to the emission rate, which is just the Boltzmann factor and the microscopic physical foundation for ratiometric luminescence thermometry. Alongside, Equation (39) demonstrates that Boltzmann-based thermometry is valid for the case of multiphonon emitters only.

The Born-Oppenheimer potentials in a solid do not strongly deviate from harmonic behavior. Thus, electron–phonon coupling is typically dominated by the interaction with one effective vibrational mode of energy $\hbar\omega_{eff}$ below the cutoff energy $\hbar\omega_{max}$ of the phonon density of states. The number p of necessary phonons to bridge the electronic energy gap ΔE_{21} is the next smallest integer, i.e.

$$p := \left\lfloor \frac{\Delta E_{21}}{\hbar\omega_{eff}} \geq \frac{\Delta E_{21}}{\hbar\omega_{max}} \right\rfloor \tag{40}$$

with $\lfloor x \rfloor$ as the Gaussian floor function ensuring that p is an integer. For a reasonable elucidation of guidelines for luminescence thermometry, it will be assumed that both considered electronic states $|1\rangle$ or $|2\rangle$ couple to the same effective mode. $k_{nr}^{em}(T)$ and $k_{nr}^{abs}(T)$ from Equation (37) and (38) can then be simplified to

$$k_{nr}^{em}(T) = g_1 k_{nr}(0)\left(1 + \langle n_{eff} \rangle\right)^p \tag{41}$$

and

$$k_{nr}^{abs}(T) = g_2 k_{nr}(0)\langle n_{eff} \rangle^p \tag{42}$$

respectively.

As already mentioned earlier, the radiative decay rate $k_r(T)$ can also have a weak temperature dependence. That is particularly prominent for electronic states with electric dipole-forbidden radiative transitions. If those states couple more strongly to local odd-parity vibrational modes or phonons, the transition can become vibronically allowed. A very prominent example for that is the excited ^2E state (in cubically symmetric fields) of the $3d^3$ configuration like in Mn^{4+} or Cr^{3+},[64–77] but also the lowest excited (dominantly) triplet states $^3T_{2u}$ and ^3E_u of the $4f^{13}5d^1$ configuration of Yb^{2+}.[189]

For $T > 0$, vibronic coupling leads to an increase in the intensity of the Stokes (phonon emission, contribution of $1 + \langle n_{eff} \rangle$) and anti-Stokes sidebands (phonon absorption, contribution of $\langle n_{eff} \rangle$). Thus, $k_r(T)$ can gain an additional temperature-dependent contribution that increases by a factor of $2\langle n_{eff} \rangle + 1$,

$$k_r(T) = k_r(0)\left[1 + \kappa\left(1 + 2\langle n_{eff} \rangle\right)\right] = k_r(0)\left[1 + \kappa \coth\left(\frac{\hbar\omega_{eff}}{2k_B T} \right)\right] \tag{43}$$

κ represents the relative strength between the zero-phonon and vibronic side transitions. A theoretically very profound account on κ was elaborated by Grinberg.[71,77] Given its definition, κ also scales with the electron-phonon coupling constant. For trivalent lanthanides, the value of κ is typically very small ($\kappa \approx 0.01$–0.05) due to the shielded nature of the $4f^n$ orbitals and is therefore negligible then.[258,259] The temperature dependence is the foundation of the lifetime-based thermometric performance of Mn^{4+}- or Cr^{3+}-activated phosphors at cryogenic temperatures due to the stronger electron-phonon coupling in d orbitals.[63,70,72–75] Since $\coth(x) \to 1$ for $x \gg 1$ ($\hbar\omega_{eff} \gg k_B T$), while $\coth(x) \gg 1$ for $x \ll 1$ ($\hbar\omega_{eff} \ll k_B T$), the radiative decay rate becomes faster at low temperatures already.

2.6. Nonradiative Transitions as Energy Transfer Rates to Vibrational (Over)Tones—Unification of Electric and Magnetic Dipole-Type Transitions

While the temperature-dependence of multiphonon transitions is well understood, the intrinsic nonradiative transition rate

$k_{nr}(0)$ is more difficult to estimate. A very intuitive approach to non-radiative transitions was originally proposed by Ermolaev and Sveshnikova.[260,261] They embedded nonradiative decay processes in the context of an energy transfer interaction between the dipole moment governing the nonradiative transition and a local vibrational fundamental mode or overtone in resonance to the energy gap ΔE_{21} bridged by the nonradiative transition. This interpretation of nonradiative transitions is particularly insightful since it does not only allow their description by the same theory as radiative rates, but also unifies electric and magnetic dipole-type transitions as will be shown below. This model resulted in both qualitatively and quantitatively correct predictions in coordination compounds[260,261] and lanthanide-doped nanocrystals dispersed in organic or aqueous solutions.[262,263]

The most common form of nonradiative transitions includes an energy transfer between the electric transition dipole moment of the electronic transition and the corresponding vibrational dipole moment in the sense of a Förster-type energy transfer. It is the purpose of this section to illustrate the advantage of this interpretation to unify the two main types of underlying electron–phonon coupling into the explanation and how to control the magnitude of non-radiative transition rates. The starting point is Fermi's Golden Rule

$$k_{nr}(0) = \frac{2\pi}{\hbar}\left|\langle \mathcal{H}_{int}\rangle\right|^2 \rho\left(E_f\right) \tag{44}$$

In there, $|\langle \mathcal{H}_{int}\rangle|^2$ is the squared modulus of the Hamiltonian interaction matrix element while $\rho(E_f)$ denotes the available density of final phonon energy states and ensures the resonance condition for the energy transfer. An alternative view on $\rho(E_f)$ known from physics is that it defines the available phase space for the energy transfer: The higher $\rho(E_f)$, the higher is the probability for a non-radiative transition. This explains why usually optical phonon modes of matching energy are coupled to. Their typically flat dispersion in reciprocal space leads to a high density of states.

The electronic transition between the two excited states separated by the energy gap ΔE_{21} gives rise to an electric or magnetic transition dipole moment. In turn, the local vibrations or optical phonons can be interpreted to induce electromagnetic fields due to the movement of the surrounding ligands. The corresponding electric and magnetic field components are then derived from the Liénard-Wiechert potentials known from electrodynamics.[264] Those potentials are typically familiar to a wider audience as the foundation for synchrotron radiation. It is noteworthy that the following mechanism does not apply to acoustic phonons since they cannot induce electromagnetic fields. The wavelength of the vibrations ($\approx 10^{-5}$ m) is much longer than the activator-ligand bond lengths (≈nm) and especially longer than the vibrational amplitudes. Thus, it is a very good approximation to consider the induced electromagnetic fields in the near-field limit, i.e., close to the luminescent center.

Let $k_{vib} = 2\pi/\lambda_{vib}$ be the vibrational wavevector and $R = |\boldsymbol{r} - \boldsymbol{r}_{vib}|$ the distance between the activator and vibrating entity. Since it is $k_{vib}R \approx 10^{-4} - 10^{-3} \ll 1$, the near-field limit is a very accurate approximation. For the simplest case of a single point charge oscillating along the activator-ligand bond, the induced electromagnetic field components explicitly read as follows,

$$\boldsymbol{E}_{ind}(\boldsymbol{r}, t) = \frac{1}{4\pi\epsilon_0\epsilon_r}\frac{3\hat{\boldsymbol{r}}\left(\hat{\boldsymbol{r}}\cdot\boldsymbol{\mu}_{vib}(t)\right) - \boldsymbol{\mu}_{vib}(t)}{R^3} \tag{45}$$

$$\boldsymbol{B}_{ind}(\boldsymbol{r}, t) = \frac{\mu_0\mu_r}{4\pi}\frac{\dot{\boldsymbol{\mu}}_{vib}(t)}{R^2} \times \hat{\boldsymbol{r}} \tag{46}$$

where ϵ_0 and ϵ_r are the dielectric constants in vacuum and the relative medium permittivity, respectively, while μ_0 and μ_r are the magnetic vacuum and medium permeability, respectively. $\hat{\boldsymbol{r}}$ is the unit position vector,

$$\hat{\boldsymbol{r}} = \frac{\boldsymbol{r} - \boldsymbol{r}_{vib}}{|\boldsymbol{r} - \boldsymbol{r}_{vib}|} = \frac{\boldsymbol{r} - \boldsymbol{r}_{vib}}{R} \tag{47}$$

and $\boldsymbol{\mu}_{vib}(t)$ and $\dot{\boldsymbol{\mu}}_{vib}(t)$ are the vibrational transition dipole moment and its time derivative, respectively. Formally, Equations (45) and (46) have to be summed over several coordination spheres in order to capture the total contribution to the electromagnetic field components in the near-field regime. In that limit, the induced electric field component dominates despite the stronger R^{-3} distance dependence (see also below). However, Equation (46) also states that the magnetic field component is expected to scale proportionally to the phonon frequency (by means of $\dot{\boldsymbol{\mu}}_{vib}(t)$ assuming a harmonically oscillating dipole moment). This can be envisioned as a realization of the Biot-Savart law since a vibrating activator-ligand bond formally induces a current that in turn leads to a perpendicular magnetic field.[264] The induced magnetic field should become stronger for strong activator-ligand bonds containing light ligands, which vibrate with higher frequency.

Equations (45) and (46) also indicate that coupling is only possible to longitudinally polarized optical phonons since the induced field components will vanish otherwise. Moreover, in agreement to expectation, the magnetic field component is perpendicular to the electric field component. Finally, both $\boldsymbol{E}_{ind}(\boldsymbol{r}, t)$ and $\boldsymbol{B}_{ind}(\boldsymbol{r}, t)$ decrease if vibrational overtones or multiple phonons are created. This stems from a corresponding decrease in amplitude of the vibrational dipole moment $\boldsymbol{\mu}_{vib}(t)$. It is a consequence of the real anharmonicity of the bonds.[265–271] The weakening of the amplitude of the vibrational dipole moment roughly scales exponentially with the number of required phonons p,[268–272]

$$\left|\boldsymbol{\mu}_{vib}(0)\right|^2 \propto \exp(-\gamma p) \tag{48}$$

with a host-dependent constant γ in the order of 1. Equation (48) is the well-known energy gap law predicting an exponential decrease in non-radiative multi-phonon relaxation rates with the number of phonons involved. Several more elaborate modifications from higher-order perturbation theory such as the approaches by van Dijk and Schuurmans,[273] Hagston and Lowther,[274] Pukhov and Sakun or others[275–279] exist that allow for better agreement with experimental results, but consistently predict the exponential scaling according to Equation (48). In a solid, however, the rigidity of the crystal structure does not allow as anharmonic bonds as in a free molecule, which means that the

energy gap law (48) will only be valid for rather low phonon numbers ($p \leq 4$). For higher phonon numbers, the nonradiative transition rate between two levels is expected to be negligibly small in a solid. This is consistent with the experimentally established fact that radiative decay is usually expected from energy levels separated by a gap of 5 or more phonons from the next lower level.

With those preliminaries, the energy transfer interpretation of non-radiative rates between two electronic states can be simply understood as a coupling between transition dipole moment and vibrationally induced electromagnetic field. Let $\mathcal{F}$ represent any of the electromagnetic field components, $\mathcal{F} = \{\boldsymbol{E}(\boldsymbol{r}, t); \boldsymbol{B}(\boldsymbol{r}, t)\}$. The interaction matrix element then reads

$$\left|\langle \mathcal{H}_{\text{int}} \rangle\right|^2 = \left|\langle \boldsymbol{\mu}_{\mathcal{F}} \cdot \mathcal{F} \rangle\right|^2 \tag{49}$$

with $\boldsymbol{\mu}_{\mathcal{F}}$ as the electric or magnetic transition dipole moment at the luminescent center that couples to the corresponding field component $\mathcal{F}$, respectively. Equations (45)–(49) imply that any magnetic dipole-type nonradiative transition leads to much lower nonradiative transition rates than any corresponding electric dipole-type transition. Their relative magnitude can be estimated by

$$\frac{k_{\text{nr}}^{\text{MD}}(0)}{k_{\text{nr}}^{\text{ED}}(0)} = \frac{\left|\langle \boldsymbol{\mu}_{\text{mag}} \cdot \boldsymbol{B}_{\text{ind}} \rangle\right|^2}{\left|\langle \boldsymbol{\mu}_{\text{el}} \cdot \boldsymbol{E}_{\text{ind}} \rangle\right|^2} \approx \frac{n^4}{16}\alpha^2 \left(k_{\text{vib}} R\right)^2 \sim 10^{-8} - 10^{-9} \tag{50}$$

with $n^2 = \sqrt{\varepsilon_{\text{r}} \mu_{\text{r}}}$ as the refractive index and α as the electromagnetic fine structure constant. The results from this interpretation of nonradiative transitions are in excellent agreement with the original estimates by Dexter on magnetic dipole-electric dipole-type energy transfer mechanisms.[280] The magnetic dipole-electric dipole-type energy transfer additionally underlies specific symmetry selection rules in order to occur at all and may be inhibited in cubic symmetries.[281] Moreover, this general derivation predicts a clear difference in the dependence on the activator-ligand dependence for electric-dipole type ($\approx R^{-6}$) and magnetic-dipole type ($\approx R^{-4}$) transitions. The estimate from Equation (50) easily explains that magnetic-dipole type nonradiative transitions can become as slow as the radiative decay of $4f^n$ levels even if a resonant phonon can bridge the energy gap between the two coupled excited levels. It should be noted, however, that in the case of the lanthanides, electric dipole-type transitions are not pure but actually of induced nature in the framework of Judd-Ofelt theory. Thus, they are connected to much lower oscillator strengths $f_{\text{ind ED}}$ than 1 (typically in the order of 10^{-6}) and consequently, the weakening of magnetic dipole-type transitions as given in Equation (50) in the case of the $J \rightarrow J'$ transitions between spin-orbit levels of the lanthanides is not as severe,

$$\frac{k_{\text{nr}}^{\text{MD}}(0)}{k_{\text{nr}}^{\text{ind ED}}(0)} = \frac{f_{\text{ED}}}{f_{\text{ind ED}}} \frac{\left|\langle \boldsymbol{\mu}_{\text{mag}} \cdot \boldsymbol{B}_{\text{ind}} \rangle\right|^2}{\left|\langle \boldsymbol{\mu}_{\text{el}} \cdot \boldsymbol{E}_{\text{ind}} \rangle\right|^2} \approx \frac{1}{10^{-6}} \cdot \frac{n^4}{16}\alpha^2 \left(k_{\text{vib}} R\right)^2 \approx 10^{-2} - 10^{-3} \tag{51}$$

This estimate demonstrates that magnetic dipole-type nonradiative transitions are, however, still inherently slow compared to any transitions with an electric dipole type character.

The biggest advantage of non-radiative transitions in the framework of coupling between a transition dipole and a vibrationally induced field component is the employment of the well-established compendium on selection rules of radiative transitions to easily identify a certain type of nonradiative transitions among two excited states. Thus, not only does this mechanism unify magnetic and electric dipole type nonradiative transitions being two consequences of the same coupling mechanism, but it also asserts a direct relation between non-radiative transition rates and radiative ones. At least in the context of electric dipole-type transitions, this is analogous to the established theories of, e.g., Pukhov et al.,[275,278] Strek[282] or van Dijk and Schuurmans,[273] which describe non-radiative transition rates for lanthanides in a similar framework to Judd-Ofelt-based radiative decay rates. Thus, simple inspection of the reduced matrix elements (see Equations (20) and (21)) in Carnall's tables[217] or with programs such as RELIC[219] do also allow to at least qualitatively judge whether an intrinsic nonradiative transition rate between two excited levels is expectedly of (induced) electric dipole or magnetic dipole nature.

2.7. Guidelines on Phonon Energies $\hbar\omega_{\text{eff}}$ for Optimum Thermometry Performance

So far, only the optimized range for feasible energy gaps ΔE_{21} was specified, which offers guidelines for the most suitable choice of a luminescent ion. It is also possible to establish a similar decision flowchart for the optimum effective host phonon energy to bridge an energy gap ΔE_{21}. This provides an additional guideline for a thermodynamically optimized choice of host besides the guideline on the preconstant C to match the other condition for optimized photon count rates (see Equation (35)). According to the previous section, nonradiative rates can be interpreted as to arise from an interaction between a transition dipole moment and vibrationally induced electromagnetic field. This interpretation is only possible for optical phonons. Since the density of phonon states is very high for optical phonons all over the first Brillouin zone (for acoustic phonons, that is only the case at the zone boundary), luminescence thermometry is dominated by coupling to longitudinal optical phonons. Thus, we will restrict ourselves to this case only and disregard coupling to acoustic phonons, which is more relevant for thermal coupling among crystal field states with very low energy gaps. Optical phonon energies of typical inorganic host compounds for dopants cover a range between around 150 cm^{-1} (heavy halides) to around 1300 cm^{-1} (borates). Both the number of phonons p and the phonon energy $\hbar\omega_{\text{eff}}$ enter the non-radiative transition rates $k_{\text{nr}}^{\text{em}}(T)$ and $k_{\text{nr}}^{\text{abs}}(T)$ due to the energy gap law (Equation (48) and the Planck factor (Equations 41 and 42). It is insightful to compare the one-phonon non-radiative transition rates, $k_{\text{nr}}^{\text{em}}(T, p = 1)$ or $k_{\text{nr}}^{\text{abs}}(T, p = 1)$, to the respective p-phonon transition rates, $k_{\text{nr}}^{\text{em}}(T, p > 1)$ or $k_{\text{nr}}^{\text{abs}}(T, p > 1)$.

With higher required phonon numbers p, the intrinsic nonradiative transition rate $k_{\text{nr}}(0)$ exponentially decreases according to Equation (48). The ratios can be defined with respect to the previously introduced variable $r = \Delta E_{21}/k_{\text{B}}T$,

$$\frac{k_{\text{nr}}^{\text{em}}(r, p = 1)}{k_{\text{nr}}^{\text{em}}(r, p > 1)} = \frac{k_{\text{nr}}^{\text{abs}}(r, p = 1)}{k_{\text{nr}}^{\text{abs}}(r, p > 1)} \propto \exp(p - 1) \frac{\left[\exp(r) - 1\right]}{\left[\exp(r/p) - 1\right]^p} \tag{52}$$

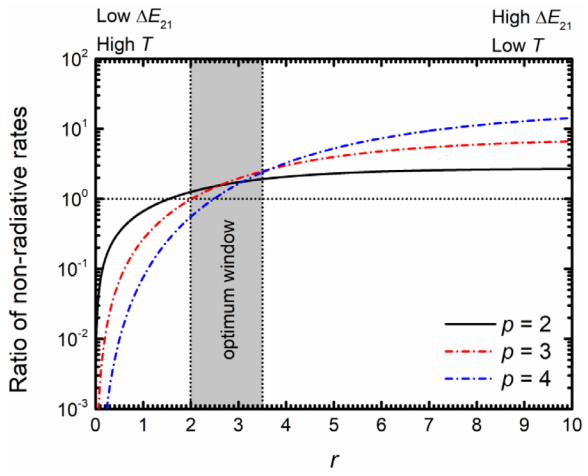

Figure 6. Ratios of the nonradiative transition rates involving one phonon to bridge an energy gap ΔE_{21} to the corresponding rate for a p-phonon transition (see Equation 52). The functions are parametrized in $r = \Delta E_{21}/k_B T$.

and are depicted in **Figure 6** for selected phonon numbers p. From the evolution of these ratios, the most advisable number of involved phonon modes to bridge the energy gap ΔE_{21} at a given temperature T can be deduced.

At the optimum $r = 2$, it is visible that a two-phonon nonradiative transition rate is almost as large as that for a one-phonon process. Those involving three and four phonons are even higher than the transition rate for a one-phonon process. This is understandable since $r = 2$ is already in a range of rather low energy gaps or elevated temperatures. In that regime, stimulated phonon absorption and emission can take place for sufficiently low phonon energies, which then accelerate nonradiative transitions between two electronic levels separated by the energy gap ΔE_{21}. Two shortcomings of the idealization of one effective mode become apparent here. At those high temperatures, also stimulated emission from lower energetic phonon modes will contribute, which still effectively increase the one-phonon nonradiative relaxation rate. This is not readily captured in a one-effective mode model. Moreover, it has been discussed in Section 2.3 that for practically desired relative sensitivities $S_{r0} > 1\%\ K^{-1}$, the optimum performance of a Boltzmann thermometer at $r = 2$ ($\Delta E_{21} = 2k_B T$) is only feasible at temperatures below 200 K or energy gaps below around 300 cm^{-1}. The required maximum optical phonon energies to allow three- or four-phonon processes are thus below 100 cm^{-1}, below the minimum cut-off optical phonon energies known for inorganic hosts. Overall, for $r = 2$, only one- or two-phonon processes are practically accessible with cut-off optical phonons. The non-radiative transition rates for the one- or two-phonon transitions are almost equal at $r = 2$ (see black curve in Figure 6). In Section 4.3, an additional kinetic argument for the restriction to maximum two phonons for Boltzmann thermometry will be given.

The choice of a host material that favors either a one- or two-phonon non-radiative transition rate is dependent on the practical conditions (see **Figure 7**a). The already low energy gap of maximum $\Delta E_{21} = 300\ cm^{-1}$ for optimum performance of the thermometer with sufficiently high relative sensitivity ($S_{r0} > 1\%$ K^{-1}) requires a host with an effective optical phonon mode at 150 cm^{-1}. This is typically encountered for heavy halides only, which are, however, difficult to chemically prepare completely anhydrous and nanocrystalline form. Thus, from a practical perspective, a one-phonon transition appears more compatible with the optimum conditions on a Boltzmann thermometer with high relative sensitivities. On the other hand, if the relative sensitivity is granted to be lower, both the eligible temperature and energy gaps are higher. For those cases, a two-phonon transition is a reasonable alternative to avoid non-radiative luminescence quenching to an energetically lower quenching state $|q\rangle$.

At $r = 2 + \sqrt{2} \approx 3.41$, the one-phonon nonradiative transition rate is dominant (see Figure 6). If compared to a two-phonon rate (see black curve in Figure 6), a one-phonon transition in that range of r is almost twice as fast, which clearly favors the choice of a host that allows for resonant one-phonon transitions to bridge the energy gap ΔE_{21}.

Especially if the nonradiative transition is magnetic dipole type, this can already be a crucial benefit. Thus, inherently slow magnetic dipole-type nonradiative transitions are not expected to perform well for Boltzmann thermometry at higher energy gaps or lower temperatures if more than one phonon is required to bridge ΔE_{21}. Electric dipole-type transitions are in turn expected to be more flexible towards a release of that restriction since they are inherently fast. This is particularly important if a lower energetic quenching state $|q\rangle$ is present. It is self-explanatory that for a reasonably performing luminescent thermometer $|q\rangle$ should be separated by a larger energy gap ΔE_{1q} from the emissive state $|1\rangle$ than the thermally addressed energy gap ΔE_{21}. The quenching rate exponentially decreases with the number of required phonons according to Equation (48). Thus, for a sufficiently high energy gap ΔE_{1q} (rule of thumb: $\geq 5\ \Delta E_{21}$), this precautionary choice of a host with lower phonon energy is not necessary and a host allowing for a one-phonon non-radiative transition can be chosen. If ΔE_{1q} is, however, only slightly larger than ΔE_{21}, it may be more reasonable to choose a host with lower maximum phonon energy and favor a two-phonon process. Although the corresponding nonradiative transition rates connecting states $|1\rangle$ and $|2\rangle$ for a two-phonon process are lowered by a factor of 2, the number of phonons consumed in the quenching process are also doubled, which reduces the quenching rate by a factor of $e^2 \approx 7.39$. Also these overall guidelines can be implemented in a similar decision flowchart (Figure 7b) towards an optimum effective phonon energy that allows for a specific choice of a suited host material for luminescence thermometry.

3. Assessment on the Linearization of the Boltzmann Distribution

Particularly in in vivo thermometry, only small temperature ranges are probed. In that special situation, the intensity ratio $R(T)$ may show an approximately linear correlation to the temperature, and would allow for an even simpler calibration of temperatures than with the Boltzmann distribution itself (see Equation 16).[36,55,123] However, dependent on the type of application, temperature precision is very important. Especially in those cases, it is mandatory to assess the errors introduced by such a simplification appropriately. Very often, a linearization of

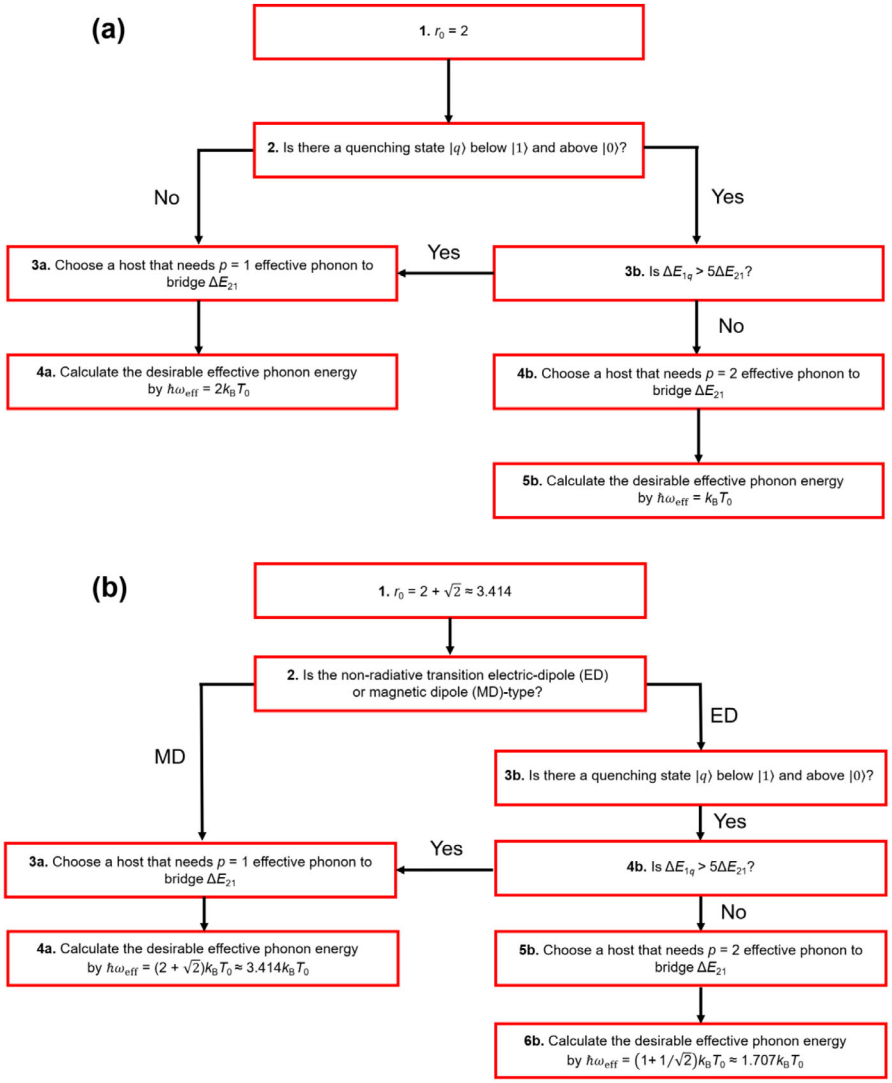

Figure 7. Decision flowcharts for the choice of the optimized effective phonon energy for a Boltzmann-based luminescence thermometer performing at a) $r_0 = \Delta E_{21}/k_BT = 2$ or b) $r_0 = \Delta E_{21}/k_BT = 2 + \sqrt{2}$. For further explanations on the flowcharts, see text.

the Boltzmann distribution and calibration with a linear least-squares fit is done without any justification. The purpose of this section is to provide the validity regime for such a linearization of Boltzmann's law. Moreover, it is also desirable to know which calibration method (linearized or Boltzmann-type plot) is more robust towards introduced systematic experimental errors such as those stemming from photon count fluctuations. Suppose a small temperature range ΔT around a desired central temperature $T_0 \gg \Delta T$ is measured. If $k_BT = k_B(T_0 \pm \Delta T) > \Delta E_{21}$, it is valid to expand the Boltzmann distribution (16) around T_0 and truncate the series after linear order,

$$R(T) = C\frac{g_2}{g_1}\exp\left(-\frac{\Delta E_{21}}{k_BT}\right) = C\frac{g_2}{g_1}\exp(-r_0)\left[(1-r_0)+r_0\frac{T}{T_0}\right] + \mathcal{O}\left(\left(\frac{\Delta T}{T_0}\right)^2\right) \quad (53)$$

with $r_0 = \Delta E_{21}/k_BT_0$. Both the Boltzmann distribution and the linear expansion are depicted in **Figure 8**a. In particular, Equation (53) predicts a positive slope for a plotting the intensity ratio directly versus temperature, in perfect agreement with reported findings in literature.[35,54,120]

The approximation of the Boltzmann distribution law by a linear expansion introduces an additional relative bias

$$\frac{\Delta(T)}{R(T)} = \left|1 - \left[(1-r_0)+r_0\frac{T}{T_0}\right]\exp\left[-r_0\left(1-\frac{T_0}{T}\right)\right]\right| \quad (54)$$

It is plotted for selected values of r_0 in terms of T/T_0 in Figure 8b. Two important aspects can be noted. First, the relative errors are generally smaller over a wider temperature range if $r_0 < 1$ or, alternatively, if $\Delta E_{21} < k_BT$ in perfect agreement with the stated precondition above. Second, the relative error becomes even minimized if $r_0 = 2$, which is a consequence of the thermal

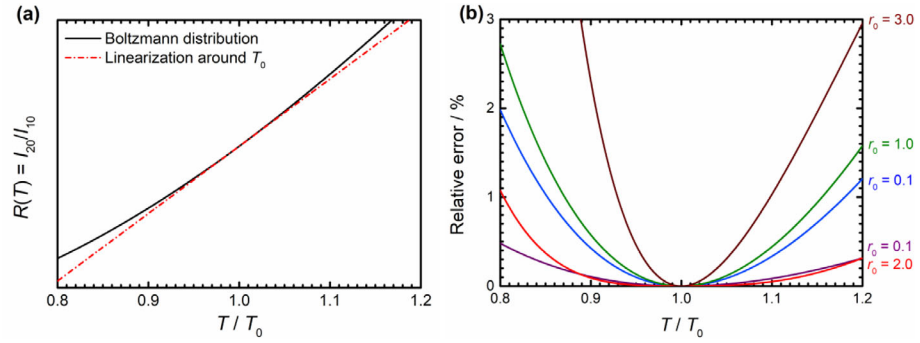

Figure 8. a) Illustration of the linearization (red, dashed-dotted) of a Boltzmann-type evolution (black, solid) of the LIR in a narrow temperature regime around central temperature T_0. b) Relative errors of the linear expansion of Boltzmann's law (see Equation 54) for different values of r_0 being an alternative representative of the energy gap ΔE_{21}.

response becoming maximized at that point (see Equation 24). For $r_0 > 2$, it quickly grows for small deviations from T_0. Thus, a strategy aiming at a minimum relative error for a linearization of the Boltzmann distribution would formally suggest to remain with the optimum condition (24). On the other hand, the validity of the expansion (53) is critically dependent on the magnitude of r_0 itself. An alternative, practically relevant condition on the decision for a linearization of the Boltzmann distribution is the robustness of the relative errors towards relative uncertainties of the measurable intensity ratio if a Boltzmann plot is employed for temperature calibration

$$\left|\frac{\mathrm{d}\ln R(T)}{\ln R(T)}\right| = \frac{1}{\left|\ln R(T)\right|}\left|\frac{\mathrm{d}R(T)}{R(T)}\right| \tag{55}$$

The relative error, $|\frac{\mathrm{d}R(T)}{R(T)}|$, in a linearized plot is only smaller than the relative error in a Boltzmann plot if $|\ln R(T)| < 1$. This is clearly the case for $\Delta E_{21} < k_B T_0$ or, alternatively, if $r_0 < 1$, as mentioned above. Thus, a linearization of the Boltzmann distribution is in fact even practically only justified for low energy gaps as given between, e.g., the crystal field states of $4f^n$ spin–orbit levels of trivalent lanthanide ions. Indeed, for Boltzmann thermometry relying on emission from the two crystal field components of the $^4F_{3/2}$ level of Nd^{3+} ($\Delta E_{21} \approx 100\ \mathrm{cm}^{-1}$), linearized calibration procedures have been successfully used around room temperature, consistent with the present findings.[105,114,120,245] However, linearization does not comply with the previously described optimization strategy toward an energy gap of at least $2k_B T$ for optimum performance and high relative sensitivities and is only of meaningful use for lower energy gaps and sufficiently narrow temperature ranges.

4. Kinetic Perspective—Control over Boltzmann's Law and Generalized Kinetics of Two Thermally Coupled Excited States

4.1. Analysis of the Excited State Dynamics—Experimental Determination of Radiative and Nonradiative Decay Rates of the Excited Two-State System

The validity of the Boltzmann distribution as the governing temperature calibration law for luminescence thermometry will critically depend on a balance between radiative decay and nonradiative transition rates. Only if nonradiative relaxation rates between thermally coupled levels are faster than radiative decay can Boltzmann equilibrium be kinetically realized. Besides advanced theoretical tools to predict those rates, still one of the simplest and most straightforward approaches to gain insight in the balance between radiative and nonradiative decay rates are luminescence decay experiments. For that purpose, it is insightful to consider the kinetics of an excited two-state system. It can be described by the following coupled system of rate equations,

$$\begin{pmatrix}\dot{N}_1(t,T)\\ \dot{N}_2(t,T)\end{pmatrix} = \begin{pmatrix}-\left(k_{1r}(T)+k_{nr}^{abs}(T)\right) & k_{nr}^{em}(T)\\ k_{nr}^{abs}(T) & -\left(k_{2r}(T)+k_{nr}^{em}(T)\right)\end{pmatrix}\begin{pmatrix}N_1(t,T)\\ N_2(t,T)\end{pmatrix} \tag{56}$$

where $N_j(t, T)$ denotes the time- and temperature-dependent population in the excited state $|j\rangle = \{|1\rangle, |2\rangle\}$. Equation (56) is valid under the assumption that the considered excited states are energetically sufficiently well separated from other excited states such that competing quenching or thermalization effects are negligible. Equation (56) can be in principle analytically solved for both $N_1(t, T)$ and $N_2(t, T)$ (see Supporting Information for the full solution and discussion of some limiting cases), which are both described by biexponential functions. The exact solutions are not very insightful for a detailed interpretation, however, since the resulting decay rates are complicated combinations of the rates in Equation (56).

The analysis is considerably simplified at sufficiently low temperatures (the lower boundary temperature will be given below) since it is then a valid approximation to set $k_{nr}^{abs}(T) \approx 0$ by Equation (42). All decay rates will then take their limiting values at $T \to 0$. Upon excitation into the lower excited state $|1\rangle$, the decay functions are given by (see **Figure 9**)

$$\begin{pmatrix}N_1(t,0)\\ N_2(t,0)\end{pmatrix} = N_1(0,0)\begin{pmatrix}\exp\left(-k_{1r}(0)t\right)\\ 0\end{pmatrix} \tag{57}$$

allowing a determination of $k_{1r}(0)$. As expected, the neglected nonradiative absorption rate leads to sole population of the lower excited state $|1\rangle$. Excitation into the higher excited state $|2\rangle$ is

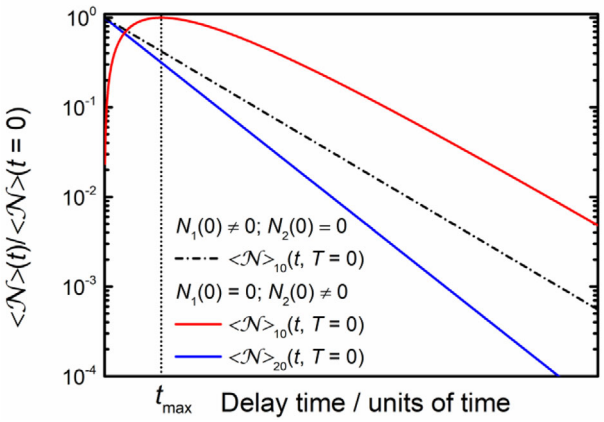

Figure 9. Theoretically expected luminescence decay curves (semilog scale) of an idealized excited two-state system at low doping concentrations and cryogenic temperatures. Dashed-dotted curves indicate excitation into state $|1\rangle$ while solid curves indicate excitation into state $|2\rangle$. t_{max} is also indicated. For further explanations, see text.

reflected in the initial condition $N_2(0,\ 0) \neq 0$ and gives (see Figure 9)

$$\begin{pmatrix} N_1(t,0) \\ N_2(t,0) \end{pmatrix} = N_2(0,0) \begin{pmatrix} \frac{k_{nr}^{em}(0)}{k_{2r}(0)+k_{nr}^{em}(0)-k_{1r}(0)} \left\{ \exp\left(-k_{1r}(0)t\right) - \exp\left[-\left(k_{2r}(0)+k_{nr}^{em}(0)\right)t\right] \right\} \\ \exp\left[-\left(k_{2r}(0)+k_{nr}^{em}(0)\right)t\right] \end{pmatrix} \tag{58}$$

It is typically $k_{1r} < k_{2r} + k_{nr}^{em}$, i.e., state $|2\rangle$ will decay faster than state $|1\rangle$, especially due to the additional nonradiative decay. The luminescence decay curve of state $|1\rangle$ shows an initial exponential rise based on the non-radiative feeding from state $|2\rangle$ and decays with a rate of $k_{1r}(T)$ at the longer delay time tail.

The time t_{max} at which the decay curve goes through a global maximum is dependent on the ratio between $k_{1r}(0)$ and $k_{2r}(0) + k_{nr}^{em}(0)$,

$$t_{max} = \frac{1}{k_{2r}(0)+k_{nr}^{em}(0)-k_{1r}(0)} \ln\left(\frac{k_{2r}(0)+k_{nr}^{em}(0)}{k_{1r}(0)}\right) \tag{59}$$

Since logarithmic growth is weaker than linear growth, t_{max} overall decreases with increasing $k_{nr}^{em}(0)$, which is also reasonable since feeding of state $|1\rangle$ proceeds faster then. Thus, t_{max} increases with decreasing phonon energy at low temperatures due to the energy gap law (48). Moreover, t_{max} converges to the maximum possible value of $k_{1r}^{-1}(0) = (k_{2r}(0) + k_{nr}^{em}(0))^{-1}$ in the limiting case of $k_{1r}(0) = k_{2r}(0) + k_{nr}^{em}(0)$. t_{max} is the time at which steady state conditions are present in the excited states despite pulsed excitation and the limit of equal rates ($k_{1r} = k_{2r} + k_{nr}^{em}$) corresponds to the extreme case of continuous steady state conditions. Section 5.2 will deal with the consequences of that extreme case for generalized ratiometric luminescence thermometry. Figure 9 illustrates the previously described appearance of the luminescence decay curves of both excited states at low temperatures, where $k_{nr}^{abs}(T) \approx 0$.

For accurate values of all decay rates, very low doping concentrations (≈ 0.01%–0.1%) are advisable in order to avoid side effects from energy transfer, cross relaxation or energy migration processes, which provide additional decay channels and severely complicate the analysis. Moreover, in time-resolved experiments, in which photons are detected by time-correlated single photon counting (TCSPC) techniques, the phosphor powder or colloidal solutions should be best diluted with non-absorbing powders or transparent dispersing solvents in the spectral range of interest, such as $BaSO_4$ or *n*-hexane.[263] This avoids reabsorption effects among luminescent centers in the same or different crystallites or nanoparticles, which would produce artificial lengthening effects on the measured radiative decay times. Also, saturation of the photon-counting detector should be avoided as that can also lead to artificial lengthening of measured decay times.

In order to extract the intrinsic nonradiative decay rate $k_{nr}(0)$ (see Equations (41) and (42) for the definition), it is necessary to acquire a separate photoluminescence spectrum upon selective excitation into state $|2\rangle$. Given that the emission intensities are measured in photon count numbers $\langle\mathcal{N}\rangle$, the relative quantum yields of the two states at sufficiently low temperatures can be assessed by the photon count numbers[189]

$$\begin{aligned} \phi_1(0) &= \frac{k_{nr}^{em}(0)}{k_{2r}(0)+k_{nr}^{em}(0)} = \frac{\beta_{20}\langle\mathcal{N}\rangle_{10}(0)}{\beta_{20}\langle\mathcal{N}\rangle_{10}(0)+\beta_{10}\langle\mathcal{N}\rangle_{20}(0)} \\ &= 1-\phi_2(0) \end{aligned} \tag{60}$$

with β_{10} and β_{20} as the respective emission branching ratios into the ground state $|0\rangle$. Thus,

$$k_{nr}(0) = \frac{\phi_1(0)}{g_1\tau_2(0)} = \frac{1}{g_1\tau_2(0)} \frac{\beta_{20}\langle\mathcal{N}\rangle_{10}(0)}{\beta_{20}\langle\mathcal{N}\rangle_{10}(0)+\beta_{10}\langle\mathcal{N}\rangle_{20}(0)} \tag{61}$$

and

$$\begin{aligned} k_{2r}(0) &= \frac{\phi_2(0)}{\tau_2(0)} = \frac{1}{\tau_2(0)} \frac{\beta_{10}\langle\mathcal{N}\rangle_{20}(0)}{\beta_{20}\langle\mathcal{N}\rangle_{10}(0)+\beta_{10}\langle\mathcal{N}\rangle_{20}(0)} \\ &= \tau_2^{-1}(0) - g_1 k_{nr}(0) \end{aligned} \tag{62}$$

while the decay time $\tau_2(0)$ can be obtained from the single exponential decay curve of the higher energetic emission upon excitation into state $|2\rangle$

$$\tau_2(0) = \frac{\int_0^\infty dt\ t\langle\mathcal{N}\rangle_{20}(t,0)}{\int_0^\infty dt\ \langle\mathcal{N}\rangle_{20}(t,0)} \tag{63}$$

It is noteworthy that Equations (61) and (62) also account for the limiting cases that the decay from state $|2\rangle$ can be either purely radiative or non-radiative, respectively. This case is translated to the presence of only one observable radiative transition in the luminescence spectrum. Accordingly, the relative errors on the experimental determination of $k_{nr}(0)$ or $k_{2r}(0)$, respectively, are dependent on the relative uncertainties of the luminescence intensities, represented by $\langle\mathcal{N}\rangle_{10}(0)$ and $\langle\mathcal{N}\rangle_{20}(0)$, respectively.

Once all intrinsic decay rates have been established with aid of Equations (57)–(63), it is in principle possible to predict the rates at arbitrarily higher temperatures by Equations (41)–(43) if the effective vibrational energy $\hbar\omega_{eff}$ is known. In particular,

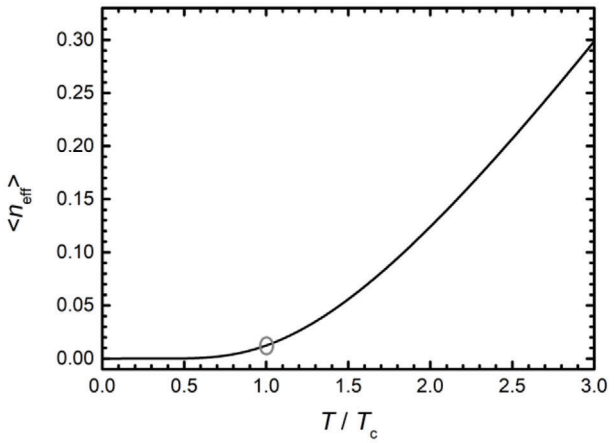

Figure 10. Plot of the Planck factor $\langle n_{\text{eff}} \rangle$ versus temperature. The critical temperature T_c at which the graph of $\langle n_{\text{eff}} \rangle$ has its maximum curvature is indicated.

it is even possible to assess the not straightforwardly measurable non-radiative absorption rate $k_{\text{nr}}^{\text{abs}}(T)$ by means of $k_{\text{nr}}(0)$ with aid of Equation (42). Independently, the presented analysis is also extendable to any higher temperature if the approximation $k_{\text{nr}}^{\text{abs}}(T) \approx 0$ is valid. The temperature at which breakdown of that approximation occurs can be experimentally verified by different means. One of the most straightforward proofs is the measurement of a luminescence spectrum upon direct excitation into the lower energetic excited state $|1\rangle$. Any observation of a higher energetic emission band arising from thermal population of state $|2\rangle$ indicates that $k_{\text{nr}}^{\text{abs}}(T) \neq 0$. The appearance of the corresponding luminescence decay curves will then deviate from the ideal shape as depicted in Figure 9.

The suitability range of the approximation $k_{\text{nr}}^{\text{abs}}(T) \approx 0$ may be at least roughly predicted by definition of that critical temperature T_c at which both $\langle n_{\text{eff}} \rangle$ and $1 + \langle n_{\text{eff}} \rangle$ show their maximum curvature. The corresponding temperature is governed by the numerical solution of the following equation (see Supporting Information for the derivation)

$$\sqrt{3}\left(\frac{\hbar\omega_{\text{eff}}}{2k_{\text{B}}T_{\text{c}}}\coth\left(\frac{\hbar\omega_{\text{eff}}}{2k_{\text{B}}T_{\text{c}}}\right)-1\right)-\frac{\hbar\omega_{\text{eff}}}{2k_{\text{B}}T_{\text{c}}}=0 \tag{64}$$

which yields the upper bound

$$T \leq T_{\text{c}} \approx 0.2227\frac{\hbar\omega_{\text{eff}}}{k_{\text{B}}} \tag{65}$$

and may serve as an estimate for the temperature validity regime of $k_{\text{nr}}^{\text{abs}}(T) \approx 0$. For $T > T_c$, $\langle n_{\text{eff}} \rangle$ starts to increase more rapidly until it grows linearly with T (see **Figure 10**). In that case, the nonradiative absorption rate cannot be neglected anymore and the two excited states $|1\rangle$ and $|2\rangle$ start becoming thermally coupled. As expected, the threshold temperature T_c increases with increasing effective vibrational energy. Except for heavy halides or chalcogenides with smallest optical phonon energies of around 150 cm^{-1}, in which the lowest threshold temperature is around 50 K, the decay analysis in most inorganic hosts can be already verified at liquid N_2 temperatures (≈70–80 K). This temperature range is typically sufficient to fulfill the approximation $k_{\text{nr}}^{\text{abs}}(T) \approx 0$.

Equation (65) can be easily generalized to the case of multiphonon processes. If the energy gap ΔE_{21} is bridged by p phonons of energy $\hbar\omega_{\text{eff}}$, the corresponding threshold temperature for appreciable thermal excitation of the phonon modes increases to pT_c (see Supporting Information for a proof). Thus, typically for $p > 4$ and a phonon energy $\hbar\omega_{\text{eff}} \gg k_{\text{B}}T$, the non-radiative transition rates $k_{\text{nr}}(T)$ can become so small that they become negligible compared to the radiative decay rates. The coupled rate equation system (56) is diagonalized in that case and the two excited states are not thermally coupled anymore. Both states $|1\rangle$ and $|2\rangle$ then decay purely radiatively and can be treated as two thermally isolated states (see **Figure 11**a). Thus, for any Boltzmann thermometer, the energy gap ΔE_{21}, the phonon energy $\hbar\omega_{\text{eff}}$ and the thermal energy $k_{\text{B}}T$ must be of similar order of magnitude. While the previously described elucidation of the different radiative and nonradiative rates is best performed if $\Delta E_{21} \gtrsim \hbar\omega_{\text{eff}} \gg k_{\text{B}}T$ (see Figure 11b), Boltzmann thermometry is best performed at the condition $\Delta E_{21} \gtrsim \hbar\omega_{\text{eff}} \gg k_{\text{B}}T$ (see Figure 11c). This again demonstrates that Boltzmann thermometers generally only perform well in a limited temperature range. It is noteworthy that at very high temperatures, Boltzmann thermometry is practically disturbed by the gradual shift of thermal blackbody radiation background into the visible range that can pose problems to an accurate determination of the luminescence intensities of interest. Moreover, thermalization with higher lying states will also occur. In that regard, the excited two state system is only an idealized model system and Boltzmann thermometry will have practical limitations also for high temperatures.

4.2. Temperature-Dependent Steady State Dynamics of Two Excited States–Generalization and Conditions for Failure of Boltzmann Thermometry

4.2.1. General Excited State Dynamics Model for Two Thermally Coupled Excited States

An immediate consequence from the kinetic analysis of the previous section is that at temperatures below T_c, the Boltzmann distribution may not be sustained anymore since the nonradiative absorption rate from the excited state $|1\rangle$ to $|2\rangle$ then becomes negligible. According to Equation (50), this is especially serious if the nonradiative transition rate has a MD-type character since the intrinsic nonradiative rate $k_{\text{nr}}(0)$ is not sufficiently high to compensate the effect from the very small Planck factor $\langle n_{\text{eff}} \rangle$ then. Overall, any ion luminescent thermometer based on Boltzmann equilibrium among the excited states will fail at sufficiently low temperatures once the nonradiative transition rates $k_{\text{nr}}^{\text{abs}}(T)$ and $k_{\text{nr}}^{\text{em}}(T)$ become comparable to the radiative rates $k_{1\text{r}}$ and $k_{2\text{r}}$. According to Section 2.6, this is especially a problem for luminescent ions with two excited states thermalizing via a magnetic dipole-type nonradiative transition. Knowledge about these limitations does not only provide a mechanistically more elaborate picture of the performance of a luminescent thermometer over a very wide temperature range, it also offers guidelines for the kinetic control of a Boltzmann-based single ion luminescent thermometer.

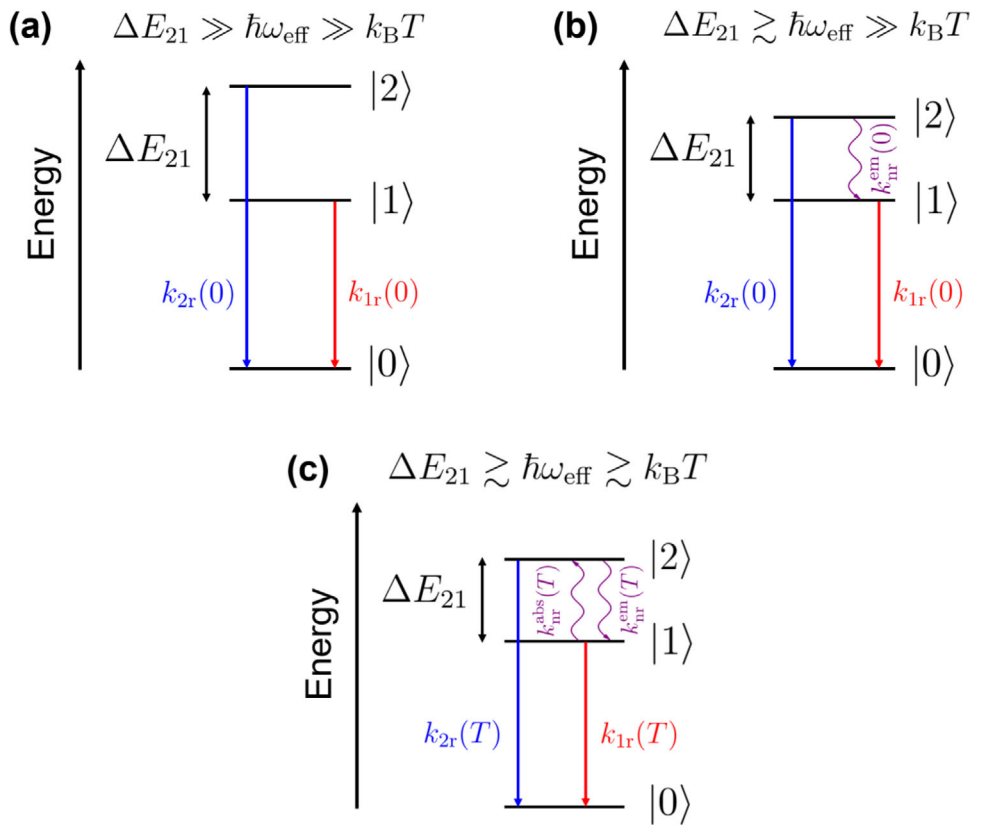

Figure 11. Different scenarios of excited state dynamics of a single ion luminescent thermometer dependent on the relative sizes of the energy gap ΔE_{21}, $\hbar\omega_{\text{eff}}$ and $k_B T$. a) If $\Delta E_{21} \gtrsim \hbar\omega_{\text{eff}} \gg k_B T$, the excited two states are thermally isolated and even spontaneous nonradiative emission from $|2\rangle$ to $|1\rangle$ is not favorable. The two states only decay radiatively and are isolated. b) If $\Delta E_{21} \gtrsim \hbar\omega_{\text{eff}} \gg k_B T$, spontaneous non-radiative emission from $|2\rangle$ to $|1\rangle$ occurs additionally. This is the situation to be met for the elucidation of all intrinsic decay rates. c) If $\Delta E_{21} \gtrsim \hbar\omega_{\text{eff}} \gg k_B T$, the two states $|2\rangle$ and $|1\rangle$ both populate each other non-radiatively. If the non-radiative rates supersede the radiative rates, thermodynamic equilibrium is achieved. This is the most desirable situation for a Boltzmann-based luminescence thermometer.

Reported examples for the observation of a kinetically induced failure of the Boltzmann distribution for thermometry are the luminescent $^5D_1 \rightarrow {}^7F_J$ and $^5D_0 \rightarrow {}^7F_J$ transitions of Eu^{3+} ($\Delta E_{21} \approx 1700$ cm^{-1})[135,198] or the $^4I_{15/2} \rightarrow {}^6H_{15/2}$ and $^4F_{9/2} \rightarrow {}^6H_{15/2}$ transitions of Dy^{3+} ($\Delta E_{21} \approx 1000$ cm^{-1})[135] at temperatures below around 550 and 400 K, respectively. In those cases, the temperature dependence of the intensity ratio is no longer governed by Boltzmann's law but must be accounted for by careful consideration of the generalized excited state dynamics instead. A generalized model for the steady-state kinetics of a two excited-state system has been recently presented and discussed in the case of Eu^{3+} by Geitenbeek et al.[198] A similar problem involving thermal coupling of the ^5D_J ($J = 0, 1, 2$) states of Sm^{2+} upon excitation into the excited $4f^5 5d^1$ configuration was also investigated in very much detail by Shen and Bray[181] and in the case of different non-offset $4f^{12}5d^1$ states of Tm^{2+} by Güdel et al.[186] In contrast to the indicated very specific cases, however, we will now derive a general excited state dynamical model that contains all those cases and allows for the elucidation of general guidelines.

The conditions for a ratiometric thermometry experiment were outlined in Section 2.2.1. Suppose that the previously introduced auxiliary state $|a\rangle$ is populated with population N_a from all present, non-interacting luminescent ions. Given that state $|a\rangle$ does not show any radiative emission, the relaxation rates from $|a\rangle$ to the states $|2\rangle$ and $|1\rangle$ can be approximated as $\alpha_{aj} K$ ($j = 1, 2$), respectively with the effective non-radiative decay rate K as introduced in Equation (10). The α_{aj} denote so-called feeding ratios. Very often, it is $\alpha_{a2} > \alpha_{a1} > 0$ due to the smaller energy gap between state $|a\rangle$ and $|2\rangle$ (compare to Equation (48)), although that specifically depends on the selection rules governing the non-radiative transitions $|a\rangle \rightarrow |2\rangle$ and $|a\rangle \rightarrow |1\rangle$ (see Section 2.5). If the thermally probed states are also energetically sufficiently separated from other lower lying electronic states and no intermediate states between $|a\rangle$ and $|2\rangle$ are present, it is even $\alpha_{a1} + \alpha_{a2} = 1$. Finally, we explicitly neglect any additional cross-relaxation effects among different spatially close ions (achievable by low doping concentrations), although they can be formally easily incorporated into the coupled rate equation system (56).[192] However, the additionally introduced parameters would distract from the main properties of the single ion luminescent thermometer, which is the focus of this work.

The steady-state conditions under the previously described preliminaries applied on the rate equation system (56) for the populations in the excited states $|1\rangle$ and $|2\rangle$ read

$$\begin{pmatrix} \alpha_{a1} K N_a \\ \alpha_{a2} K N_a \end{pmatrix} = \begin{pmatrix} k_{1r}(T) + k_{nr}^{abs}(T) & -k_{nr}^{em}(T) \\ -k_{nr}^{abs}(T) & k_{2r}(T) + k_{nr}^{em}(T) \end{pmatrix} \begin{pmatrix} N_1(T) \\ N_2(T) \end{pmatrix} \quad (66)$$

This system can be explicitly rearranged for a population ratio and by introduction of all temperature dependences (see Equations (41)–(43)), the generalized formula for the modified LIR is given by

$$R(T) = C\frac{N_2}{N_1} = C\frac{\alpha_{a2}k_{1r}(T) + \left(\alpha_{a1}+\alpha_{a2}\right)k_{nr}^{abs}(T)}{\alpha_{a1}k_{2r}(T) + \left(\alpha_{a1}+\alpha_{a2}\right)k_{nr}^{em}(T)} = C\frac{\alpha_{a2}k_{1r}(0)\left[1+\kappa\left(2\langle n_{eff}\rangle+1\right)\right] + \left(\alpha_{a1}+\alpha_{a2}\right)g_2k_{nr}(0)\langle n_{eff}\rangle^p}{\alpha_{a1}k_{2r}(0)\left[1+\kappa\left(2\langle n_{eff}\rangle+1\right)\right] + \left(\alpha_{a1}+\alpha_{a2}\right)g_1k_{nr}(0)\left(1+\langle n_{eff}\rangle\right)^p} \quad (67)$$

with C as defined in Equation (16), α_{a1} and α_{a2} as the previously defined feeding ratios from the auxiliary state $|a\rangle$ and κ as a measure for the strength of the electron-phonon coupling. An analogous formula has already been reported by Geitenbeek et al. earlier.[198]

It is instructive to analyze the meaning and limits of the generalized LIR according to Equation (67). It correctly contains the limit of the conventional Boltzmann distribution if the nonradiative transition rates are much larger than the radiative rates (i.e., if $k_{1r}(T)$, $k_{2r}(T) \ll k_{nr}(T)$). If $T > T_c$ (see Equation 65), the Planck factors start becoming the dominant terms in Equation (67). Factorization of $\langle n_{eff}\rangle$ from the nominator and $\langle n_{eff}\rangle + 1$ from the denominator then allows to make the terms containing the radiative rates $k_{1r}(0)$ and $k_{2r}(0)$ safely negligible, respectively. Finally, with Equation (39) and the remaining Planck factors from the nonradiative contributions in Equation (67), it is straightforward to recover the Boltzmann distribution as the limit of dominant nonradiative rates ($k_{nr}(T) \gg k_{jr}(T)$ with $j = 1, 2$),

$$R(T) \rightarrow C\exp\left(-\frac{\hbar\omega_{eff}}{k_B T}\right)\frac{g_2}{g_1}\exp\left(-\frac{(p-1)\hbar\omega_{eff}}{k_B T}\right) = C\frac{g_2}{g_1}\exp\left(-\frac{\Delta E_{21}}{k_B T}\right) \quad (68)$$

However, this analysis also demonstrates that the Boltzmann distribution is only expected above the threshold temperature T_c for a one-phonon or pT_c for a p-phonon transition, respectively (see Equation 65). At low temperatures, the validity of the Boltzmann distribution will critically depend on the relative size of the intrinsic transition rates. Only if $k_{1r}(0) \ll g_2k_{nr}(0)$ and $k_{2r}(0) \ll g_1k_{nr}(0)$, Boltzmann equilibrium is kinetically sustained down to lowest temperatures. This indicates that Boltzmann behavior can be controlled by appropriate engineering of the intrinsic nonradiative transition rate.

For the discussion of the generalized LIR irrespective of the specific luminescent ion, it is again helpful to reparametrize Equation (67) in terms of the variable r (see Equation 25). After some straightforward rearrangements, it follows

$$R(r) = C\frac{g_2}{g_1}\frac{\alpha_{a2}}{\alpha_{a1}}\cdot \frac{\frac{k_{1r}(0)}{g_2k_{nr}(0)}\left[1+\kappa\coth\left(\frac{r}{2p}\right)\right] + \left(1+\frac{\alpha_{a1}}{\alpha_{a2}}\right)\left[\frac{1}{2}\left(\coth\left(\frac{r}{2p}\right)-1\right)\right]^p}{\frac{k_{2r}(0)}{g_1k_{nr}(0)}\left[1+\kappa\coth\left(\frac{r}{2p}\right)\right] + \left(1+\frac{\alpha_{a2}}{\alpha_{a1}}\right)\left[\frac{1}{2}\left(\coth\left(\frac{r}{2p}\right)+1\right)\right]^p} \quad (69)$$

where Equation (36) was used for the Planck factors. This function is plotted for different phonon numbers p and consequently varying parameters $k_{nr}(0)$ (by the energy gap law, Equation 48) and α_{a1} and α_{a2} in **Figure 12**. Both the cases of negligible electron-phonon coupling ($\kappa \sim 0$, typical for trivalent lanthanides) and stronger electron–phonon coupling ($\kappa > 1$, typical for Cr^{3+}, Mn^{4+}, divalent lanthanides) are depicted in Figure 12. It is clearly observed that the Boltzmann regime generally shifts to successively lower values of r (i.e., into the regime of higher temperatures $T > pT_c$) for higher phonon numbers p. This is expected as the intrinsic non-radiative rate exponentially decreases with p and the radiative rates become dominant instead. Once the Planck factors become non-negligible (if $T > pT_c$), the nonradiative transition rate quickly increases, and Boltzmann equilibrium can be kinetically sustained. In the case of strong electron–phonon coupling (Figure 12b), breakdown of the Boltzmann equilibrium is even more severe since the radiative rate also increases with increasing. This result demonstrates the potential that trivalent lanthanides have for the field of single ion luminescence thermometry besides their practically beneficial property of narrow line luminescence with weakly overlapping transitions.

The critical dependence on the number of phonons p in order to bridge the gap confirms the findings from Section 2.6 and clearly suggests choosing hosts with sufficiently high phonon energies such that the energy gap ΔE_{21} is best bridged by only one or two phonons. For high phonon numbers, the temperature range, in which Boltzmann equilibrium is sustained, can even shift above the optimum temperature range. This occurs for ions with large energy gaps ΔE_{21} between the two thermally coupled excited states if they are additionally doped into host compounds with low phonon energies. A representative example for that is the $^5D_1$–$^5D_0$ gap of Eu^{3+} in hosts such as β-$NaYF_4$ or Y_2O_3.[135,198] An immediate conclusion is that Eu^{3+} is rather useful for ratiometric luminescence thermometry at high temperatures if doped in high energy phonon hosts such as phosphates or borates.

For successively higher phonon numbers p, the LIR $R(r)$ goes through a minimum before Boltzmann behavior evolves at low r or high temperatures T (see Figure 12). This apparently strange behavior is a consequence of the early onset of stimulated phonon emission for low phonon energies. With gradually decreasing r (or, alternatively, increasing temperatures), stimulated phonon emission from state $|2\rangle$ to $|1\rangle$ may set in above T_c, which is lower for successively lower phonon energies $\hbar\omega_{eff}$. According to Equation (65), the corresponding r_c is given by $r_c = 1/0.2227 \approx 4.491$. In that case, the LIR decreases because of the quickly increasing stimulated phonon emission rate that populates state $|1\rangle$. In the range of the temperature pT_c (or at $r_c/p \approx 4.491/p$),

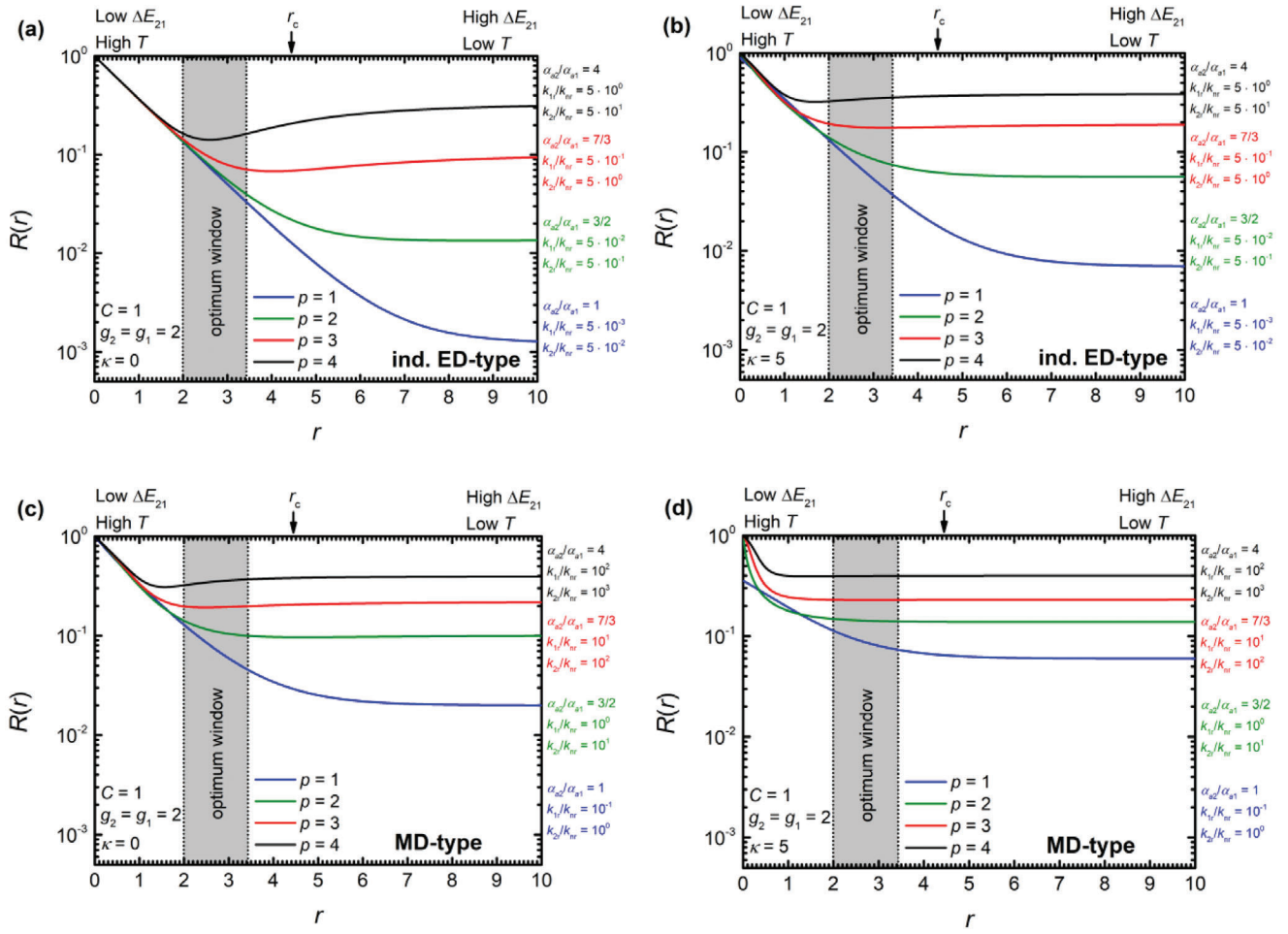

Figure 12. a) Generalized universal plots of the LIR, $R(r)$, in terms of the variable $r = \Delta E_{21}/k_B T$ upon explicit inclusion of radiative decay (see Equation 69). The following cases are depicted: a) induced electric dipole-type nonradiative transitions without electron-phonon coupling ($\kappa = 0$), b) induced electric dipole-type non-radiative transitions with stronger electron-phonon coupling ($\kappa = 5$), c) magnetic dipole-type nonradiative transitions without electron–phonon coupling ($\kappa = 0$), and d) magnetic dipole-type nonradiative transitions with stronger electron-phonon coupling ($\kappa = 5$). The exemplary parameters are denoted in the graph and varied with p to produce physically meaningful plots. The threshold value r_c for the onset of the Planck factors (see Equation 65) is also specified.

a minimum LIR is observed and stimulated phonon absorption from state $|1\rangle$ to $|2\rangle$ becomes competitive, while at temperatures above pT_c, Boltzmann equilibrium is sustained (see Figure 12). Although not exact, the value of pT_c or, alternatively, r_c/p gives a very good estimate for the onset temperature or onset value of r, above which Boltzmann equilibrium is kinetically favored. The value pT_c is a rather precise estimate for magnetic dipole-type nonradiative transitions with low intrinsic transition rates $k_{nr}(0)$, while it typically overestimates the onset temperature for Boltzmann behavior for (induced) electric dipole-type transitions with higher intrinsic nonradiative transition rates $k_{nr}(0)$ (see Equations (50) and (51) and also Figure 12a,c). This is understandable since for magnetic dipole-type nonradiative transitions, the magnitude of the transition rate is dominated by the Planck factor while for electric dipole-type transitions, the intrinsic transition rate $k_{nr}(0)$ is already high and thus, also dominates the overall nonradiative transition rate even at temperatures below activation of the Planck factor at pT_c.

4.2.2. Practical use of the Generalized Excited State Dynamics Model of the LIR

The generalized LIR, $R(T)$, as given in Equation (67) is not readily practical for use as a non-linear fitting model to simple luminescence thermometry data as any lack of knowledge on the transition rates requires many fitting parameters to be fitted. Convergence to a global minimum of the non-linear fit with physically meaningful values seems almost impossible then. Section 4.1 describes the necessary prescriptions to determine and fix many of the physical parameters in Equation (67) beforehand by very simple luminescence experiments. We thus aimed at a user-friendly version of the generalized excited state dynamics model with as

few fitting parameters as possible to make the non-linear fit stable. If the LIR is measured as prescribed in Equation (16), Equation (67) can be rearranged to

$$R(T) = C\frac{g_2}{g_1}\frac{\alpha_{a2}}{\alpha_{a1}} \cdot \frac{\frac{\beta_{20}}{\beta_{10}C}\left(\frac{1}{\phi_1(0)}-1\right)\left[1+\kappa\left(2\langle n_{\text{eff}}\rangle+1\right)\right]+\left(1+\frac{\alpha_{a1}}{\alpha_{a2}}\right)\langle n_{\text{eff}}\rangle^p}{\left(\frac{1}{\phi_1(0)}-1\right)\left[1+\kappa\left(2\langle n_{\text{eff}}\rangle+1\right)\right]+\left(1+\frac{\alpha_{a2}}{\alpha_{a1}}\right)\left(1+\langle n_{\text{eff}}\rangle\right)^p} \tag{70}$$

where the Planck factors are defined in Equation (36). $\phi_1(0)$ is the relative quantum yield of the lower energetic radiative transition upon selective excitation into state $|2\rangle$ as defined in Equation (60) and can be obtained from a conventional luminescence spectrum at the temperature $T < T_c$ (i.e., if $r > r_c = 4.491$). β_{10} and β_{20} are the luminescence branching ratios of the radiative transitions of interest also obtainable from a luminescence spectrum over a wide wavelength range that captures all radiative transitions from the excited states $|1\rangle$ or $|2\rangle$ to lower energy levels, respectively. Alternatively, they are also accessible from Judd-Ofelt calculations in the case of trivalent lanthanides. The phonon number p is restricted to integer values only and is typically known preliminarily, since the energy gap ΔE_{21} is also spectroscopically accessible from an absorption or photoluminescence excitation spectrum. Thus, the number of independent fitting parameters reduces to two or three: The pre-factor C, the ratio α_{a2}/α_{a1} and the electron-phonon coupling strength κ. For trivalent lanthanides, it is even possible to neglect κ such that only two independent fitting parameters are present. In the case of strong electron-phonon coupling, a good estimate on κ is obtained from the ratio of photon counts of the zero-phonon line compared to the vibronic sidebands in the emission spectra.

The preconstant C can be fixed by independent luminescence decay experiments at temperatures below T_c. In the special case of trivalent lanthanides, both C and the emission branching ratios can alternatively be determined by Judd-Ofelt theory with, e.g., the packages RELIC,[219] JOES,[220] LUMPAC[228,229] or, in principle also BonnMag[237–241] (see Equation 21). On the other hand, C can be independently obtained from the intercept of a Boltzmann plot in the validity regime of the Boltzmann equilibrium (see Figure 12), since

$$\lim_{T\to\infty} R(T) = \lim_{r\to 0} R(r) = C\frac{g_2}{g_1} = \frac{g_2\beta_{20}k_{2r}(0)}{g_1\beta_{10}k_{1r}(0)} \tag{71}$$

Another commonly encountered practical problem is a very low luminescence intensity of the radiative transition $|2\rangle \rightarrow |0\rangle$ at low temperatures, i.e., if the relative quantum yield for the lower energetic emission, $\phi_1(0)$, is close to 1. This can pose a problem in the experimental determination of the decay time $\tau_2(0)$ and the radiative decay rate $k_{2r}(0)$. By knowledge of the pre-factor C and the easily obtainable radiative decay rate $k_{1r}(0)$ of the lower excited state $|1\rangle$, it is possible to independently determine $k_{2r}(0)$, which in turn allows the determination of $k_{nr}(0)$ by Equations (61) and (62). Thus, luminescence thermometry also helps elucidate the different transition rates governing the kinetics of the two excited states of interest.

A final problem is the determination of the ratio of the non-radiative feeding parameters, α_{a2}/α_{a1}. Dependent on the relative size of the two separate feeding ratios, this parameter can vary from very small to very large numbers, which makes the judgment of the obtained fitting value difficult in practice. However, an alternative check is possible from a measurement of the LIR at temperatures $T < T_c$, at which the LIR evolves into a constant plateau (high values of r in Figure 12). In the limit $T \rightarrow 0$, $\langle n_{\text{eff}}\rangle$ expectedly becomes 0. Thus, it is

$$\lim_{T\to 0} R(T) = \lim_{r\to\infty} R(r) = \frac{g_2\beta_{20}}{g_1\beta_{10}}\cdot\frac{\alpha_{a2}}{\alpha_{a1}} \cdot \frac{\left(\frac{1}{\phi_1(0)}-1\right)(1+\kappa)}{\left(\frac{1}{\phi_1(0)}-1\right)(1+\kappa)+\left(1+\frac{\alpha_{a2}}{\alpha_{a1}}\right)} := R(0) \tag{72}$$

which can be rearranged for the ratio α_{a2}/α_{a1},

$$\frac{\alpha_{a2}}{\alpha_{a1}} = \frac{\left[1+\left(\frac{1}{\phi_1(0)}-1\right)(1+\kappa)\right]R(0)}{\frac{g_2\beta_{20}}{g_1\beta_{10}}\left(\frac{1}{\phi_1(0)}-1\right)(1+\kappa)-R(0)} \tag{73}$$

Both Equations (71) and (73) offer the possibility of independent verification of the obtained fitting parameters C and α_{a2}/α_{a1} or, if the respective luminescence spectra are acquired, even the potential to fully simulate the whole temperature evolution of the LIR, as was already demonstrated in the case of Eu^{3+}.[198]

4.3. Guidelines to Sustain Boltzmann Behavior over a Wide Temperature Range

The kinetic analysis of a single ion luminescent thermometer allows to set up additional guidelines for a desirable control of the Boltzmann equilibrium over a possibly wide temperature range, but in particular within the optimum window according to the previous thermodynamic analysis (see Section 2.3). A first simple conclusion arises from the general onset of the Boltzmann behavior above temperatures of pT_c or, alternatively, r_c/p with $r_c \approx 4.41$. In order to ensure that Boltzmann behavior is clearly present in the optimum window $r \in [2, 2+\sqrt{2}]$, it is necessary that r_c/p is larger than the two boundaries. This puts a kinetic restriction on the advisable phonon number to bridge the energy gap ΔE_{21}. For the higher boundary, it follows

$$p_{\text{high}} \leq \left\lfloor \frac{r_c}{2+\sqrt{2}} \right\rfloor \approx \lfloor 1.32 \rfloor = 1 \tag{74}$$

while the lower boundary affords

$$p_{\text{low}} \leq \left\lfloor \frac{r_c}{2} \right\rfloor \approx \lfloor 2.25 \rfloor = 2 \tag{75}$$

with $\lfloor x \rfloor$ as the Gaussian floor function rounding off to the next lower integer. These rules exactly agree with the findings of Section 2.6. From a kinetic perspective, nonradiative transitions over

ΔE_{21} involving more than two phonons should be clearly avoided since otherwise a thermodynamically optimum performance of a Boltzmann thermometer cannot be guaranteed anymore (see also Figure 12).

It was indicated in Section 2.6 that a two-phonon nonradiative transition should yet be favored in the case that the quenching state $|q\rangle$ is energetically close to the lower energetic excited state $|1\rangle$ in order to lower probability for multi-phonon relaxation to $|q\rangle$. A possibility to release restriction (74) is an increase of the intrinsic non-radiative transition rate $k_{nr}(0)$ itself. According to the estimate (50), this is only possible for an (induced) electric dipole-type nonradiative transition since then pT_c is an overestimate of the onset of Boltzmann behavior of the LIR (see Figure 12a). A well-known example for that underlying principle is the $^2H_{11/2}$–$^4S_{3/2}$ energy gap of Er^{3+} ($\Delta E_{21} \approx 700\ cm^{-1}$). The most conventionally used host material for Er^{3+} is β-$NaYF_4$ with a cut-off phonon energy of around 450 cm^{-1},[283], i.e., the $^2H_{11/2}$–$^4S_{3/2}$ energy gap of Er^{3+} can only be bridged by two phonons in that host compound. A low energy phonon host is mandatory since otherwise efficient non-radiative relaxation to the next lower red-emitting $^4F_{9/2}$ level ($\Delta E_{1q} \approx 3100\ cm^{-1}$) takes place, which would destroy the efficient thermometric performance of $^2H_{11/2}$–$^4S_{3/2}$ energy gap of Er^{3+}. Boltzmann behavior of the LIR of the two green $^2H_{11/2} \rightarrow {}^4I_{15/2}$ and $^4S_{3/2} \rightarrow {}^4I_{15/2}$ transitions is formally expected only to set in above $pT_c \approx 230$ K. However, it was reported that thermalization between the $^2H_{11/2}$ and $^4S_{3/2}$ levels can be even observed down to $T \approx 130$–140 K in the case of YVO_4:Er^{3+} having a higher phonon energy.[247] This specialty can be understood from the high value of the reduced electric dipole matrix element $\langle \| U^{(4)} \| \rangle^2 = 0.2002$ dominating the non-radiative transition dipole moment of the $^2H_{11/2} \leftrightarrow {}^4S_{3/2}$ transition.[217] β-$NaYF_4$ gives rise to a sufficiently high Ω_4 Judd-Ofelt parameter ($\Omega_4 \approx 1.16 \times 10^{-20}\ cm^2$)[248] and thus favors an efficient electric dipole-type non-radiative transition among those two spin-orbit levels. This is the underlying mechanistic reason for the success of β-$NaYF_4$:Er^{3+}, Yb^{3+} as a sensitive luminescence thermometer even below room temperature despite a nonradiative transition requiring two phonon modes that would naively be expected to lead to a kinetically induced failure of the Boltzmann equilibrium at temperatures below 230 K. Overall, electric dipole-type non-radiative transitions are generally beneficial for a good performance of any Boltzmann thermometer. In the case of magnetic dipole-type nonradiative transitions connecting the thermally coupled excited levels (as suggested by strong reduced matrix elements $\langle \| \boldsymbol{L} + g_S \boldsymbol{S} \| \rangle^2$ for the respective transition,[218] see Equation (20)), the restrictions (74) and (75) should be followed seriously and one-phonon non-radiative transitions are strongly recommendable for temperature measurements above 200 K, as also suggested by the flowcharts in Figure 7b.

5. Conclusions

Luminescence thermometry is a quickly emerging application sector for remote and sensitive temperature sensing. Despite extensive and vibrant experimental research, the theoretical foundations and design principles for optimum performance of luminescent thermometers are virtually nonexistent. Herein, a general theoretical framework for ratiometric single ion luminescence thermometers is elucidated that is applicable to any luminescent ion showing multiphonon nonradiative transitions. Typical representatives are the trivalent lanthanides with their $4f^n$–$4f^n$ transitions, Cr^{3+} or Mn^{4+} with intraconfigurational $3d^3$–$3d^3$ nonradiative transitions or divalent lanthanides with either intraconfigurational $4f^n$–$4f^n$ or $4f^{n-1}5d^1$–$4f^{n-1}5d^1$ nonradiative transitions.

Starting from a fundamental derivation of the proper definition of a LIR obtained in modern luminescence spectrometers, three main conclusions can be drawn from the developed theoretical framework and are shown to result in design rules for optimized performance of single ion luminescence thermometers. By straightforward mathematics, it was possible to derive that any Boltzmann thermometer with energy gap ΔE_{21} shows its optimum thermal response at the temperature $T_{opt} = \Delta E_{21}/2k_B$. Together with a desirable high relative sensitivity S_r, it could be elucidated that Boltzmann thermometers can only perform under optimum conditions up to a temperature $T_0 < 2/S_r$. Above, it is advisable to sacrifice a bit of thermal response to achieve a higher gain in relative sensitivity by increasing the energy gap to $\Delta E_{21} = 3.41 k_B T_0$. In turn, every single ion Boltzmann-based thermometer is best suited for a limited temperature range only, which depends on the chosen energy gap between the two thermally coupled excited states. The optimization strategy is based on the principle that it is not only the relative sensitivity S_r that should be high, but there should be a balance between signal-measurable changes in the LIR and the relative sensitivity. This simple concept results in user-friendly guidelines on both an advisable energy gap ΔE_{21} and the exponential pre-factor C governing the electronic properties of the two excited states. For temperature measurements at $\Delta E_{21} = 3.41 k_B T_0$, it was elucidated that the most recommendable value for the pre-factor is given as $C\frac{g_2}{g_1} = 21.5$ to compensate for the thermally low emission intensity of the higher excited energy state $|2\rangle$ and relax the requirement on a high emission intensity. In the case of the lanthanides, such an optimization is possible by a Judd-Ofelt analysis of the embedding host material. It is particularly recommendable in the field of nanothermometry, in which low quantum efficiencies and the impact of the surface-attached ligands generally lower the observable emission intensities.

The second part dealt with a critical verification of the validity of the linearization of the Boltzmann distribution for narrow temperature regimes for the sake of simpler calibration. This is especially employed in the field of in vivo thermometry without justification. A general formula for the linearized version of Boltzmann's law was derived and it was assessed that it is only accompanied with minimum relative errors in the regime $\Delta E_{21} < k_B T$ such as for the crystal field states of $4f^n$ spin-orbit levels of the trivalent lanthanides. In fact, a linearized plot is then even advisable since the LIR is then more robust towards a statistical uncertainty of the LIR than the conventional (and actual) exponential temperature dependence of the Boltzmann distribution. The validity regime for a linearization of the Boltzmann distribution is, however, incompatible with the more important requirement for optimum performance of the luminescent thermometer at $\Delta E_{21} = 2k_B T - 3.41 k_B T$.

In the third part, the excited state kinetics of a Boltzmann thermometer was analyzed. Boltzmann equilibrium is only sustained if the nonradiative transitions are much faster than the radiative decay pathways. Thus, in order to guarantee a

Boltzmann behavior of the LIR over a wide temperature range, it is necessary to understand the parameters that govern non-radiative transition rates. It was derived that Boltzmann thermometry is only meaningful if the energy gap ΔE_{21} is bridged by one or two phonons, while a requirement of more than three phonons kinetically inhibits thermal coupling over a wide temperature range. A generalized description of the temperature evolution of the LIR including both the non-radiative and radiative decay pathways was derived that is applicable for single-ion luminescent thermometers and at all temperatures (with or without Boltzmann equilibrium). It could be shown that the temperature-dependent part of the nonradiative transition rates sets in above a threshold temperature $T_c \approx 0.2227 \bullet \hbar\omega_{eff}/k_B$ with $\hbar\omega_{eff}$ as the effective host phonon energy that is absorbed or emitted during the non-radiative transition. For p necessary phonons to bridge ΔE_{21}, Boltzmann behavior is expected to set in above a temperature of pT_c, which clearly favors one- or two-phonon transitions among the thermally coupled excited states. This kinetically motivated concept provides a clear guideline for the maximum phonon energy in a suitable host material for a luminescent ion of interest for the purpose of luminescence thermometry.

Nonradiative rates can be interpreted in terms of a coupling between an electronic transition dipole moment connecting the two excited levels of interest and the induced electromagnetic field components arising from the vibration of the surrounding ligands of the luminescent activator in a host. This interpretation does not only give rise to electric dipole-type, but also magnetic dipole-type nonradiative transitions and allows to use the conventionally known quantum mechanical selection rules for radiative transitions in order to qualitatively assert the expected non-radiative transition rates. In particular, it was demonstrated that magnetic dipole-type transitions are two to three orders of magnitude lower than induced electric dipole-type transitions such that the former easily become comparable to radiative decay rates. Thus, an alternative to realize Boltzmann behavior at lower temperatures than pT_c is to select levels with intrinsic (induced) electric dipole-type non-radiative transition rates, such as the well-known $^2H_{11/2}$–$^4S_{3/2}$ levels of Er^{3+}. In case of electric dipole-type non-radiative transitions, also two-phonon processes (instead of one-phonon) are capable to still give rise to Boltzmann behavior over a wider temperature range. The lower maximum phonon energy helps reduce quenching of the luminescence by multi-phonon relaxation to lower energetic quenching states.

In summary, a comprehensive and universal theoretical framework of single ion luminescence thermometers was established. Not only provides it justification for many experimentally observed properties of Boltzmann thermometers, it also offers a full set of basic, user-friendly guidelines for an optimized performance of a Boltzmann thermometer. This helps avoid time-consuming trial and error attempts and rather allows specific design of luminescent thermometers dependent on the desired relative sensitivity and temperature range to be covered.

Supporting Information

Supporting Information is available from the Wiley Online Library or from the author.

Acknowledgements

The authors acknowledge funding from the European Union-Horizon 2020-FET-Open project NanoTBTech (grant agreement no.: 801305). Moreover, they thank the other consortium members of this project for fruitful input and the motivating support in development of this extensive work. Benoît Fond, Robin G. Geitenbeek, Freddy T. Rabouw, Thomas P. van Swieten and Harold W. de Wijn are also acknowledged for their interest in this work and many stimulating discussions.

Conflict of Interest

The authors declare no conflict of interest.

Keywords

Boltzmann distribution, excited state dynamics, luminescence thermometry

Received: July 29, 2020
Revised: September 15, 2020
Published online: October 12, 2020

[1] S. W. Allison, G. T. Gillies, *Rev. Sci. Instrum.* **1997**, *68*, 2615.
[2] P. R. N. Childs, J. R. Greenwood, C. A. Long, *Rev. Sci. Instrum.* **2000**, *71*, 2959.
[3] General Conference on Weights and Measures (CGPM), On the revision of the International Systems of Units (SI), **2018** (accessed October 2, 2020).
[4] General Conference on Weights and Measures (CGPM), Information for users about the redefinition of the SI, **2019** (accessed October 2, 2020).
[5] V. K. Rai, *Appl. Phys. B* **2007**, *88*, 297.
[6] Y. Gao, Y. Bando, Z. Liu, D. Golberg, H. Nakanishi, *Appl. Phys. Lett.* **2003**, *83*, 2913.
[7] Y. B. Li, Y. Bando, D. Golberg, Z. W. Liu, *Appl. Phys. Lett.* **2003**, *83*, 999.
[8] N. W. Gong, M. Y. Lu, C. Y. Wang, Y. Chen, L. J. Chen, *Appl. Phys. Lett.* **2008**, *92*, 73101.
[9] J. M. R. Weaver, L. M. Walpita, H. K. Wickramasinghe, *Nature* **1989**, *342*, 783.
[10] K. Luo, R. W. Herrick, A. Majumdar, P. Petroff, *Appl. Phys. Lett.* **1997**, *71*, 1604.
[11] A. Majumdar, *Annu. Rev. Mater. Sci.* **1999**, *29*, 505.
[12] L. Shi, S. Plyasunov, A. Bachtold, P. L. McEuen, A. Majumdar, *Appl. Phys. Lett.* **2000**, *77*, 4295.
[13] S. Sadat, A. Tan, Y. J. Chua, P. Reddy, *Nano Lett.* **2010**, *10*, 2613.
[14] M. A. Khan, C. Allemand, T. W. Eagar, *Rev. Sci. Instrum.* **1991**, *62*, 392.
[15] M. A. Khan, C. Allemand, T. W. Eagar, *Rev. Sci. Instrum.* **1991**, *62*, 403.
[16] Y. Xiao, C. Wan, A. Shahsafi, J. Salman, Z. Yu, R. Wambold, H. Mei, B. E. R. Perez, W. Derdeyn, C. Yao, M. A. Kats, *Laser Photonics Rev.* **2020**, *14*, 1900443.
[17] S. W. Allison, *Meas. Sci. Technol.* **2019**, *30*, 72001.
[18] S. F. Collins, G. W. Baxter, S. A. Wade, T. Sun, K. T. V. Grattan, Z. Y. Zhang, A. W. Palmer, *J. Appl. Phys.* **1998**, *84*, 4649.
[19] S. A. Wade, S. F. Collins, G. W. Baxter, *J. Appl. Phys.* **2003**, *94*, 4743.
[20] O. S. Wolfbeis, *Adv. Mater.* **2008**, *20*, 3759.
[21] Y. Yue, X. Wang, *Nano Rev.* **2012**, *3*, 11586.
[22] A. H. Khalid, K. Kontis, *Sensors* **2008**, *8*, 5673.

[23] C. Abram, B. Fond, F. Beyrau, *Prog. Energy Combust. Sci.* **2018**, *64*, 93.
[24] C. Gota, K. Okabe, T. Funatsu, Y. Harada, S. Uchiyama, *J. Am. Chem. Soc.* **2009**, *131*, 2766.
[25] K. M. McCabe, M. Hernandez, *Pediatr. Res.* **2010**, *67*, 469.
[26] C. D. S. Brites, P. P. Lima, N. J. O. Silva, A. Millán, V. S. Amaral, F. Palacio, L. D. Carlos, *Nanoscale* **2012**, *4*, 4799.
[27] D. Jaque, F. Vetrone, *Nanoscale* **2012**, *4*, 4301.
[28] K. Okabe, N. Inada, C. Gota, Y. Harada, T. Funatsu, S. Uchiyama, *Nat. Commun.* **2012**, *3*, 705.
[29] X.-d. Wang, O. S. Wolfbeis, R. J. Meier, *Chem. Soc. Rev.* **2013**, *42*, 7834.
[30] D. Jaque, B. del Rosal, E. M. Rodríguez, L. M. Maestro, P. Haro-González, J. G. Solé, *Nanomedicine* **2014**, *9*, 1047.
[31] T.-M. Liu, J. Conde, T. Lipiński, A. Bednarkiewicz, C.-C. Huang, *NPG Asia Mater* **2016**, *8*, e295.
[32] M. D. Dramićanin, *Methods Appl. Fluoresc.* **2016**, *4*, 42001.
[33] L. Marciniak, A. Bednarkiewicz, D. Kowalska, W. Strek, *J. Mater. Chem. C* **2016**, *4*, 5559.
[34] E. Hemmer, A. Benayas, F. Légaré, F. Vetrone, *Nanoscale Horiz.* **2016**, *1*, 168.
[35] C. D. S. Brites, A. Millán, L. D. Carlos in *Handbook on the Physics and Chemistry of Rare Earths, Vol. 49* (Eds: J. -C. G. Bünzli, V. K. Pecharsky), Elsevier, Amsterdam **2016**, pp. 339–427.
[36] B. del Rosal, E. Ximendes, U. Rocha, D. Jaque, *Adv. Opt. Mater.* **2017**, *5*, 1600508.
[37] C. D. S. Brites, S. Balabhadra, L. D. Carlos, *Adv. Opt. Mater.* **2019**, *7*, 1801239.
[38] J. Lee, N. A. Kotov, *Nano Today* **2007**, *2*, 48.
[39] M. Quintanilla, L. M. Liz-Marzán, *Nano Today* **2018**, *19*, 126.
[40] J. M. Taylor, P. Cappellaro, L. Childress, L. Jiang, D. Budker, P. R. Hemmer, A. Yacoby, R. Walsworth, M. D. Lukin, *Nat. Phys.* **2008**, *4*, 810.
[41] G. Balasubramanian, I. Y. Chan, R. Kolesov, M. Al-Hmoud, J. Tisler, C. Shin, C. Kim, A. Wojcik, P. R. Hemmer, A. Krueger, T. Hanke, A. Leitenstorfer, R. Bratschitsch, F. Jelezko, J. Wrachtrup, *Nature* **2008**, *455*, 648.
[42] V. M. Acosta, E. Bauch, M. P. Ledbetter, A. Waxman, L.-S. Bouchard, D. Budker, *Phys. Rev. Lett.* **2010**, *104*, 70801.
[43] G. Kucsko, P. C. Maurer, N. Y. Yao, M. Kubo, H. J. Noh, P. K. Lo, H. Park, M. D. Lukin, *Nature* **2013**, *500*, 54.
[44] P. Neumann, I. Jakobi, F. Dolde, C. Burk, R. Reuter, G. Waldherr, J. Honert, T. Wolf, A. Brunner, J. H. Shim, D. Suter, H. Sumiya, J. Isoya, J. Wrachtrup, *Nano Lett.* **2013**, *13*, 2738.
[45] N. Wang, G.-Q. Liu, W.-H. Leong, H. Zeng, X. Feng, S.-H. Li, F. Dolde, H. Fedder, J. Wrachtrup, X.-D. Cui, S. Yang, Q. Li, R.-B. Liu, *Phys. Rev. X* **2018**, *8*, 11042.
[46] M. S. J. Barson, P. Reddy, S. Yang, N. B. Manson, J. Wrachtrup, M. W. Doherty, *Phys. Rev. B* **2019**, *99*, 94101.
[47] G. W. Walker, V. C. Sundar, C. M. Rudzinski, A. W. Wun, M. G. Bawendi, D. G. Nocera, *Appl. Phys. Lett.* **2003**, *83*, 3555.
[48] P. A. S. Jorge, M. Mayeh, R. Benrashid, P. Caldas, J. L. Santos, F. Farahi, *Meas. Sci. Technol.* **2006**, *17*, 1032.
[49] S. Li, K. Zhang, J.-M. Yang, L. Lin, H. Yang, *Nano Lett.* **2007**, *7*, 3102.
[50] L. M. Maestro, E. M. Rodríguez, F. S. Rodríguez, M. C. I.-d. La Cruz, A. Juarranz, R. Naccache, F. Vetrone, D. Jaque, J. A. Capobianco, J. G. Solé, *Nano Lett.* **2010**, *10*, 5109.
[51] L. M. Maestro, C. Jacinto, U. R. Silva, F. Vetrone, J. A. Capobianco, D. Jaque, J. G. Solé, *Small* **2011**, *7*, 1774.
[52] P. Haro-González, L. Martínez-Maestro, I. R. Martín, J. García-Solé, D. Jaque, *Small* **2012**, *8*, 2652.
[53] L. M. Maestro, P. Haro-González, A. Sánchez-Iglesias, L. M. Liz-Marzán, J. García Solé, D. Jaque, *Langmuir* **2014**, *30*, 1650.
[54] E. C. Ximendes, U. Rocha, B. del Rosal, A. Vaquero, F. Sanz-Rodríguez, L. Monge, F. Ren, F. Vetrone, D. Ma, J. García-Solé, C. Jacinto, D. Jaque, N. Fernández, *Adv. Healthcare Mater.* **2017**, *6*, 1601195.
[55] B. del Rosal, D. Ruiz, I. Chaves-Coira, B. H. Juárez, L. Monge, G. Hong, N. Fernández, D. Jaque, *Adv. Funct. Mater.* **2018**, *28*, 1806088.
[56] H. D. A. Santos, D. Ruiz, G. Lifante, C. Jacinto, B. H. Juarez, D. Jaque, *Nanoscale* **2017**, *9*, 2505.
[57] X. Jiang, B. Q. Li, X. Qu, H. Yang, H. Liu, *J. Mater. Chem. B* **2017**, *5*, 8983.
[58] D. H. Ortgies, Á. L. García-Villalón, M. Granado, S. Amor, E. M. Rodríguez, H. D. A. Santos, J. Yao, J. Rubio-Retama, D. Jaque, *Nano Res.* **2019**, *12*, 749.
[59] D. Ruiz, M. Mizrahi, H. D. A. Santos, D. Jaque, C. M. S. Jones, J. Marqués-Hueso, C. Jacinto, F. G. Requejo, A. Torres-Pardo, J. M. González-Calbet, B. H. Juárez, *Nanoscale* **2019**, *11*, 9194.
[60] Y. Shen, J. Lifante, E. Ximendes, H. D. A. Santos, D. Ruiz, B. H. Juárez, I. Zabala Gutiérrez, V. Torres Vera, J. Rubio Retama, E. Martín Rodríguez, D. H. Ortgies, D. Jaque, A. Benayas, B. del Rosal, *Nanoscale* **2019**, *11*, 19251.
[61] A. Ortega-Rodríguez, Y. Shen, I. Zabala Gutierrez, H. D. A. Santos, V. Torres Vera, E. Ximendes, G. Villaverde, J. Lifante, C. Gerke, N. Fernández, O. G. Calderón, S. Melle, J. M. Hueso, D. Mendez-Gonzalez, M. Laurenti, C. Jones, J. M. López-Romero, R. Contreras-Caceres, D. Jaque, J. Rubio-Retama, *ACS Appl. Mater. Interfaces* **2020**, *12*, 12500.
[62] H. D. A. Santos, I. Zabala Gutiérrez, Y. Shen, J. Lifante, E. Ximendes, M. Laurenti, D. Méndez-González, S. Melle, O. G. Calderón, E. López Cabarcos, N. Fernández, I. Chaves-Coira, D. Lucena-Agell, L. Monge, M. D. Mackenzie, J. Marqués-Hueso, C. M. S. Jones, C. Jacinto, B. del Rosal, A. K. Kar, J. Rubio-Retama, D. Jaque, *Nat. Commun.* **2020**, *11*, 2933.
[63] S. Yakunin, B. M. Benin, Y. Shynkarenko, O. Nazarenko, M. I. Bodnarchuk, D. N. Dirin, C. Hofer, S. Cattaneo, M. V. Kovalenko, *Nat. Mater.* **2019**, *18*, 846.
[64] Z. Zhang, K. T. V. Grattan, A. W. Palmer, *Phys. Rev. B* **1993**, *48*, 7772.
[65] M. Back, E. Trave, J. Ueda, S. Tanabe, *Chem. Mater.* **2016**, *28*, 8347.
[66] J. Ueda, M. Back, M. G. Brik, Y. Zhuang, M. Grinberg, S. Tanabe, *Opt. Mater.* **2018**, *85*, 510.
[67] K. Elzbieciak, A. Bednarkiewicz, L. Marciniak, *Sens. Actuators, B* **2018**, *269*, 96.
[68] M. Back, J. Ueda, J. Xu, K. Asami, M. G. Brik, S. Tanabe, *Adv. Opt. Mater.* **2020**, *8*, 2000124.
[69] M. Back, J. Ueda, M. G. Brik, S. Tanabe, *ACS Appl. Mater. Interfaces* **2020**, *12*, 38325.
[70] V. B. Mykhaylyk, H. Kraus, V. Tsiumra, A. Luchechko, A. Wagner, A. Suchocki, *Sensors* **2020**, *20*, 5259.
[71] T. Lesniewski, S. Mahlik, M. Grinberg, R.-S. Liu, *Phys. Chem. Chem. Phys.* **2017**, *19*, 32505.
[72] T. Senden, R. J. A. van Dijk-Moes, A. Meijerink, *Light: Sci. Appl.* **2018**, *7*, 8.
[73] E. Glais, V. Đorđević, J. Papan, B. Viana, M. D. Dramićanin, *RSC Adv.* **2018**, *8*, 18341.
[74] M. Sekulić, Z. Ristić, B. Milićević, Ž. Antić, V. Đorđević, M. D. Dramićanin, *Opt. Commun.* **2019**, *452*, 342.
[75] M. D. Dramićanin, B. Milićević, V. Đorđević, Z. Ristić, J. Zhou, D. Milivojević, J. Papan, M. G. Brik, C.-G. Ma, A. M. Srivastava, M. Wu, *ChemistrySelect* **2019**, *4*, 7067.
[76] M. Grinberg, T. Lesniewski, *J. Lumin.* **2019**, *214*, 116574.
[77] M. Grinberg, *J. Lumin.* **1993**, *54*, 369.
[78] L. Marciniak, K. Trejgis, *J. Mater. Chem. C* **2018**, *6*, 7092.
[79] K. Kniec, K. Ledwa, L. Marciniak, *Nanomaterials* **2019**, *9*, 1375.
[80] P. M. Gschwend, D. Niedbalka, L. R. H. Gerken, I. K. Herrmann, S. E. Pratsinis, *Adv. Sci.* **2020**, *7*, 2000370.
[81] C. D. S. Brites, X. Xie, M. L. Debasu, X. Qin, R. Chen, W. Huang, J. Rocha, X. Liu, L. D. Carlos, *Nat. Nanotechnol.* **2016**, *11*, 851.

[82] R. Piñol, J. Zeler, C. D. S. Brites, Y. Gu, P. Téllez, A. N. Carneiro Neto, T. E. da Silva, R. Moreno-Loshuertos, P. Fernandez-Silva, A. I. Gallego, L. Martinez-Lostao, A. Martínez, L. D. Carlos, A. Millán, *Nano Lett.* **2020**, *20*, 6466.
[83] A. R. N. Bastos, C. D. S. Brites, P. A. Rojas-Gutierrez, C. DeWolf, R. A. S. Ferreira, J. A. Capobianco, L. D. Carlos, *Adv. Funct. Mater.* **2019**, *7*, 1905474.
[84] C. Abram, I. Wilson Panjikkaran, S. N. Ogugua, B. Fond, *Opt. Lett.* **2020**, *45*, 3893.
[85] R. G. Geitenbeek, A.-E. Nieuwelink, T. S. Jacobs, B. B. V. Salzmann, J. Goetze, A. Meijerink, B. M. Weckhuysen, *ACS Catal.* **2018**, *8*, 2397.
[86] T. Hartman, R. G. Geitenbeek, G. T. Whiting, B. M. Weckhuysen, *Nat. Catal.* **2019**, *2*, 986.
[87] J.-C. G. Bünzli, *J. Lumin.* **2016**, *170*, 866.
[88] J.-C. G. Bünzli, *Eur. J. Inorg. Chem.* **2017**, *2017*, 5058.
[89] J. Zhou, J. L. Leaño, Z. Liu, D. Jin, K.-L. Wong, R.-S. Liu, J.-C. G. Bünzli, *Small* **2018**, *14*, 1801882.
[90] E. Hemmer, N. Venkatachalam, H. Hyodo, A. Hattori, Y. Ebina, H. Kishimoto, K. Soga, *Nanoscale* **2013**, *5*, 11339.
[91] Y. Wu, M. J. Y. Ang, M. Sun, B. Huang, X. Liu, *J. Phys. D: Appl. Phys.* **2019**, *52*, 383002.
[92] W. M. Yen, W. C. Scott, A. L. Schawlow, *Phys. Rev.* **1964**, *136*, A271.
[93] S. Zhou, G. Jiang, X. Wei, C. Duan, Y. Chen, M. Yin, *J. Nanosci. Nanotechnol.* **2014**, *14*, 3739.
[94] M. S. Pudovkin, O. A. Morozov, V. V. Pavlov, S. L. Korableva, E. V. Lukinova, Y. N. Osin, V. G. Evtugyn, R. A. Safiullin, V. V. Semashko, *J. Nanomater.* **2017**, *2017*, 1.
[95] M. Runowski, P. Woźny, I. R. Martín, V. Lavín, S. Lis, *J. Lumin.* **2019**, *214*, 116571.
[96] F. Vetrone, R. Naccache, A. Zamarrón, A. La Juarranz de Fuente, F. Sanz-Rodríguez, L. Martinez Maestro, E. Martín Rodriguez, D. Jaque, J. García Solé, J. A. Capobianco, *ACS Nano* **2010**, *4*, 3254.
[97] P. Haro-González, I. R. Martín, L. L. Martín, S. F. León-Luis, C. Pérez-Rodríguez, V. Lavín, *Opt. Mater.* **2011**, *33*, 742.
[98] N.-N. Dong, M. Pedroni, F. Piccinelli, G. Conti, A. Sbarbati, J. E. Ramírez-Hernández, L. M. Maestro, M. C. La Iglesias-de Cruz, F. Sanz-Rodriguez, A. Juarranz, F. Chen, F. Vetrone, J. A. Capobianco, J. García Solé, M. Bettinelli, D. Jaque, A. Speghini, *ACS Nano* **2011**, *5*, 8665.
[99] D. Wawrzynczyk, A. Bednarkiewicz, M. Nyk, W. Strek, M. Samoc, *Nanoscale* **2012**, *4*, 6959.
[100] U. Rocha, C. Jacinto da Silva, W. Ferreira Silva, I. Guedes, A. Benayas, L. Martínez Maestro, M. Acosta Elias, E. Bovero, F. C. J. M. van Veggel, J. A. García Solé, D. Jaque, *ACS Nano* **2013**, *7*, 1188.
[101] X. Tian, X. Wei, Y. Chen, C. Duan, M. Yin, *Opt. Express* **2014**, *22*, 30333.
[102] G. Jiang, X. Wei, S. Zhou, Y. Chen, C. Duan, M. Yin, *J. Lumin.* **2014**, *152*, 156.
[103] S. Balabhadra, M. L. Debasu, C. D. S. Brites, L. A. O. Nunes, O. L. Malta, J. Rocha, M. Bettinelli, L. D. Carlos, *Nanoscale* **2015**, *7*, 17261.
[104] L. Marciniak, K. Prorok, A. Bednarkiewicz, A. Kowalczyk, D. Hreniak, W. Strek, *J. Lumin.* **2016**, *176*, 144.
[105] U. Rocha, C. Jacinto, K. U. Kumar, F. J. López, D. Bravo, J. G. Solé, D. Jaque, *J. Lumin.* **2016**, *175*, 149.
[106] E. C. Ximendes, W. Q. Santos, U. Rocha, U. K. Kagola, F. Sanz-Rodríguez, N. Fernández, A. d. S. Gouveia-Neto, D. Bravo, A. M. Domingo, B. del Rosal, C. D. S. Brites, L. D. Carlos, D. Jaque, C. Jacinto, *Nano Lett.* **2016**, *16*, 1695.
[107] L. Marciniak, A. Pilch, S. Arabasz, D. Jin, A. Bednarkiewicz, *Nanoscale* **2017**, *9*, 8288.
[108] L. Marciniak, A. Bednarkiewicz, W. Strek, *Sens. Actuators, B* **2017**, *238*, 381.
[109] A. Skripka, A. Benayas, R. Marin, P. Canton, E. Hemmer, F. Vetrone, *Nanoscale* **2017**, *9*, 3079.
[110] P. Cortelletti, A. Skripka, C. Facciotti, M. Pedroni, G. Caputo, N. Pinna, M. Quintanilla, A. Benayas, F. Vetrone, A. Speghini, *Nanoscale* **2018**, *10*, 2568.
[111] M. Xu, X. Zou, Q. Su, W. Yuan, C. Cao, Q. Wang, X. Zhu, W. Feng, F. Li, *Nat. Commun.* **2018**, *9*, 2698.
[112] G. Gao, D. Busko, S. Kauffmann-Weiss, A. Turshatov, I. A. Howard, B. S. Richards, *J. Mater. Chem. C* **2018**, *6*, 4163.
[113] L. Marciniak, A. Bednarkiewicz, K. Trejgis, K. Maciejewska, K. Elzbieciak, K. Ledwa, *Phys. Chem. Chem. Phys.* **2019**, *21*, 10532.
[114] G. Dantelle, M. Matulionyte, D. Testemale, A. Cantarano, A. Ibanez, F. Vetrone, *Phys. Chem. Chem. Phys.* **2019**, *21*, 11132.
[115] S. Zhou, C. Duan, M. Yin, S. Zhang, C. Wang, *J. Alloys Compd.* **2019**, *784*, 970.
[116] J. Ke, S. Lu, X. Shang, Y. Liu, H. Guo, W. You, X. Li, J. Xu, R. Li, Z. Chen, X. Chen, *Adv. Sci.* **2019**, *58*, 1901874.
[117] P. Huang, W. Zheng, D. Tu, X. Shang, M. Zhang, R. Li, J. Xu, Y. Liu, X. Chen, *Adv. Sci.* **2019**, *6*, 1802282.
[118] C. Mi, J. Zhou, F. Wang, G. Lin, D. Jin, *Chem. Mater.* **2019**, *31*, 9480.
[119] I. E. Kolesnikov, A. A. Kalinichev, M. A. Kurochkin, D. V. Mamonova, E. Y. Kolesnikov, E. Lähderanta, M. D. Mikhailov, *Nanotechnology* **2019**, *30*, 145501.
[120] A. Skripka, A. Morinvil, M. Matulionyte, T. Cheng, F. Vetrone, *Nanoscale* **2019**, *11*, 11322.
[121] M. Suta, Ž. Antić, V. Đorđević, S. Kuzman, M. D. Dramićanin, A. Meijerink, *Nanomaterials* **2020**, *10*, 543.
[122] R. Wu, J. Zhou, L. Lei, S. Zhang, Z. Xiao, J. Zhang, S. Xu, *Chem. Phys. Lett.* **2017**, *667*, 206.
[123] E. C. Ximendes, U. Rocha, T. O. Sales, N. Fernández, F. Sanz-Rodríguez, I. R. Martín, C. Jacinto, D. Jaque, *Adv. Funct. Mater.* **2017**, *27*, 1702249.
[124] E. C. Ximendes, A. F. Pereira, U. Rocha, W. F. Silva, D. Jaque, C. Jacinto, *Nanoscale* **2019**, *11*, 8864.
[125] M. A. R. C. Alencar, G. S. Maciel, C. B. de Araújo, A. Patra, *Appl. Phys. Lett.* **2004**, *84*, 4753.
[126] V. Lojpur, G. Nikolić, M. D. Dramićanin, *J. Appl. Phys.* **2014**, *115*, 203106.
[127] X. Xu, Z. Wang, P. Lei, Y. Yu, S. Yao, S. Song, X. Liu, Y. Su, L. Dong, J. Feng, H. Zhang, *ACS Appl. Mater. Interfaces* **2015**, *7*, 20813.
[128] T. Li, C. Guo, S. Zhou, C. Duan, M. Yin, *J. Am. Ceram. Soc.* **2015**, *98*, 2812.
[129] S. Balabhadra, M. L. Debasu, C. D. S. Brites, R. A. S. Ferreira, L. D. Carlos, *J. Phys. Chem. C* **2017**, *121*, 13962.
[130] L. Marciniak, K. Prorok, A. Bednarkiewicz, *J. Mater. Chem. C* **2017**, *5*, 7890.
[131] D. Ananias, F. A. Almeida Paz, L. D. Carlos, J. Rocha, *Chem. - Eur. J.* **2018**, *24*, 11926.
[132] M. Runowski, N. Stopikowska, D. Szeremeta, S. Goderski, M. Skwierczyńska, S. Lis, *ACS Appl. Mater. Interfaces* **2019**, *11*, 13389.
[133] H. Fu, C. Liu, P. Peng, F. Jiang, Y. Liu, M. Hong, *Adv. Sci.* **2020**, 2000731.
[134] R. G. Geitenbeek, P. T. Prins, W. Albrecht, A. van Blaaderen, B. M. Weckhuysen, A. Meijerink, *J. Phys. Chem. C* **2017**, *121*, 3503.
[135] R. G. Geitenbeek, B. B. V. Salzmann, A.-E. Nieuwelink, A. Meijerink, B. M. Weckhuysen, *Chem. Eng. Sci.* **2019**, *198*, 235.
[136] R. G. Geitenbeek, J. C. Vollenbroek, H. M. H. Weijgertze, C. B. M. Tregouet, A.-E. Nieuwelink, C. L. Kennedy, B. M. Weckhuysen, D. Lohse, A. van Blaaderen, A. van den Berg, M. Odijk, A. Meijerink, *Lab Chip* **2019**, *19*, 1236.
[137] I. K. Ravenhorst, R. G. Geitenbeek, M. J. Eerden, J. van Tijn Omme, H. H. Peréz Garza, F. Meirer, A. Meijerink, B. M. Weckhuysen, *ChemCatChem* **2019**, *11*, 5505.
[138] T. Hartman, R. G. Geitenbeek, C. S. Wondergem, W. van der Stam, B. M. Weckhuysen, *ACS Nano* **2020**, *14*, 3725.

[139] M. Runowski, P. Woźny, S. Lis, V. Lavín, I. R. Martín, *Adv. Mater. Technol.* **2020**, *5*, 1901091.
[140] F. J. Caixeta, A. R. N. Bastos, A. M. P. Botas, L. S. Rosa, V. S. Souza, F. H. Borges, A. N. C. Neto, A. Ferrier, P. Goldner, L. D. Carlos, R. R. Gonçalves, R. A. S. Ferreira, *J. Phys. Chem. C* **2020**, *120*, 19892.
[141] M. D. Dramićanin, Ž. Antić, S. Ćulubrk, S. P. Ahrenkiel, J. M. Nedeljković, *Nanotechnology* **2014**, *25*, 485501.
[142] B. So, J. Heo, *J. Am. Ceram. Soc.* **2018**, *101*, 3372.
[143] H. Peng, M. I. J. Stich, J. Yu, L.-N. Sun, L. H. Fischer, O. S. Wolfbeis, *Adv. Mater.* **2010**, *22*, 716.
[144] T. Kissel, J. Brübach, M. Euler, M. Frotscher, C. Litterscheid, B. Albert, A. Dreizler, *Mater. Chem. Phys.* **2013**, *140*, 435.
[145] V. Lojpur, S. Ćulubrk, M. D. Dramićanin, *J. Lumin.* **2016**, *169*, 534.
[146] J. Drabik, L. Marciniak, *J. Lumin.* **2019**, *208*, 213.
[147] A. L. Heyes, S. Seefeldt, J. P. Feist, *Opt. Laser Technol.* **2006**, *38*, 257.
[148] Z. Cao, S. Zhou, G. Jiang, Y. Chen, C. Duan, M. Yin, *Curr. Appl. Phys.* **2014**, *14*, 1067.
[149] S. Ćulubrk, V. Lojpur, S. P. Ahrenkiel, J. M. Nedeljković, M. D. Dramićanin, *J. Lumin.* **2016**, *170*, 395.
[150] L. M. Chepyga, A. Osvet, C. J. Brabec, M. Batentschuk, *J. Lumin.* **2017**, *188*, 582.
[151] L. M. Chepyga, E. Hertle, A. Ali, L. Zigan, A. Osvet, C. J. Brabec, M. Batentschuk, *J. Lumin.* **2018**, *197*, 23.
[152] E. Hertle, L. Chepyga, M. Batentschuk, S. Will, L. Zigan, *J. Lumin.* **2018**, *204*, 64.
[153] I. E. Kolesnikov, A. A. Kalinichev, M. A. Kurochkin, E. V. Golyeva, A. S. Terentyeva, E. Y. Kolesnikov, E. Lähderanta, *Sci. Rep.* **2019**, *9*, 2043.
[154] W. Xu, H. Zhao, Y. Li, L. Zheng, Z. Zhang, W. Cao, *Sens. Actuators, B* **2013**, *188*, 1096.
[155] S. Zhou, S. Jiang, X. Wei, Y. Chen, C. Duan, M. Yin, *J. Alloys Compd.* **2014**, *588*, 654.
[156] O. A. Savchuk, J. J. Carvajal, M. C. Pujol, E. W. Barrera, J. Massons, M. Aguilo, F. Diaz, *J. Phys. Chem. C* **2015**, *119*, 18546.
[157] O. A. Savchuk, J. J. Carvajal, P. Haro-Gonzalez, M. Aguiló, F. Díaz, *J. Alloys Compd.* **2018**, *746*, 710.
[158] M. D. Chambers, D. R. Clarke, *Annu. Rev. Mater. Res.* **2009**, *39*, 325.
[159] S. V. Yap, R. M. Ranson, W. M. Cranton, D. C. Koutsogeorgis, G. B. Hix, *J. Lumin.* **2009**, *129*, 416.
[160] C. D. S. Brites, P. P. Lima, N. J. O. Silva, A. Millán, V. S. Amaral, F. Palacio, L. D. Carlos, *Adv. Mater.* **2010**, *22*, 4499.
[161] J. Yu, L. Sun, H. Peng, M. I. J. Stich, *J. Mater. Chem.* **2010**, *20*, 6975.
[162] X. Liu, S. Akerboom, M. de Jong, I. Mutikainen, S. Tanase, A. Meijerink, E. Bouwman, *Inorg. Chem.* **2015**, *54*, 11323.
[163] E. Hemmer, M. Quintanilla, F. Légaré, F. Vetrone, *Chem. Mater.* **2015**, *27*, 235.
[164] I. N'Dala-Louika, D. Ananias, C. Latouche, R. Dessapt, L. D. Carlos, H. Serier-Brault, *J. Mater. Chem. C* **2017**, *5*, 10933.
[165] J. Rocha, C. D. S. Brites, L. D. Carlos, *Chem. - Eur. J.* **2016**, *22*, 14782.
[166] J. Liu, R. van Deun, A. M. Kaczmarek, *Nanomaterials* **2019**, *9*, 646.
[167] A. M. Kaczmarek, R. van Deun, P. van der Voort, *J. Mater. Chem. C* **2019**, *7*, 4222.
[168] a) A. M. Kaczmarek, Y. -Y. Liu, M. K. Kaczmarek, H. Liu, F. Artizzu, L. D. Carlos, P. van der Voort, *Angew. Chem.* **2020**, *132*, 1948; b) A. M. Kaczmarek, Y.-Y. Liu, M. K. Kaczmarek, H. Liu, F. Artizzu, L. D. Carlos, P. van der Voort, *Angew. Chem., Int. Ed.* **2020**, *59*, 1932.
[169] A. M. Kaczmarek, P. van der Voort, *Materials* **2020**, *13*, 566.
[170] A. M. Kaczmarek, M. Suta, H. Rijckaert, A. Abalymov, I. van Driessche, A. G. Skirtach, A. Meijerink, P. van der Voort, *Adv. Funct. Mater.* **2020**, *30*, 2003101.
[171] D. Errulat, R. Marin, D. A. Gálico, K. L. M. Harriman, A. Pialat, B. Gabidullin, F. Iikawa, O. D. D. Couto, J. O. Moilanen, E. Hemmer, F. A. Sigoli, M. Murugesu, *ACS Cent. Sci.* **2019**, *5*, 1187.
[172] a) R. Marin, G. Brunet, M. Murugesu, *Angew. Chem.* **2019**, https://doi.org/10.1002/ange.201910299; b) R. Marin, G. Brunet, M. Murugesu, *Angew. Chem Int. Ed.* **2019**, https://doi.org/10.1002/anie.201910299.
[173] G. E. Gomez, R. Marin, A. N. Carneiro Neto, A. M. P. Botas, J. Ovens, A. A. Kitos, M. C. Bernini, L. D. Carlos, G. J. A. A. Soler-Illia, M. Murugesu, *Chem. Mater.* **2020**, *32*, 7458.
[174] A. S. Souza, L. A. O. Nunes, I. G. N. Silva, F. A. M. Oliveira, L. L. da Luz, H. F. Brito, M. C. F. C. Felinto, R. A. S. Ferreira, S. A. Júnior, L. D. Carlos, O. L. Malta, *Nanoscale* **2016**, *8*, 5327.
[175] L. Marciniak, A. Bednarkiewicz, K. Elzbieciak, *J. Mater. Chem. C* **2018**, *6*, 7568.
[176] K. Trejgis, A. Bednarkiewicz, L. Marciniak, *Nanoscale* **2020**, *12*, 4667.
[177] K. Trejgis, R. Lisiecki, A. Bednarkiewicz, L. Marciniak, *J. Lumin.* **2020**, *224*, 117295.
[178] K. Trejgis, K. Maciejewska, A. Bednarkiewicz, L. Marciniak, *ACS Appl. Nano Mater.* **2020**, *3*, 4818.
[179] E. D. Martínez, C. D. S. Brites, L. D. Carlos, R. R. Urbano, C. Rettori, *Front. Chem.* **2019**, *7*, 83.
[180] E. D. Martínez, C. D. S. Brites, L. D. Carlos, A. F. García-Flores, R. R. Urbano, C. Rettori, *Adv. Funct. Mater.* **2019**, *29*, 1807758.
[181] Y. Shen, K. L. Bray, *Phys. Rev. B* **1998**, *58*, 11944.
[182] Z. Cao, X. Wei, L. Zhao, Y. Chen, M. Yin, *ACS Appl. Mater. Interfaces* **2016**, *8*, 34546.
[183] P. Pal, T. Penhouët, V. D'Anna, H. Hagemann, *J. Lumin.* **2013**, *142*, 66.
[184] T. Wylezich, A. D. Sontakke, V. Castaing, M. Suta, B. Viana, A. Meijerink, N. Kunkel, *Chem. Mater.* **2019**, *31*, 8957.
[185] J. Grimm, H. U. Güdel, *Chem. Phys. Lett.* **2005**, *404*, 40.
[186] J. Grimm, J. F. Suyver, E. Beurer, G. Carver, H. U. Güdel, *J. Phys. Chem. B* **2006**, *110*, 2093.
[187] M. P. Plokker, E. van der Kolk, *J. Lumin.* **2019**, *216*, 116694.
[188] M. P. Plokker, W. Hoogsteen, R. D. Abellon, K. W. Krämer, E. van der Kolk, *J. Lumin.* **2020**, *225*, 117327.
[189] T. Tsuboi, D. S. McClure, W. C. Wong, *Phys. Rev. B* **1993**, *48*, 62.
[190] Z. Pan, C.-K. Duan, P. A. Tanner, *Phys. Rev. B* **2008**, *77*, 85114.
[191] P. Schouwink, M. B. Ley, A. Tissot, H. Hagemann, T. R. Jensen, L. Smrčok, R. Černý, *Nat. Commun.* **2014**, *5*, 5706.
[192] M. Suta, C. Wickleder, *Adv. Funct. Mater.* **2017**, *27*, 1602783.
[193] M. Suta, T. Senden, J. Olchowka, M. Adlung, A. Meijerink, C. Wickleder, *Phys. Chem. Chem. Phys.* **2017**, *19*, 7188.
[194] M. Suta, C. Wickleder, *J. Lumin.* **2019**, *210*, 210.
[195] C. D. S. Brites, K. Fiaczyk, J. F. C. B. Ramalho, M. Sójka, L. D. Carlos, E. Zych, *Adv. Opt. Mater.* **2018**, *6*, 1701318.
[196] M. Sójka, J. F. C. B. Ramalho, C. D. S. Brites, K. Fiaczyk, L. D. Carlos, E. Zych, *Adv. Opt. Mater.* **2019**, *7*, 1901102.
[197] M. Sójka, C. D. S. Brites, L. A. D. Carlos, E. Zych, *J. Mater. Chem. C* **2020**, *8*, 10086.
[198] R. G. Geitenbeek, H. W. de Wijn, A. Meijerink, *Phys. Rev. Appl.* **2018**, *10*, 64006.
[199] L. Labrador-Páez, M. Pedroni, A. Speghini, J. García-Solé, P. Haro-González, D. Jaque, *Nanoscale* **2018**, *10*, 22319.
[200] Y. Shen, J. Lifante, N. Fernández, D. Jaque, E. Ximendes, *ACS Nano* **2020**, *14*, 4122.
[201] M. Dramićanin, *Luminescence Thermometry: Methods, Materials, and Applications*, Woodhead Publishing (Elsevier), Duxford **2018**.
[202] M. D. Dramićanin, *J. Appl. Phys.* **2020**, *128*, 40902.
[203] A. Bednarkiewicz, L. Marciniak, L. A. D. Carlos, D. Jaque Garcia, *Nanoscale* **2020**, *12*, 14405.
[204] A. Ćirić, S. Stojadinović, M. D. Dramićanin, *J. Lumin.* **2019**, *216*, 116749.
[205] A. M. Kaczmarek, R. van Deun, M. K. Kaczmarek, *Sens. Actuators, B* **2018**, *273*, 696.

[206] M. Bartelmann, B. Feuerbacher, T. Krüger, D. Lüst, A. Rebhan, A. Wipf, *Theoretische Physik 4. Thermodynamik und Statistische Physik*, Springer Spektrum, Berlin, **2018**.
[207] E. Ejder, *J. Opt. Soc. Am.* **1969**, *59*, 223.
[208] M. de Jong, L. Seijo, A. Meijerink, F. T. Rabouw, *Phys. Chem. Chem. Phys.* **2015**, *17*, 16959.
[209] D. Avram, C. Tiseanu, *Methods Appl. Fluoresc.* **2018**, *6*, 25004.
[210] B. R. Judd, *Phys. Rev.* **1962**, *127*, 750.
[211] G. S. Ofelt, *J. Chem. Phys.* **1962**, *37*, 511.
[212] D. Toptygin, *J. Fluoresc.* **2003**, *13*, 201.
[213] C.-K. Duan, M. F. Reid, *Curr. Appl. Phys.* **2006**, *6*, 348.
[214] C. K. Duan, M. F. Reid, *Spectrosc. Lett.* **2007**, *40*, 237.
[215] T. Senden, F. T. Rabouw, A. Meijerink, *ACS Nano* **2015**, *9*, 1801.
[216] C. Görller-Walrand, K. Binnemans in *Handbook on the Physics and Chemistry of Rare Earths* (Eds: K. A. Gschneidner Jr, L. Eyring), Elsevier, Amsterdam **1998**, pp. 101–264.
[217] W. T. Carnall, G. L. Goodman, K. Rajnak, R. S. Rana, *J. Chem. Phys.* **1989**, *90*, 3443.
[218] C. M. Dodson, R. Zia, *Phys. Rev. B* **2012**, *86*, 61.
[219] M. P. Hehlen, M. G. Brik, K. W. Krämer, *J. Lumin.* **2013**, *136*, 221.
[220] A. Ćirić, S. Stojadinović, M. Sekulić, M. D. Dramićanin, *J. Lumin.* **2019**, *205*, 351.
[221] S. F. León-Luis, U. R. Rodríguez-Mendoza, P. Haro-González, I. R. Martín, V. Lavín, *Sens. Actuators, B.* **2012**, *174*, 176.
[222] Y. Yang, C. Mi, F. Jiao, X. Su, X. Li, L. Liu, J. Zhang, F. Yu, Y. Liu, Y. Mai, *J. Am. Ceram. Soc.* **2014**, *97*, 1769.
[223] N. Rakov, G. S. Maciel, *J. Appl. Phys.* **2017**, *121*, 113103.
[224] O. L. Malta, *Chem. Phys. Lett.* **1982**, *87*, 27.
[225] P. S. Peijzel, A. Meijerink, R. T. Wegh, M. F. Reid, G. W. Burdick, *J. Solid State Chem.* **2005**, *178*, 448.
[226] C.-K. Duan, P. A. Tanner, *J. Phys. Chem. A* **2010**, *114*, 6055.
[227] M. F. Reid in *Handbook on the Physics and Chemistry of Rare Earths* (Eds: J. -C. G. Bünzli, V. K. Pecharsky), Elsevier, Amsterdam **2016**, pp. 47–64.
[228] J. D. L. Dutra, T. D. Bispo, R. O. Freire, *J. Comput. Chem.* **2014**, *35*, 772.
[229] J. D. L. Dutra, N. B. D. Lima, R. O. Freire, A. M. Simas, *Sci. Rep.* **2015**, *5*, 13695.
[230] F. Neese, *WIREs Comput. Mol. Sci.* **2012**, *2*, 73.
[231] F. Neese, F. Wennmohs, U. Becker, C. Riplinger, *J. Chem. Phys.* **2020**, *152*, 224108.
[232] J. J. Joos, P. F. Smet, L. Seijo, Z. Barandiarán, *Inorg. Chem. Front.* **2020**, *7*, 871.
[233] J. J. Joos, D. van der Heggen, L. I. D. J. Martin, L. Amidani, P. F. Smet, Z. Barandiarán, L. Seijo, *Nat. Commun.* **2020**, *11*, 3647.
[234] C. K. Jørgensen, R. Pappalardo, H.-H. Schmidtke, *J. Chem. Phys.* **1963**, *39*, 1422.
[235] C. E. Schäffer, C. K. Jørgensen, *Mol. Phys.* **1965**, *9*, 401.
[236] W. Urland, *Chem. Phys.* **1976**, *14*, 393.
[237] A. Bronova, T. Bredow, R. Glaum, W. Urland, *Inorg. Chem.* **2016**, *55*, 6853.
[238] A. Bronova, T. Droß, R. Glaum, H. Lueken, M. Speldrich, W. Urland, *Inorg. Chem.* **2016**, *55*, 6848.
[239] A. Bronova, N. Kannengießer, R. Glaum, *Inorg. Chem.* **2017**, *56*, 9235.
[240] A. Bronova, T. Bredow, R. Glaum, M. J. Riley, W. Urland, *J. Comput. Chem.* **2018**, *39*, 176.
[241] R. Glaum, W. Grunwald, N. Kannengießer, A. Bronova, *Z. Anorg. Allg. Chem.* **2020**, *646*, 184.
[242] B. Cao, J. Wu, X. Wang, Y. He, Z. Feng, B. Dong, *Sensors* **2015**, *15*, 30981.
[243] L. Li, F. Qin, Y. Zhou, Y. Zheng, J. Miao, Z. Zhang, *Sens. Actuators, A* **2020**, *304*, 111864.
[244] A. Ćirić, J. Aleksić, T. Barudžija, Ž. Antić, V. Đorđević, M. Medić, J. Periša, I. Zeković, M. Mitrić, M. D. Dramićanin, *Nanomaterials* **2020**, *10*, 627.
[245] A. Benayas, B. del Rosal, A. Pérez-Delgado, K. Santacruz-Gómez, D. Jaque, G. A. Hirata, F. Vetrone, *Adv. Opt. Mater.* **2015**, *3*, 687.
[246] B. Fond, C. Abram, M. Pougin, F. Beyrau, *Opt. Mater.* **2019**, *89*, 615.
[247] J. A. Capobianco, P. Kabro, F. S. Ermeneux, R. Moncorgé, M. Bettinelli, E. Cavalli, *Chem. Phys.* **1997**, *214*, 329.
[248] P. Villanueva-Delgado, D. Biner, K. W. Krämer, *J. Lumin.* **2017**, *189*, 84.
[249] C. W. Struck, W. H. Fonger, *J. Lumin.* **1975**, *10*, 1.
[250] C. W. Struck, W. H. Fonger, *Understanding Luminescence Spectra and Efficiency Using W_p and Related Functions*, Springer, Berlin **1991**.
[251] K. Huang, A. Rhys, *Proc. R. Soc. London, Ser. A* **1950**, *204*, 406.
[252] L. A. Riseberg, H. W. Moos, *Phys. Rev. Lett.* **1967**, *19*, 1423.
[253] P. Kisliuk, C. A. Moore, *Phys. Rev.* **1967**, *160*, 307.
[254] L. A. Riseberg, H. W. Moos, *Phys. Rev.* **1968**, *174*, 429.
[255] M. J. Weber, *Phys. Rev.* **1968**, *171*, 283.
[256] H. W. Moos, *J. Lumin.* **1970**, *1*, 106.
[257] C. B. Layne, W. H. Lowdermilk, M. J. Weber, *Phys. Rev. B* **1977**, *16*, 10.
[258] A. Ellens, H. Andres, A. Meijerink, G. Blasse, *Phys. Rev. B* **1997**, *55*, 173.
[259] A. Ellens, H. Andres, M. L. H. ter Heerdt, R. T. Wegh, A. Meijerink, G. Blasse, *Phys. Rev. B* **1997**, *55*, 180.
[260] V. L. Ermolaev, E. B. Sveshnikova, *J. Lumin.* **1979**, *20*, 387.
[261] E. B. Sveshnikova, V. L. Ermolaev, *Opt. Spectrosc.* **2011**, *111*, 34.
[262] a) R. Arppe, I. Hyppänen, N. Perälä, R. Peltomaa, M. Kaiser, C. Würth, S. Christ, U. Resch-Genger, M. Schäferling, T. Soukka, *Nanoscale* **2015**, *7*, 11746; b) M. Kraft, C. Würth, V. Muhr, T. Hirsch, U. Resch-Genger, *Nano Res.* **2018**, *11*, 6360.
[263] F. T. Rabouw, P. T. Prins, P. Villanueva-Delgado, M. Castelijns, R. G. Geitenbeek, A. Meijerink, *ACS Nano* **2018**, *12*, 4812.
[264] M. Bartelmann, B. Feuerbacher, T. Krüger, D. Lüst, A. Rebhan, A. Wipf, *Theoretische Physik 2. Elektrodynamik*, Springer Spektrum, Berlin **2018**.
[265] B. Barnett, R. Englman, *J. Lumin.* **1970**, *3*, 55.
[266] R. Englman, B. Barnett, *J. Lumin.* **1970**, *3*, 37.
[267] E. S. Medvedev, *Chem. Phys. Lett.* **1985**, *120*, 173.
[268] R. Englman, J. Jortner, *Mol. Phys.* **1970**, *18*, 145.
[269] E. S. Medvedev, *Spectrosc. Lett.* **1985**, *18*, 447.
[270] E. S. Medvedev, *J. Chem. Phys.* **2012**, *137*, 174307.
[271] K. K. Lehmann, A. M. Smith, *J. Chem. Phys.* **1990**, *93*, 6140.
[272] A. Aharoni, D. Oron, U. Banin, E. Rabani, J. Jortner, *Phys. Rev. Lett.* **2008**, *100*, 57404.
[273] J. M. F. van Dijk, M. F. H. Schuurmans, *J. Chem. Phys.* **1983**, *78*, 5317.
[274] W. E. Hagston, J. E. Lowther, *Physica* **1973**, *70*, 40.
[275] K. K. Pukhov, V. P. Sakun, *Phys. Status Solidi B* **1979**, *95*, 391.
[276] Y. V. Orlovskii, R. J. Reeves, R. C. Powell, T. T. Basiev, K. K. Pukhov, *Phys. Rev. B* **1994**, *49*, 3821.
[277] K. K. Pukhov, T. T. Basiev, Y. V. Orlovskii, M. Glasbeek, *J. Lumin.* **1998**, *76-77*, 586.
[278] K. K. Pukhov, *Phys. Solid State* **2008**, *50*, 1597.
[279] F. S. Ermeneux, C. Goutaudier, R. Moncorgé, Y. Sun, R. L. Cone, E. Zannoni, E. Cavalli, M. Bettinelli, *Phys. Rev. B* **2000**, *61*, 3915.
[280] D. L. Dexter, *J. Chem. Phys.* **1953**, *21*, 836.
[281] M. Chua, P. A. Tanner, M. F. Reid, *Solid State Commun.* **1994**, *90*, 581.
[282] W. Strek, *J. Chem. Phys.* **1982**, *76*, 5856.
[283] J. F. Suyver, J. Grimm, M. K. van Veen, D. Biner, K. W. Krämer, H. U. Güdel, *J. Lumin.* **2006**, *117*, 1.

Markus Suta (30) studied Chemistry (M.Sc.) at the University of Siegen, Germany, and obtained his doctoral degree in the group of Prof. Claudia Wickleder in 2017 on the luminescence of divalent lanthanides and excitons in inorganic halides. He followed up with a second degree in Physics (M.Sc.) with specialization in Theoretical Physics in the group of Prof. Thomas Mannel in Siegen. Since November 2018, he has been a postdoctoral researcher in the group of Prof. Andries Meijerink at the University of Utrecht working on the theoretical modelling and experimental investigation of lanthanide-based nanothermometers within the EU-funded H2020 FET-Open project NanoTBTech.

Andries Meijerink (56) received his Ph.D. degree in Chemistry in the group of Prof. George Blasse at Utrecht University, the Netherlands in 1990. After a postdoctoral period in the group of Prof. John Wright at the University of Wisconsin, Madison, he was appointed at the chair of Solid State Chemistry in the Debye Institute of Utrecht University. His research group focusses on the optical spectroscopy of lanthanide ions in solids and of semiconductor quantum dots. In the field of lanthanide ions his recent work involved fundamental research and applications in solar cells, LEDs, scintillators, photonics and luminescent thermometers.